SAPIENZA
UNIVERSITÀ DI ROMA

Tuning the magnetic properties of self-assembled metal-phthalocyanine on intercalated graphene

Candidate: Giulia Avvisati, 1401628
Thesis Advisor: Prof. Maria Grazia Betti

PhD School in Astronomical, Chemical, Physical and Mathematical Sciences
"Vito Volterra"
PhD in Physics – XXXI cycle
January 2019

A Thesis presented for the degree of
Doctor of Philosophy

Tuning the magnetic properties of self-assembled metal-phthalocyanine on intercalated graphene

Giulia Avvisati

Submitted for the degree of Doctor of Philosophy
January 2019

Abstract

We report on advanced organic spin-interface architectures constituted by metal (manganese, iron, copper) phthalocyanine molecules magnetically coupled with ferromagnetic layer(s), mediated by graphene. The rippled moiré superstructure of graphene/Ir(111), intercalated with a single magnetic layer, drives the assembly of evenly-spaced molecular bits, providing preferential adsorption regions for the phthalocyanine molecules. Our X-ray absorption and photoemission results show that the graphene layer shields the electronic/magnetic state of the molecules, screening the charge transfer/orbital intermixing with the metallic surface. The magnetic response of the molecular spin interfaces and its robustness against thermal fluctuations were investigated by X-ray magnetic circular dichroism. Mn-, Fe- and Cu-phthalocyanines assemble on graphene/Co with identical structural configurations, but MnPc and FePc are strongly antiferromagnetically coupled with Co up to room temperature, while CuPc couples ferromagnetically with weaker thermal stability. The robust antiferromagnetic alignment is stabilized by a superexchange interaction, driven by the out-of-plane molecular orbitals responsible of the magnetic ground state and electronically decoupled from the underlying metal via the graphene layer, as confirmed by ab initio theoretical predictions. The strength and stability of the magnetic coupling is further optimized by the open $3d$ shell of the central Mn ion. These archetypal spin interfaces can be prototypes to demonstrate how antiferromagnetic/ ferromagnetic coupling can be optimized by selecting the molecular orbital symmetry, paradigmatic examples to exploit in surface-supported molecular spin electronics.

Contents

Chapter 1

Molecular spin interfaces: a brief introduction

The ultimate goal of nanomagnetism is to establish a route to achieve a well ordered spin network, with the smallest unit, exhibiting a high magnetic anisotropy and tunable magnetic state, robust against thermal fluctuations. This intriguing research field is motivated by the rising of spintronics, *i.e.*, electronics with spins, born with the discovery of the giant magnetoresistance that led to the award of the 2007 Nobel prize to A. Fert and P. Grünberg [1]. From a technological point of view, adding the spin degree of freedom will add substantially more capability and performance to electronic devices. Non-volatile information storage, increased processing speed, decreased power consumption and increased integration densities complete the picture [2], inspiring much experimental effort towards magnetic nanostructures. Such systems, besides meeting the demands for devices miniaturization, provide a new platform for fundamental science. Indeed, when dimension/coordination is reduced, exotic (absent/irrelevant in bulk materials) magnetic phenomena arise [3, 4], such as increase of the orbital magnetic moment [5], Kondo effect [6], enhanced magnetic anisotropy [5] and many more.

The smallest spin unit is undoubtedly represented by individual atoms, but it is difficult to attain a well-ordered arrangement of single atoms on surfaces [7] as they tend to form clusters, not to mention the effects of thermal-induced mobility [8]. Furthermore, the magnetic state of single-atom magnets strongly depends on the surrounding environment [9] and is very fragile against thermal fluctuations. In particular, single Ho atoms deposited on metallic substrates (e.g. Pt(111)) exhibit perfect paramagnetic behaviour down to 2.5 K [10], while adsorption on the insulating MgO support guarantees the protection of the

magnetic state against scattering with electrons and phonons, ensuring a stable magnetic state up to 35 K, the best configuration achieved and recently reported in Refs. [11,12]. It is worth to highlight that the Ho adatoms on the MgO/Ag(100) substrate start to migrate on the surface above 50 K, giving an upper limit to the critical temperature of the system.

A stable and reproducible long-range ordering of single-ion magnets can be achieved by self-assembly of metal-organic molecules, thanks to their capability to form intermolecular weak directional bonds [13], as well as to be sensitive to polarization effects induced by adsorption on metallic surfaces [14]. The final pattern is determined by a subtle interplay between molecule-molecule and molecule-substrate interaction [15] and, generally, the spacing between spin units is larger for metal-organic building blocks as compared to inorganic materials, hence preventing undesirable electronic/magnetic coupling among adjacent units. The choice of molecular spin units resides in the combined role of delocalized organic π orbitals, driving the formation of well ordered surface-supported architectures with the aforementioned qualities, while the incorporated metallic cores arrange in a regular network with intriguing magnetic/electronic properties [16]. Furthermore, the light weight (low Z) of metal-organic molecules ensures low spin-orbit coupling and hyperfine interactions, and hence long spin lifetimes and diffusion lengths [17]. From a technological point of view, the possibility to combine efficient spin transport with the potential of organic molecular semiconductors could enable molecular spintronics applications, with the ultimate bit being a single molecule [1].

However, molecular spin units often exhibit paramagnetic behaviour at temperatures above a few K [18, 19]. To the best of our knowledge, the most stable configuration achieved so far for surface-supported single-ion molecular magnets, described in Ref. [20], is represented by double-decker phthalocyanines hosting a rare earth atom, specifically terbium, adsorbed on the insulating MgO surface. $TbPc_2$ on MgO exhibit an exceptional zero-field magnetic remanence and an unprecedented blocking temperature of 8 K, still far from the goal of room-temperature activity. The desired thermal stability of the molecular magnetic state must then be induced by coupling with a ferromagnetic substrate. Recently, much attention has been paid to the interface between adsorbed molecules and the supporting surface. Several mechanisms occurring at the interface can influence the molecule-substrate interaction [14, 21], such as charge transfer, formation of interface dipoles, hybridization-induced reduction of the molecular symmetry as well as the appearance of the interface-localized electronic states. Direct adsorption of molecules

on the surface of reactive magnetic metals is usually characterised by chemisorption with covalent bonding between the transition metal surface and the adsorbed metal-organic molecule. This results in the strong hybridization between the d bands of the metal and the π molecular orbitals, giving rise to bonding and antibonding hybrid states [22]. Even if the formation of spin-polarized hybrid interface states has interesting spin-filtering properties [22–25], bond formation has the disadvantage to also maximise the charge transfer from the substrate to the molecular orbitals, reducing or even quenching the magnetic moment of the molecular building block [26], as reported in the left part of Fig. 1.1. Explicitly, E. Annese and her collaborators recently investigated the interface magnetic coupling between adsorbed Iron-Phthalocyanine (FePc) molecules and the underlying Co(0001) surface [27]. On the one hand, they successfully obtained a remarkable exchange coupling, much stronger than thermal fluctuations up to Room Temperature (RT). On the other hand, they estimated a reduction by a factor two(ten) of the spin(orbital) magnetic moment, with respect to the molecular crystal, because of re-hybridization and alteration of the spin-polarized molecular orbitals of the FePc molecules in contact with Co.

To achieve the optimized configuration, the magnetic state of the molecular spin units has to be protected by screening the electronic interaction with the metallic substrate, but stabilized against thermal fluctuations via magnetic coupling with the underlying ferromagnet.

In this thesis, we propose a strategic route to design molecular spin architectures that can guarantee *(i)* a long-range ordering of well-separated spin units *(ii)* with preserved electronic/magnetic configuration upon adsorption and *(iii)* exhibiting a magnetic response robust against thermal fluctuations, up to RT. Such molecular spin interfaces are obtained by depositing our molecular units on Graphene (Gr) intercalated with Co layer(s), combining the decoupling effect of a Gr buffer layer with the magnetic stability induced by coupling with a ferromagnetic substrate.

We choose archetypal molecular spin units: Transition Metal Phthalocyanine (TMPc) molecules. TMPcs are small (1.5 nm wide), square-shaped and planar metal-organic molecules with applications in optoelectronic [28] and in the pigment industry [29], as well as in organic spintronics [30]. They are ideal for *in-situ* investigation in an ultra-high-vacuum environment, because of their excellent stability that allows for *in-vacuo* thermal sublimation. TMPcs share an identical Pc cage made up by four benzene and four pyrrole rings, embedding a central metal core. The common configuration of the

organic ligands ensures ordered self-assembly, with reproducible patterns only slightly depending on the TM atom [31], while their planar geometry allows the interaction between the extended surface states of the substrate and the central metal ion. Furthermore, the possibility to change the transition metal centres allows exploring different configurations of the molecular spin units, e.g. magnetic moments, easy magnetization direction, magnetic anisotropy energy... [32]. TMPc molecules offer an excellent playground, allowing to study coupling with magnetic materials [33], intramolecular spin transport [34], Kondo effects [35], and much more intriguing physics.

Metal-organic spin networks can be stabilized by suitable templates, able to preserve their electronic/magnetic state and favouring the desired magnetic response. Gr can be elected as a promising candidate thanks to its excellent properties for spin electronic applications, with high in-plane charge carrier mobility [36] as well as spin filtering [37] and transport [38]. Furthermore, it only weakly couples with adsorbed/underlying materials via van der Waals-like interactions [39, 40], acting as an ideal spacer between metal-organic adsorbates and underlying reactive magnetic surfaces. Magnetic exchange coupling with the Ni(111) surface through Gr has been reported for isolated Co atoms/clusters [41], cobaltocene [42], Co-porphyrin [43] and -octaethylporphyrin [44], as well as for Fe-porphyrin [45] and -phthalocyanine [46]. Notably, C. F. Hermanns and co-workers recently reported a solid magnetic coupling between Co-porphyrins (CoOEP) and (111)-oriented Ni films, through a Gr spacer [44]. The authors provide evidences, also summarized in the right panel of Fig. 1.1, for electronic decoupling of the adsorbed metal-organic molecules thanks to the Gr covering of the Ni surface. The electronic structure and, accordingly, the molecular magnetic moment fully resemble that of a thick CoOEP film, while an antiferromagnetic alignment is reported, activated by the presence of the paramagnetic Gr layer. However, RT remanence is still elusive in such Gr-based atomic/molecular systems. A special effort is needed to obtain molecular spin networks with magnetic activity robust against thermal fluctuations, as a first crucial step towards the integration of molecular magnetic bits in operational spintronic devices.

In this scientific context, briefly summarized in Fig. 1.1, we would take the next step and propose novel molecular spin architectures with preserved molecular structural, electronic and magnetic configurations but with magnetic activity robust against thermal fluctuations. The aims of this thesis are:

1. to identify strategic support for molecular spin interfaces with long-range ordering;

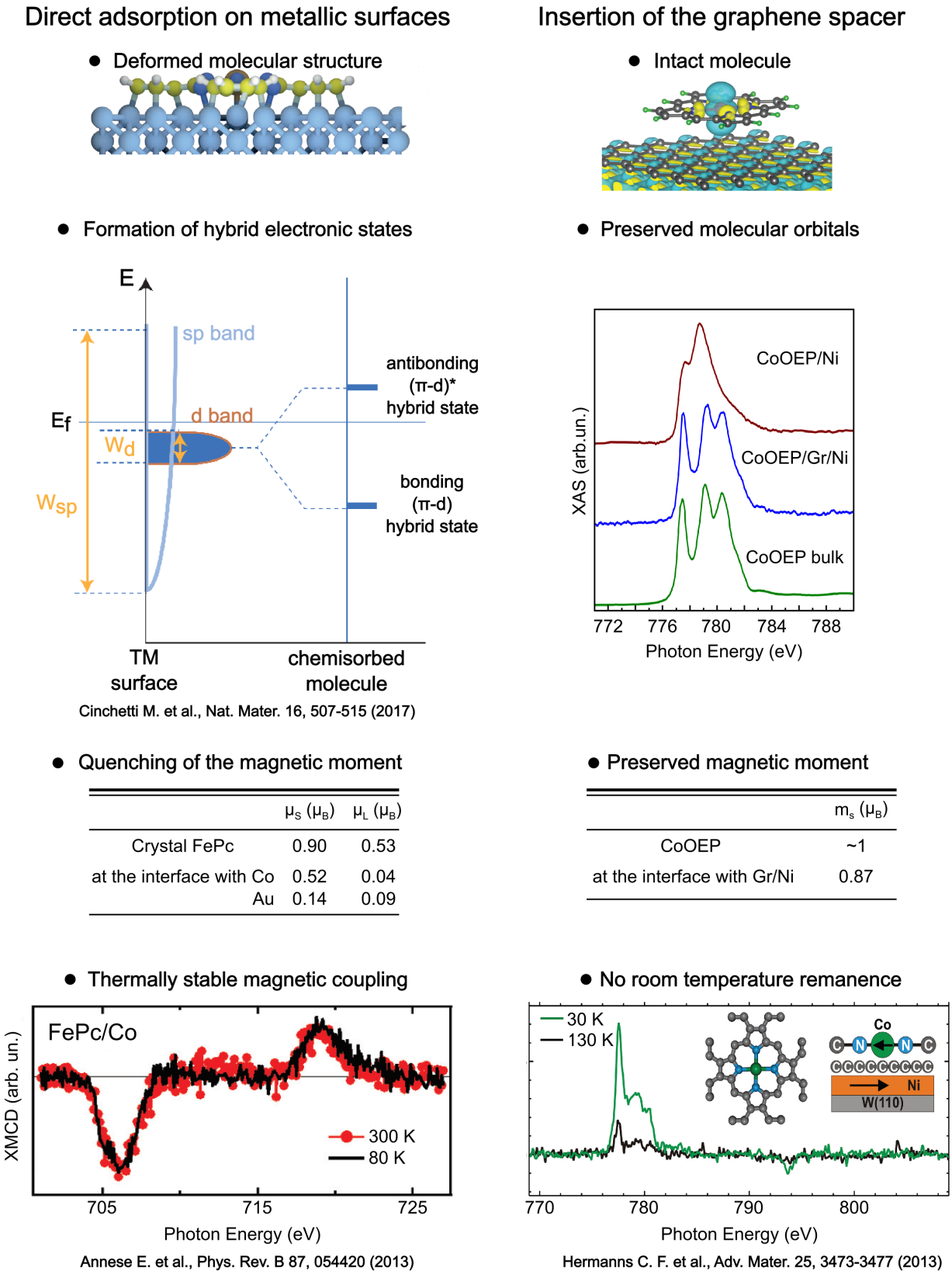

	μ_S (μ_B)	μ_L (μ_B)
Crystal FePc	0.90	0.53
at the interface with Co	0.52	0.04
Au	0.14	0.09

	m_s (μ_B)
CoOEP	~1
at the interface with Gr/Ni	0.87

Figure 1.1: Comparison between the structural [22, 44], electronic [22, 44] and magnetic [27, 44] configurations of molecular spin interfaces with (right) and without (left) the insertion of a graphene spacer.

2. to control the charge transfer/orbital intermixing at the interface between the molecular units and the Gr-based support, to prevent filling of the spin-polarized molecular orbitals and, accordingly, reduction/quenching of the molecular spin moment;

3. to ensure thermal stability of the magnetic state and to optimize the magnetic coupling channels and determine the fundamental parameters involved in driving the sign and the strength of the coupling.

The very low concentration of metal centers on the TMPc-covered Gr surface demands for surface sensitive experimental techniques, with high photon flux to minimize measurements time and avoid sample contamination. Therefore, we exploited X-ray Photoemission Spectroscopy (XPS) and Near Edge X-ray Absorption Fine Structure (NEXAFS) to address the effect of adsorption on Gr on the core levels and on the frontier empty molecular orbitals, respectively, disentangling the effects on the organic ligands from the interaction channels involving the metal centers. The magnetic activity of the surface was investigated by means of X-ray Magnetic Circular Dichroism (XMCD) measurements, allowing for a quantitative determination of the element specific spin and orbital contribution to the magnetic moment, separating the role of the magnetic intercalant from that of the molecular centers.

The ultimate understanding of the fundamental forces driving the self-assembly (Chap. 3) and the magnetic coupling (Chap. 4) at the molecule-graphene/ ferromagnet interface (Chap.2), is indeed crucial to design a molecular magnetic system with the desired functionalities.

Chapter 2

The graphene/ferromagnet substrate: a strategic support

The magnetic substrate is the first ingredient to optimize the magnetic coupling in molecular spin architectures. Indeed, the choice of the substrate not only influences the sign and the strength of the magnetic coupling, but can also drive the self-assembly of the molecular units and impact on the magnetic state of the adsorbate itself. The ideal substrate is capable to *(i)* electronically decouple the adsorbed molecular units, to preserve their magnetic state upon adsorption, while *(ii)* allowing for magnetic coupling, essential to stabilize the magnetic state of the system against thermal fluctuations. Finally, *(iii)* a fine tuning of the relevant parameters for spintronics applications would be desirable. In particular, the magnetic energy must exceed the thermal energy to avoid spontaneous spin flip but, at the same time, must remain below the practical writing energies. Furthermore, a Perpendicular Magnetic Anisotropy (PMA) is preferable to facilitate the writing process as well as inhibit magnetic coupling between adjacent bits. In this chapter, the structural, electronic and magnetic configurations of the ferromagnetic supports for our molecular spin networks are presented. First, we will describe how the moiré superstructure of pristine graphene/Ir is altered upon increasing Co intercalation, to provide a complete picture of the template for our molecular architectures. Then a thorough investigation of the magnetic properties for this peculiar graphene-based ferromagnetic support will be presented and, finally, a route to further optimize its magnetic activity will be proposed.

2.1 The versatile Co-intercalated graphene/Ir(111) substrate

The ideal magnetic support for molecular spin architectures is able to prevent molecular symmetry reduction [47] and the decrease/quenching of the molecule spin moment [26,27, 48] upon adsorption. Recently, interposing a Gr buffer layer has been proved to effectively decouple the adsorbed TMPc molecules (TM= Fe [39], Co, Cu [49]) from the Gr growth substrate. However, TMPcs preserve their paramagnetic state when not strongly coupled with a magnetic substrate [48].

We propose to combine the electronic decoupling role of Gr with the possibility to magnetically couple our TMPc molecular building blocks with a magnetic support by intercalating a ferromagnetic metal beneath the Gr sheet. Intercalation between Gr and its metallic growth substrate is indeed an established route to functionalise Gr from below, as well as to ensure the protection of the intercalant [50–52], without damaging the Gr overlayer. Intercalation is a widely used procedure to decouple the Gr adlayer from its metallic growth substrate [53, 54], to alter its band structure via doping [55, 56] and to manipulate the interaction with the adsorbate from behind [57]. Furthermore, by tuning the Gr/substrate hybridization it is possible to induce/enhance in-plane [58, 59] or out-of-plane [60] magnetic anisotropy of molecular/atomic adsorbates.

Metal intercalation beneath a Gr sheet ensures the growth of a smooth single metal layer, without grain formation, and is an excellent playground to investigate defectless ultrathin films of ferromagnetic metals/alloys with altered properties with respect to their bulk counterpart, and under tensile stress induced by epitaxial growth. In this chapter, this peculiar magnetic support will be described, together with the tuning of its structural arrangement (highly corrugated or flat) and magnetic state (easy-axis or easy-plane anisotropy).

2.1.1 Structural and electronic environment: a template for molecular assembly

Gr can be easily grown on the Ir(111) surface by thermal decomposition of a hydrocarbon precursor, resulting in a high-quality and almost free standing single Gr layer. Because of non-integer mismatch between the lattice parameters of Gr (2.46 Å) and Ir(111) (2.72 Å) a 9.32 × 9.32 moiré superstructure is formed [61, 62], with an average C-Ir distance of about 3.4 Å and a gentle corrugation of 0.3 Å [63]. The C1s core level of Gr (grey curve in Fig. 2.1), weakly interacting with the Ir(111) surface, consists of one sharp peak

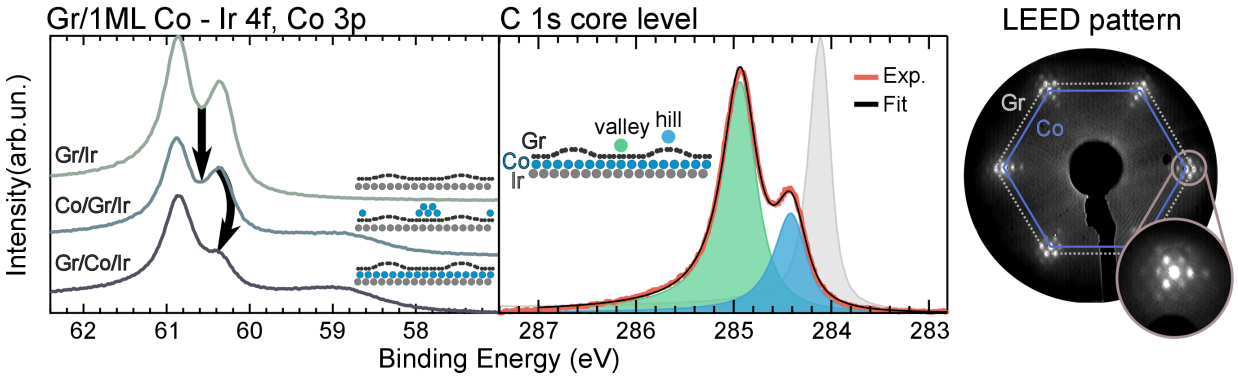

Figure 2.1: Left: Ir4f core level evolution going from pristine Gr/Ir through Co-covered Gr/Ir to Co-intercalated Gr/Ir(111). Center: C1s core level for bare Gr/Ir(111) (grey curve) and upon intercalation of Co. Right: LEED pattern of Gr/Co/Ir(111), with preserved periodicity and symmetry of the moiré satellite spots characteristics of pristine Gr/Ir(111). The Co coverage is 1.0±0.1 ML for all the presented measurements.

well approximated by a Doniach-Sunjic profile centered at 284.1 eV and with asymmetry α=0.09 [64]. The weak van der Waals C-Ir interaction is also reflected in the Ir4$f_{7/2}$ core level (left panel of Fig. 2.1) where the surface component, very sensitive to electronic interaction at the Ir(111) interface, is preserved.

Co intercalation occurs via annealing of a Gr/Ir(111) sample with pre-deposited Co atoms: at first, metallic Co is evaporated onto the Gr/Ir surface kept at room temperature, resulting in an overall reduction of the Ir4$f_{7/2}$ core level because of Co covering; then the sample is annealed up to 600 K, providing the Co atoms mobility to reach edges, defects and domain boundaries, through which they intercalate below the Gr sheet [65–68]. To shed more light on the intercalation process, we accurately monitored the evolution of the Ir4f (Fig. 2.2, left) and C1s (Fig. 2.2, right) core levels as a function of the annealing temperature, in a time-resolved XPS experiment. As previously mentioned, at RT the Co-covered Gr/Ir(111) sample presents reduced spectral intensity but with almost preserved lineshape, as reported in Fig. 2.2. At increasing annealing temperature the spectra smoothly evolve, with the reduction of the Ir4f surface component and the depletion of the sharp C1s feature at 284.1 eV. Concurrently, a double-peaked Gr/1 ML Co C1s core level develops, up to 600 K when the pre-deposited Co is fully intercalated. At the end of the process, the interface component of the Ir4$f_{7/2}$ core level is reduced and will be fully quenched at the completion of the first intercalated Co layer, without any further alteration of the spectral lineshape, ruling out any surface-alloy formation expected for Co intercalation obtained at higher annealing temperatures [69]. Likewise, the C1s spec-

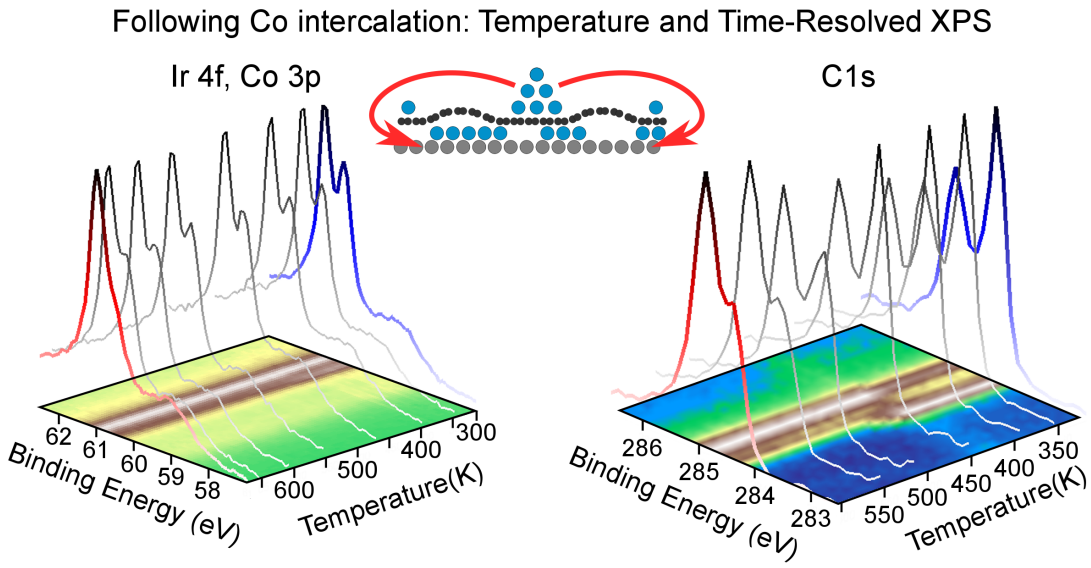

Figure 2.2: Ir4f (left) and C1s (right) time-resolved XPS, following Co intercalation as a function of the sample annealing temperature.

trum of Gr also evolves upon intercalation of Co: the single C1s component of bare Gr/Ir is quenched and replaced by two features, representing regions with different bonding strengths [66, 70, 71]. When a single Co layer is intercalated at the Gr-Ir(111) interface it arranges pseudomorphically to the Ir(111) surface, thus preserving the periodicity and symmetry of the Gr/Ir(111) moiré superstructure (as confirmed by the Low-Energy Electron Diffraction (LEED) pattern in Fig. 2.1) while, due to the stronger C-Co interaction, the corrugation is enhanced by a factor five (from 0.3 Å to 1.5 Å) [66, 70–73].

To elucidate the origins of the C1s core level of Gr/1 ML Co, theoretical Density Functional Theory (DFT) calculations were performed using the QUANTUM ESPRESSO package in the Local Density Approximation (LDA)[1]. Starting from a commensurate Gr-Co configuration, several registries, reported in the right part of Fig. 2.3, were considered, inspired by recent measurements on Gr/Co highlighting the presence of two C species depending on the adsorption sites on Co(0001) [70, 75]. However, both the experimental results and the computed core level shifts (left panel of Fig. 2.3) agree that the C-Co registry cannot justify such large separation and the moiré corrugation must be taken into account to reproduce the C1s core level. At first, since the description of the full moiré unit cell requires a huge computational effort, the influence of Gr-Co distance and relative registry was investigated within the so-called egg box model, in which the C atoms height

[1]Courtesy of Dr. Claudia Cardoso, Dr. Daniele Varsano and Dr. Andrea Ferretti.

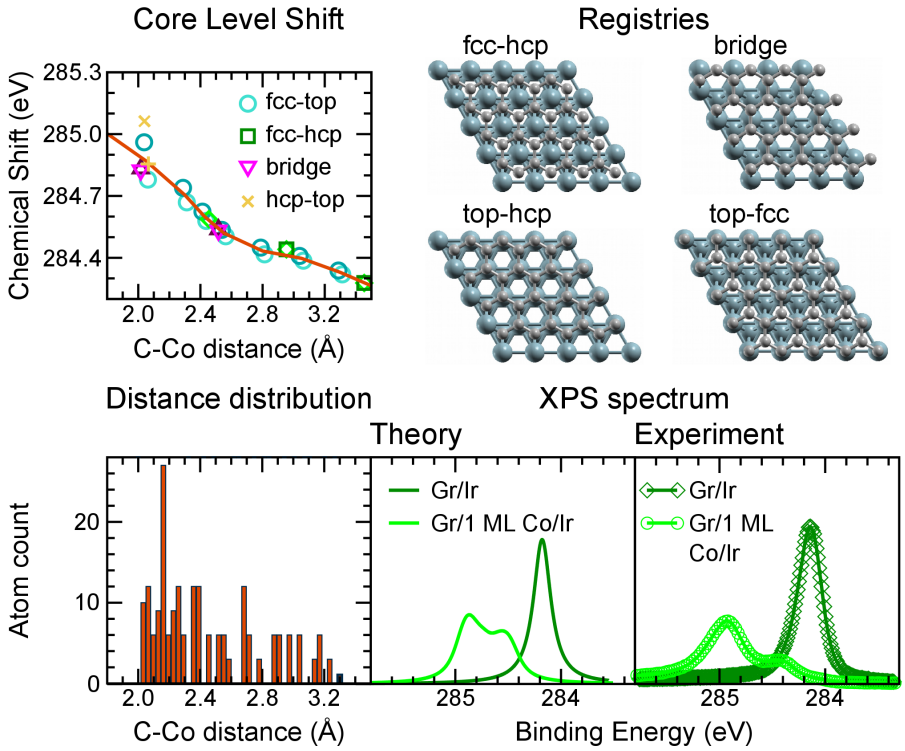

Figure 2.3: Top: Core level shift (left) computed for different registries (right) of Gr on Co layer(s) as a function of C-Co distance. Bottom: (left) C atoms height distribution within the moié unit cell; simulated (centre) and measured (right) XPS spectrum of Gr/Ir(111) (dark green curves) and Gr/1 ML Co/Ir(111) (light green curves). Figure adapted from Ref. [74].

distribution is given by:

$$h(\vec{r}) = h_{avg} + \frac{2}{9}\Delta h[\sum_{i=1}^{3} cos(\vec{k_i} \cdot \vec{r})] \tag{2.1.1}$$

with $\Delta h = h_{max} - h_{min}$, $h_{avg} = h_{min} + 1/3\Delta h$ assuming the values reported in Ref. [72] ($h_{max} = 3.29$ Å, $h_{min} = 2.02$ Å). With this model it was possible to extrapolate the C-Co distance distribution within the moiré cell (bottom left in Fig. 2.3) and, by using the core level shifts computed for commensurate Gr/Co at different C-Co distances (top left Fig. 2.3), the two peaks in the XPS spectrum were perfectly reproduced, as reported in the bottom part of Fig. 2.3. This confirms that they arise from the enhanced corrugation of Co-intercalated Gr. In particular, we observed the formation of two nonequivalent adsorption sites, namely valleys and hills, respectively being the regions closer to and further from the intercalated single Co layer. The component at 284.4 eV corresponds to C atoms weakly interacting with the Co-Ir support, hence it is attributed to the hill regions of the highly corrugated moiré superstructure, while the peak located at 284.9

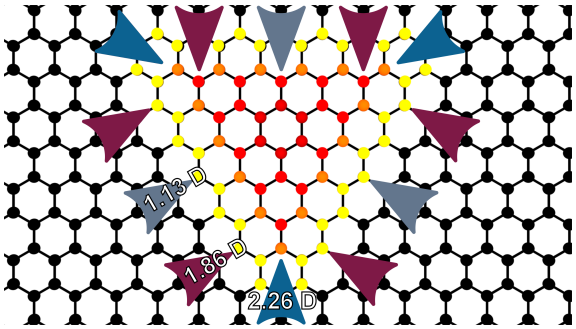

Figure 2.4: Sketch of the dipole formation for highly corrugated Gr/Ru(0001), as inspired by Ref. [81].

eV is ascribed to highly interacting C atoms placed closer to Co [70, 71]. The different intensity ratio is due to the fact that, even if the corrugation is between 1.2 and 1.8 Å, around 70% of Gr C atoms lie closer to the Co layer and, accordingly, the "valley" peak is three times more intense than the "hill" one, and accounts for the 74% of the total area [74]. Notably, these results were later confirmed by theoretical simulations of the full moiré superstructure, corresponding to 10×10 Gr plus 9×9 unit cells for the single Co layer and the Ir substrate [76].

The different bonding strengths experienced by the C atoms at different distances from the reactive metallic substrate induces a local modulation of the surface potential, with a work function variation of around 200 meV between the top and bridge sites of the moiré superstructure [77]. The enhanced corrugation, even if associated to only a tensile strain of the order of 1% as recently reported for Gr/Ru(0001) [78], produces a reorganization of the charge density distribution. As a consequence, lateral electric dipoles are formed, as sketched in Fig. 2.4. The strategical role of moiré patterns in driving the ordered self-assembly of adsorbed atoms [79, 80] and molecules [81, 82] can guarantee the long-range order of molecular spin networks.

At increasing quantity of intercalated Co, the film smoothly recovers the bulk Co (0001) configuration, almost commensurate to the Gr lattice. Intercalation of 6-8 ML Co can be performed step-by-step or all-at-once, giving the same results of high quality samples [51, 70]. In the left panel of Fig. 2.5, the evolution of the LEED pattern at increasing thickness of the intercalated film is reported. The moiré pattern of Gr/Ir(111) is gradually smeared out and the LEED pattern exhibits a 1×1 hexagonal structure upon completion of the sixth Co intercalated layer, indicating lattice mismatch relaxation and commensurate/flat Gr sheet on the Co thick film [70]. Concurrently, the two components of the C1s core

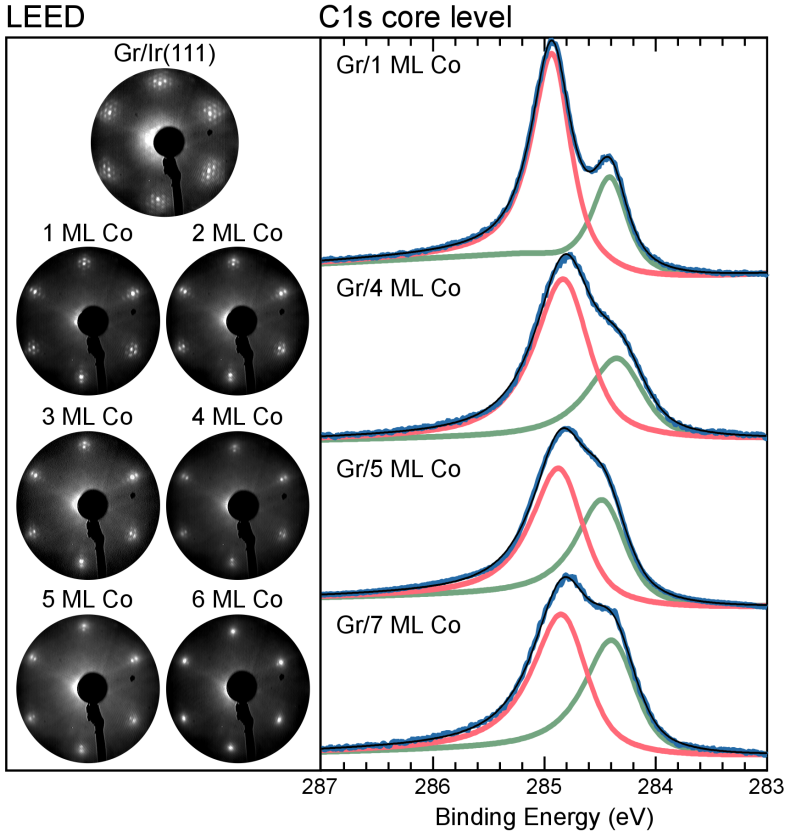

Figure 2.5: Evolution of the LEED pattern (left) and C1*s* core level (right) upon subsequent Co intercalation beneath the Gr sheet.

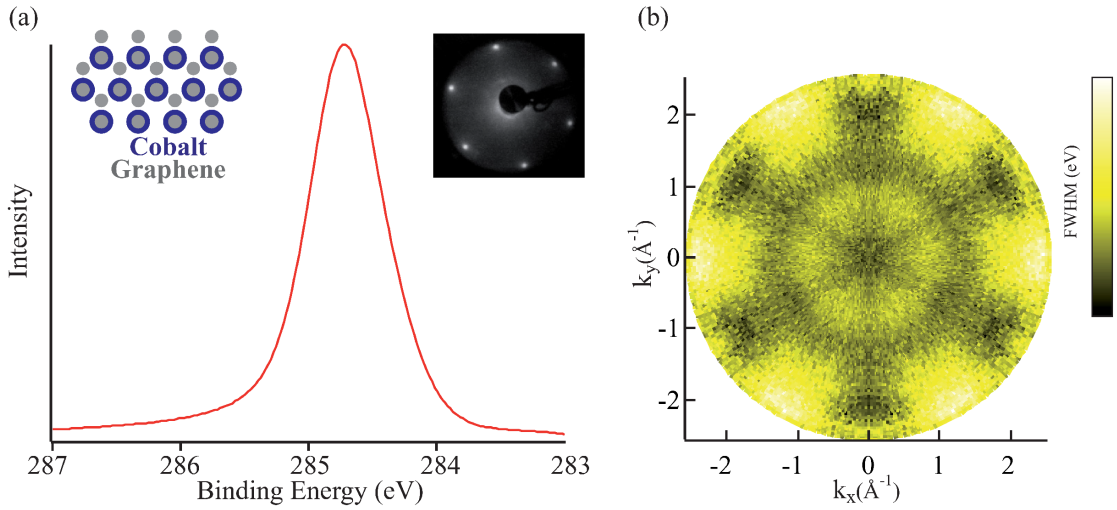

Figure 2.6: Gr/Co/W(110): (a) C1*s* core level ($h\nu$ 400 eV), the structural model (top-hollow) and the LEED (122 eV primary energy) are reported in the inset. (b) k-space image of the C1*s* full width at half maximum. Figure adapted from Ref. [70].

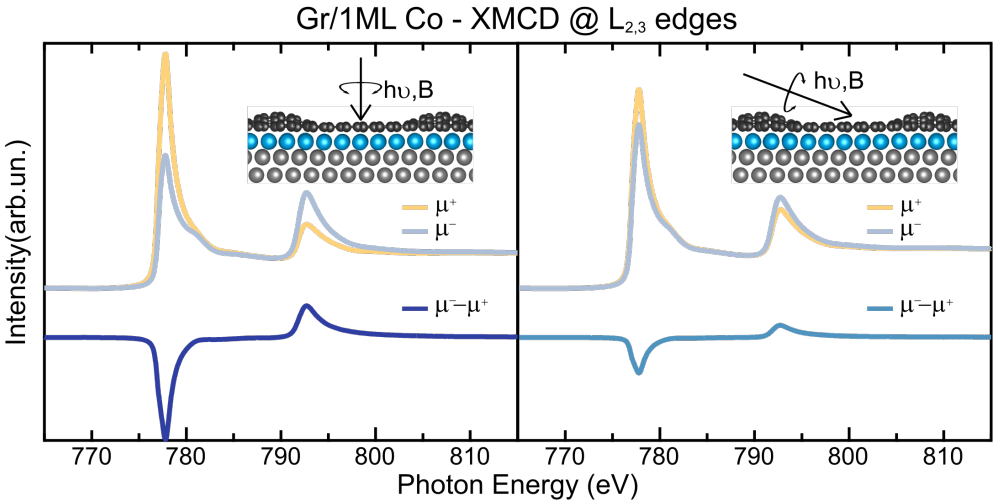

Figure 2.7: XMCD spectra at the $L_{2,3}$ absorption edges of Co for Gr/1 ML Co acquired at room temperature and in remanence condition both at normal (left) and grazing (right) incidence. The experimental geometry is sketched in the inset.

level, attributed to the C atoms in the valley or in the hill regions, approach each other and become of comparable intensity, towards the lineshape of Gr/Co(0001). In fact, the two peaks, separated by 270 meV [75], reflect the two equally populated adsorption sites of Gr on Co(0001), depending if a C atom lies on top of a first-layer (top site) or second-layer (hollow site) Co atom. This is confirmed by recent photoemission (Fig. 2.6 left) and photoelectron diffraction (Fig. 2.6 right) measurements of Gr directly grown on a 15 layer film of Co(0001) grown on W(110) [70]. The C1*s* core level is much broader (700 meV) than the sharp Doniach Sunjic profile of Gr/Ir (250 meV). Furthermore, the *k*-image of the Gr C1*s* core level highlights a 120 meV modulation of the peak width across the Gr Brillouin zone. The reported linewidth modulation was attributed to diffraction effects arising from different C sites during the photoemission process, ruling out the existence of one single component. The authors concluded that the two carbon sublattices occupy different adsorption sites in the 1×1 phase, associated to the presence of two main components [70].

2.1.2 The magnetic configuration

The magnetic state of ultrathin magnetic films can be investigated by means of XMCD measurements, that probe the spin imbalance of the empty magnetic states along the direction of the applied magnetic field, collinear with the X-ray beam. In Fig. 2.7 the XMCD spectrum acquired at room temperature and in remanence conditions, *i.e.*, after

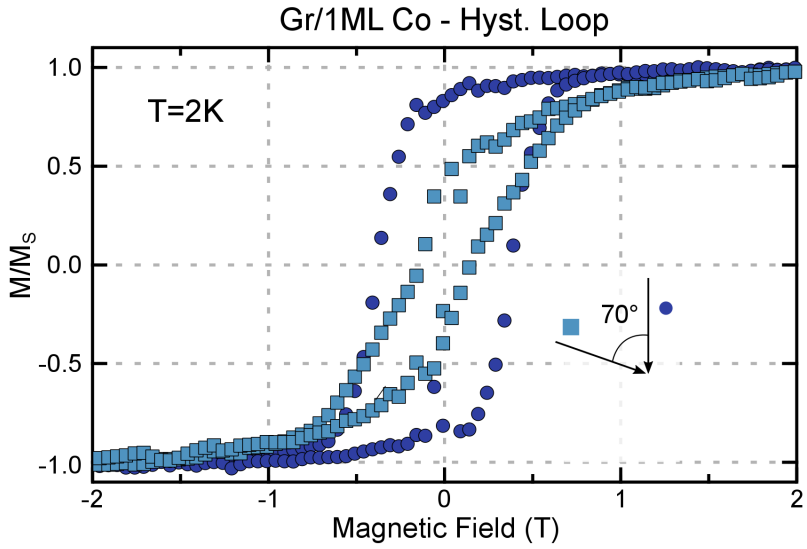

Figure 2.8: Field-dependent XMCD measurements at the Co L_3 edge, acquired at T= 3 K and normal (dark blue circles) and grazing (light blue squares) incidence for Gr/1 ML Co.

removing the 6 T magnetic field, is presented for the Gr/1 ML Co system both at Normal Incidence (NI) (left) and Grazing Incidence (GI) (right). The spectra consist of two sharp white lines separated by 15 eV, representing the transitions from the Co $2p_{3/2}$ (L_3 absorption edge at 778 eV) and $2p_{1/2}$ (L_2 edge at 793 eV) to the empty $3d$ states. By comparing the left and right panels of Fig. 2.7 it can be noticed that the remanent XMCD signal is about three times more intense when probed at NI than at GI. This indicates that this sample has a clear out-of-plane magnetic anisotropy, preferring to align the spins perpendicularly to the surface plane, in agreement with recent literature [71, 72, 83]. This picture is confirmed by the hysteresis loops acquired at NI and GI reported in Fig. 2.8. Indeed, Gr coating of Co layer(s) has proved to effectively enhance the PMA of Co ultrathin films, stabilizing it up to 4 Co layers. This was attributed to a fairly strong electronic interaction between the Gr π orbitals and the Co d_{z^2} state [70, 84], shifting them towards the Fermi level [83, 85]. The strange wasp-waisted shape of the field-dependent XMCD signal, acquired alogn the hard magnetization direction, can pinpoint towards complex magnetic domains contributing to the uni-axial magnetic anisotropy [86, 87], as this is usually attributed to the presence of magnetic domains exhibiting different coercivities [88–90].

On the other hand, when a thicker Co film is interposed between Gr and Ir(111), the Gr/Co substrate presents an in-plane magnetic anisotropy, resembling that of pristine Co(0001). In Fig. 2.9 we report the XMCD characterization of Gr/6 ML Co/Ir(111),

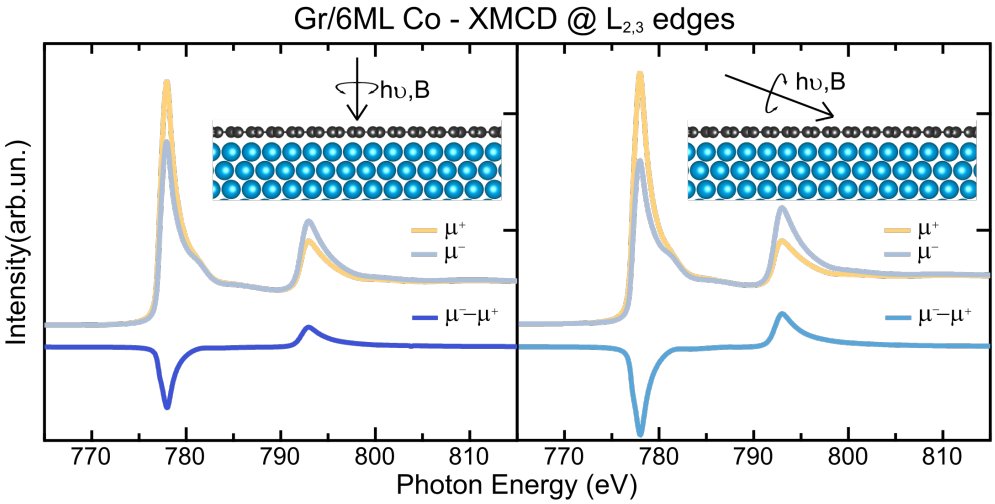

Figure 2.9: XMCD spectra at the $L_{2,3}$ absorption edges of Co for Gr/6 ML Co acquired at room temperature and in remanence condition both at normal (left) and grazing (right) incidence. The experimental geometry is sketched in the inset.

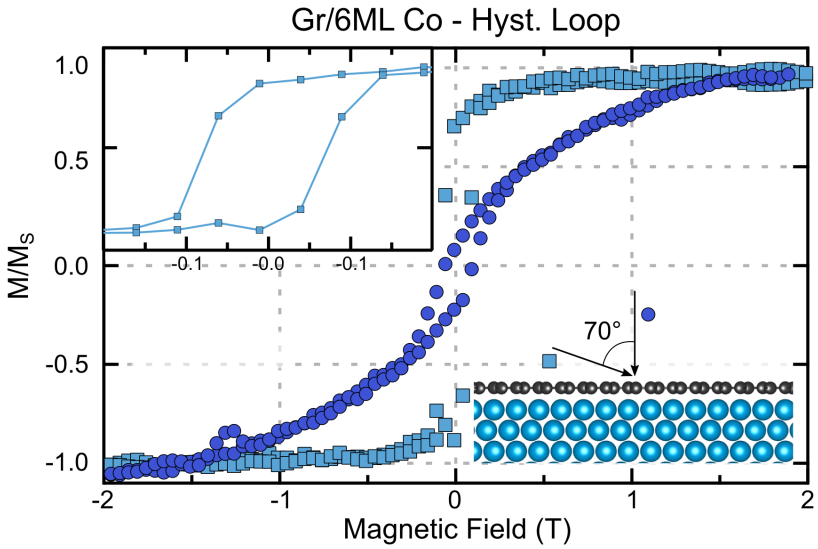

Figure 2.10: Co hysteresis loops, acquired at T= 3 K and normal (dark blue circles) and grazing (light blue squares) incidence for the Gr/6 ML Co sample. In the inset the details of the low-field trend is reported.

as acquired at room temperature and after removing the 6 T magnetic field. In this case a slightly more intense dichroism (50% higher) is observed when the photon beam impinges, and hence the magnetic field is applied, at 70° with respect to the surface normal. This clearly indicates that the magnetic anisotropy has changed, by only increasing Co coverage, from perpendicular to parallel to the sample surface. When Gr is grown oriented on a Co(0001) substrate, the electronic states of the Gr adlayer strongly hybridize with the extended states of the metallic substrate [91], giving rise to a 100% spin polarized

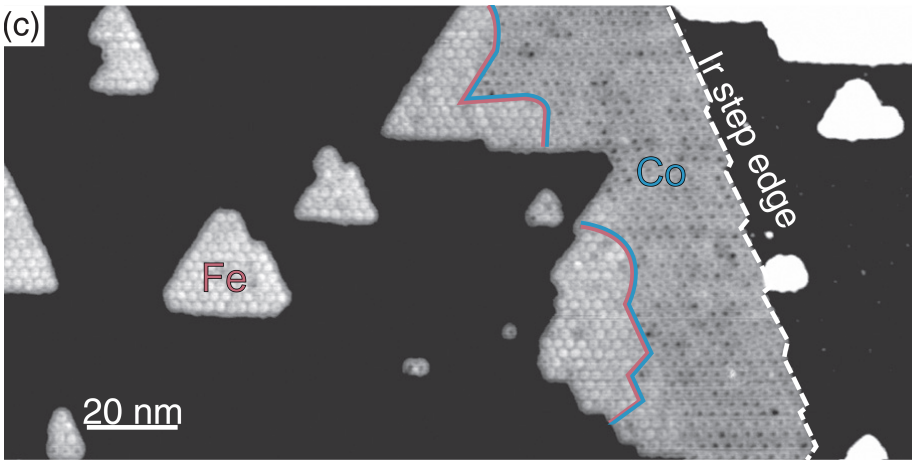

Figure 2.11: Scanning Tunneling Microscopy image of Gr intercalated with Fe and Co, image from Ref. [98]. The authors explain that, at the used bias voltage, Fe areas appear bright.

interface mini-cone. This state has significant contributions from both Gr π and Co $3d$ states and makes this substrate very interesting for spin transport applications [92, 93]. The possibility to further play with the magnetic activity of our Gr-based support, aiming at the ultimate optimization of the magnetic response of the adsorbed molecular spin network, will be discussed in the next section.

2.2 Simultaneous FeCo intercalation at the graphene/Ir(111) interface

The magnetic state of the Gr/ferromagnet substrate is a key ingredient to stabilize/optimize the response of the molecular architecture. It is well known that the ordered equiatomic FeCo alloy presents the highest magnetic moment among the known $3d$ ferromagnetic materials/alloys, a mandatory requirement for recording media [94]. Furthermore, an incredibly high Magnetic Anisotropy Energy (MAE) is found when the cubic symmetry is broken [95], for example by epitaxially growing FeCo films on suitable substrates [96]. When forced to arrange in an hexagonal pattern, Fe_xCo_{1-x} monolayers exhibit enhanced orbital magnetic moment and MAE close to the equiatomic composition, as a result of the change in the Fe and Co $d_{x^2-y^2}\downarrow$ and $d_{xy}\downarrow$ population [97].

Recently, a subsequent evaporation and intercalation of Fe and Co between Gr and Ir(111) has led to the formation of segregated Fe and Co islands, without alloy formation, as reported in Fig. 2.11 from Ref. [98]. In particular, the authors noticed that Co

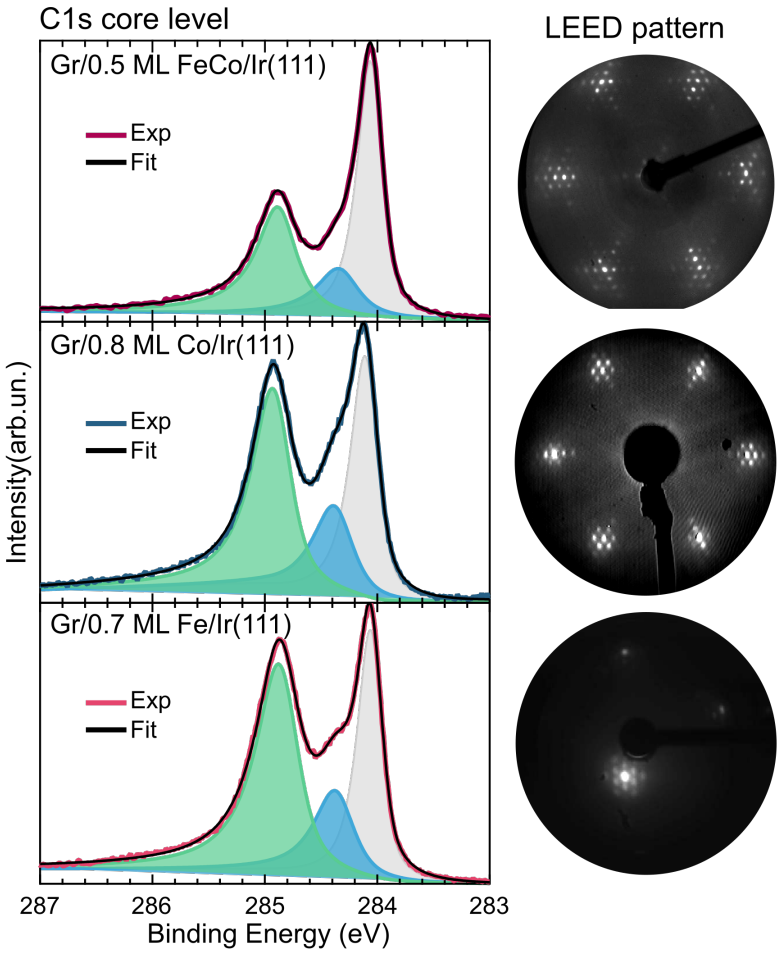

Figure 2.12: C1*s* core level (left) and LEED pattern (right) for 0.5 ML FeCo co-intercalated between the Gr sheet and the Ir(111) growth substrate (top). To ease comparison the XPS and LEED measurements are reported also for Gr/0.8 ML Co (center) and 0.7 ML Fe (bottom).

preferentially decorates Ir step edges, while Fe preferentially nucleates to form islands. We propose a different strategy: co-evaporating, at identical rates, metallic Fe and Co on the Gr/Ir sample kept at 500 K. This optimized procedure, established carefully selecting the substrate temperature and Fe, Co evaporation fluxes, results for the first time in a homogeneous and smooth intercalated FeCo film. Furthermore, intercalation below Gr ensures a better film quality, with respect to that grown by atomic-beam-epitaxy, without kinetically-limited interlayer diffusion usually leading to 3D growth (*i.e.*, cluster/aggregate formation).

First we want to shed light on the early growth stages of the Gr/FeCo/Ir(111) heterostructure, in order to verify if it is similar to what obtained for Gr/Co. To facilitate comparison we report in Fig. 2.12 the C1*s* core level for Gr intercalated with 0.5 ML

$Fe_{44}Co_{56}$ (top), 0.8 ML Co (centre) and 0.7 ML Fe (bottom). In all the three spectra we notice the co-existence of three features, the peak at 284.1 eV of the pristine Gr/Ir(111) and two new peaks at 284.4 eV and 284.9 eV, attributed to the Gr/FeCo (Fe,Co) sample. The binding energy and the lineshape of the intercalated regions resemble that of Gr intercalated with pure Co(Fe), indicating that the energetics of FeCo-intercalated Gr is similar to that of bare Co(Fe), with the presence of Gr regions undergoing different binding strength (valleys and hills). Furthermore, the energy separation between the valleys and hills contribution to the C1s core level, in very good agreement with what was measured for Gr/Co, suggest a similar moiré corrugation of 1.5–1.8 Å, in agreement with what is reported for Gr/Fe/Ir(111) [99]. The LEED patterns (right panel of Fig. 2.12) coincide with that of the Gr/Ir moiré superstructure for all the three cases, meaning that, at the early growth stages, the interatomic distance of the FeCo film stretches and adapts to the Ir(111) lattice parameter. We want to emphasize that the only information we have on the FeCo monolayer structure comes from the LEED measurements, hence we can safely claim that the growth is pseudomorphic to the Ir(111) surface, but not exclude the presence of structural dislocation induced by the high deposition temperature [97].

Before turning to the characterization of the magnetic properties of this peculiar substrate, we want to further investigate the electronic configuration at the interface with the Ir(111) surface. In the left panel of Fig. 2.13 we present the evolution of the Ir4f core level of the Gr/Ir substrate upon intercalation of Co (top), Fe (bottom) and FeCo (centre). We can notice that they follow the same trend proposed at the beginning of this chapter, with the quenching of the Ir surface state because of the strong metal-iridium interaction. Recently, J. Brede and coworkers [100] revealed that Fe interdiffuses in the Ir substrate, forming a superficial alloy, already at 600–650 K. The Fe-Ir alloying is reflected in a shift of the Ir4f(Fe2p) core level by around 150 meV towards lower(higher) binding energies. In order to avoid alloy formation, we kept the temperature well below 600 K during intercalation and, indeed, no evident shift can be appreciated in the experimental data (Fig. 2.13) for all the intercalated samples. In the right part of the Fig. 2.13 we report the Fe (bottom) and Co (top) 2p core levels, when co-evaporated (purple curve) and separately intercalated (red, Fe, and blue, Co, curves). No considerable alteration of the lineshape at the interface with the Ir(111) surface was observed, confirming that no Fe(Co)-Ir alloy is formed. It is worth noting that the success of the complete intercalation process was further checked by exposing the sample to 10^{-6} mbar of O_2 for 10 minutes

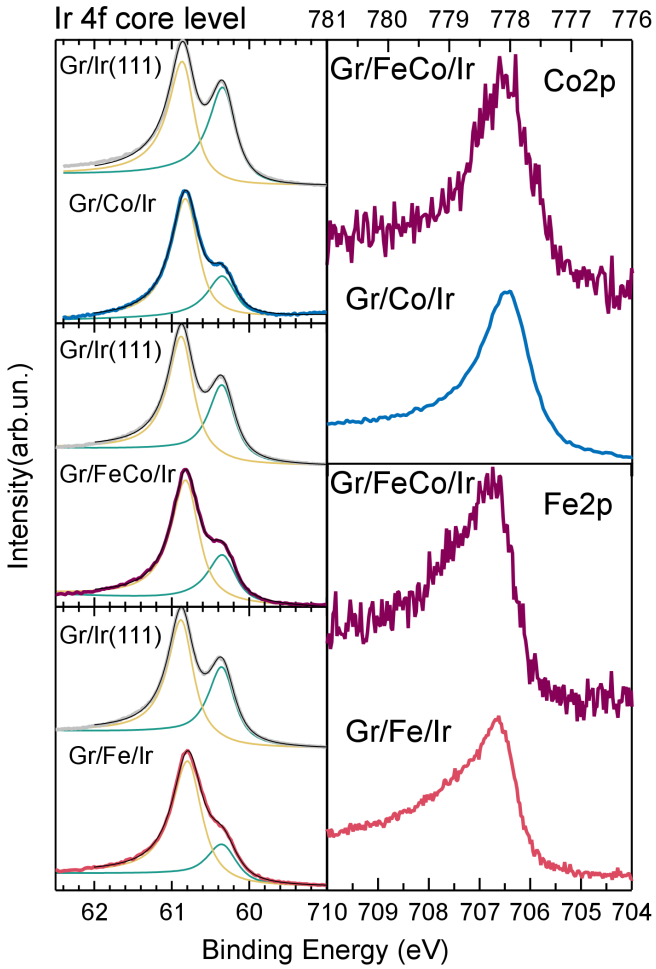

Figure 2.13: Left: Ir4f core level evolution from the bare Gr/Ir (grey curve in each panel) to the Gr intercalated with 0.8 ML Co (top), 0.5 ML FeCo (center) and 0.7 ML Fe (bottom). Right: Comparison between the Co (top) and Fe (bottom) 2p core levels when intercalated separately (blue and red curve, respectively) and at once (purple curve).

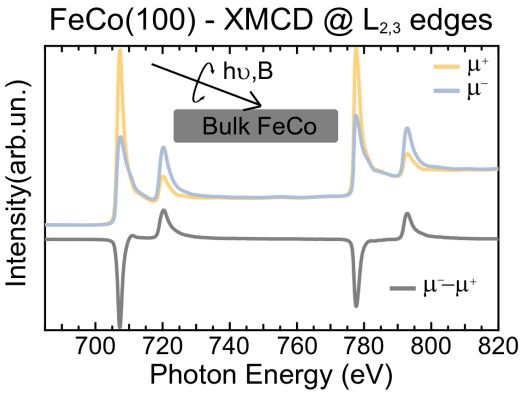

Figure 2.14: XMCD measurements at the Fe and Co $L_{2,3}$ absorption edges of a reference bulk sample: a FeCo single crystal oriented along the 100 surface. The spectra were acquired at room temperature and in a 0.7 T magnetic field and at GI.

and checking that no sign of oxidation arises neither in the absorption spectra nor in the magnetic dichroism measurements. This not only confirms the complete intercalation, but also the quality of the FeCo intercalated layers.

Turning to the magnetic properties of the Gr/FeCo substrate, we first describe, as a reference, the magnetic state of a FeCo single crystal oriented along the (100) surface. The spectra, acquired at room temperature and in a GI experimental geometry, are reported in Fig. 2.14 and consist of two sets of white lines: at 707 eV (L_3) and 720 eV (L_2) for transitions from the Fe $2p$ to the empty $3d$ states and at 778 eV (L_3) and 793 eV (L_2) for transitions located on the Co atoms. The spin and orbital contribution to the magnetic moment can be extracted from the experimental data according to the sum rules for the orbital (L) and effective spin (S_{eff}) moments, including the D term accounting for spin anisotropy within the atom [101, 102]:

$$L = -\frac{4}{3} n_h \frac{\int_{L_3+L_2}(\mu_- - \mu_+)dE}{\int_{L_3+L_2}\mu_- + \mu_+} = -\frac{4}{3} n_h \frac{q}{r} \tag{2.2.2}$$

$$S + 7D = -n_h \frac{6\int_{L_3}(\mu_- - \mu_+)dE - 4\int_{L_3+L_2}(\mu_- - \mu_+)dE}{\int_{L_3+L_2}(\mu_- + \mu_+)dE} = -n_h \frac{6p - 4q}{r} \tag{2.2.3}$$

where p,q and r are highlighted in Fig. 2.15 and n_h is the number of $3d$ holes, assumed to be 2.4 and 3.4 for Co and Fe, respectively [97]. The sum rules were applied at all the experimental spectra and the results are summarized in Tab.2.2. We also report the ratio L/S_{eff} to rule out any dependence on the considered number of holes, that can be altered by electron donation from Fe(Co) to the Gr adlayer and to the Ir support [103], thus favoring comparison with the existing literature.

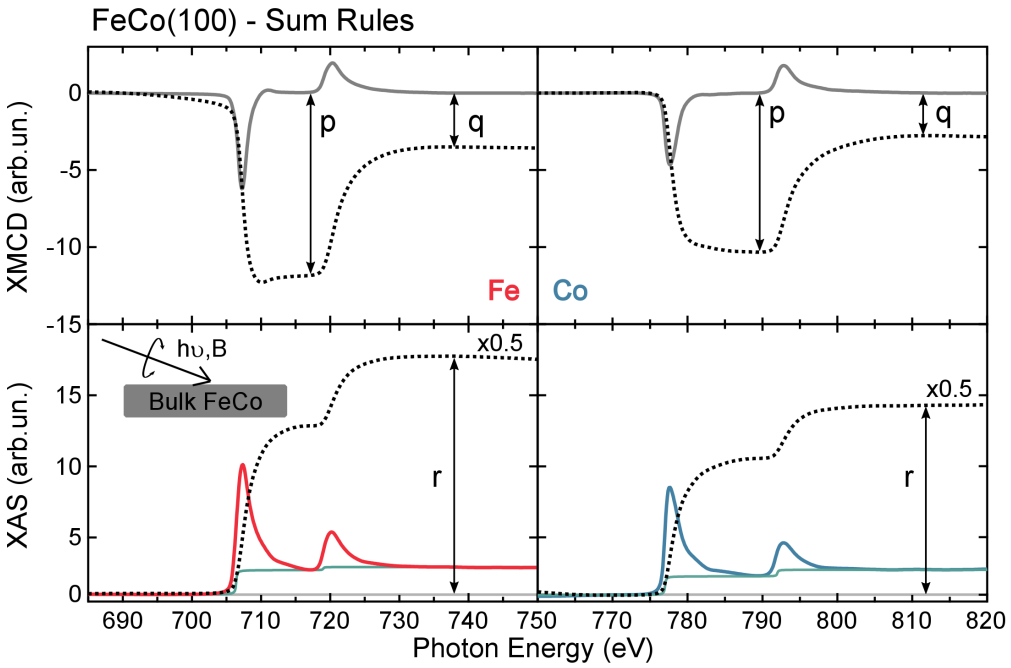

Figure 2.15: XAS (bottom) and XMCD (top) spectra at the Fe (left) and Co (right) $L_{2,3}$ absorption edges. Appended to the experimental data we report the XAS arctangent background (green lines) and the integrated signals (dashed black lines).

	Co μ_L	**Co μ_S**	**Fe μ_L**	**Fe μ_S**
bct $Fe_{0.4}Co_{0.6}$ [104]	0.15	1.73	0.10	2.20
bcc Fe [105]			0.09	1.98
hcp Co [105]	0.15	1.62		
bcc FeCo(100)	0.15	1.93	0.20	2.43

Table 2.1: Comparison between the spin and orbital magnetic moments of bct FeCo, pure Fe(Co) and of a single FeCo(100) crystal.

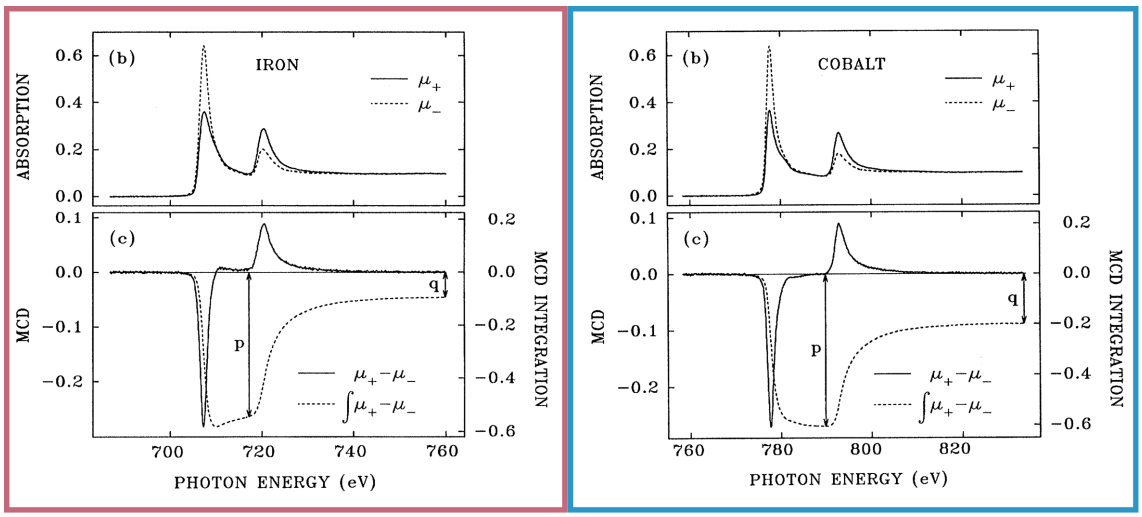

Figure 2.16: XMCD measurements at the $L_{2,3}$ absorption edges for bcc Fe (left) and hcp Co (right). Figure from Ref. [105].

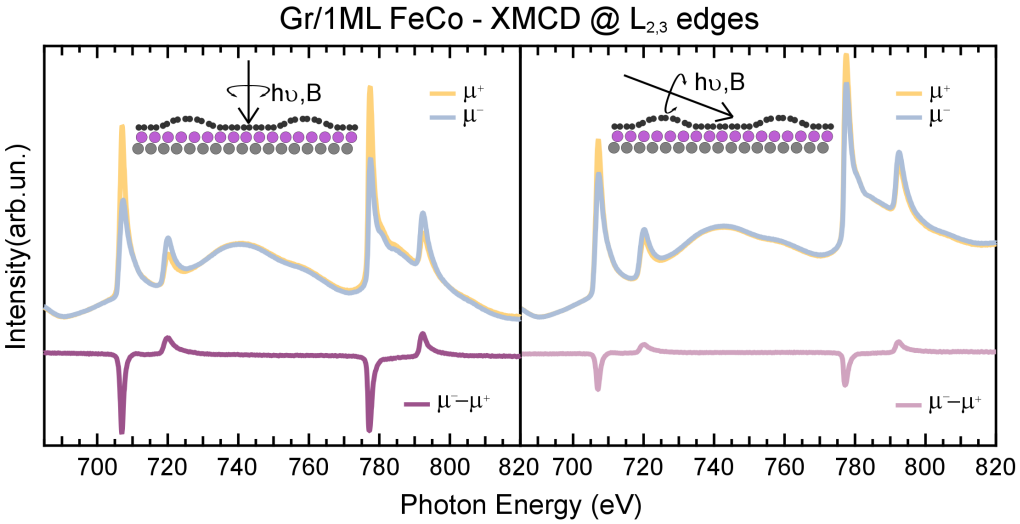

Figure 2.17: XMCD spectra at the $L_{2,3}$ absorption edges of Fe and Co for Gr/1 ML FeCo acquired at T= 3 K and in remanence condition both at normal (left) and grazing (right) incidence. The experimental geometry is sketched in the inset.

In Tab.2.1 we report the magnetic moment of our single FeCo crystal, as extrapolated by XMCD measurements, and of bcc Fe(hcp Co) from the literature. Notably, an enhancement of the total magnetic moment, from 2.07 μ_B (1.77 μ_B) to 2.63 μ_B (2.08 μ_B) for Fe(Co) can be observed. The increase in the Fe magnetic moment upon FeCo alloy formation is generally attributed to a strong hybridization between Fe, a weak ferromagnet, and Co, a strong ferromagnet with a filled $3d_{\uparrow}$ and an empty $3d_{\downarrow}$ bands. This induces a redistribution of the spin-polarized Fe $3d$ orbitals, from the spin minority to the spin majority band, transforming Fe in a strong ferromagnet [97, 106]. A steep increase in the MAE is also expected upon Fe-Co alloy formation. In particular, for bulk FeCo tetragonally-distorted [95] and epitaxial FeCo island on Pt(111) [107], the effect of Fe was to move the Fermi level down to the point where the spin-split d_{xy} and $d_{x^2-y^2}$ bands cross, maximizing the energy difference between the two magnetization directions.

XMCD measurements were performed for a single FeCo layer intercalated between Gr and Ir(111), both at GI and NI, and are presented in Fig. 2.17. The two sets of white lines are reproduced in this sample, with the same Fe and Co jump-edge ratios, hence confirming the intercalation of a nearly equiatomic alloy, with a slight excess of Co. Being the remanent dichroic signal more intense at NI (left) with respect to the GI (right) experiment, we can conclude that the single intercalated layer presents an out-of-plane easy magnetization axis, in agreement with what reported by G. Moulas and co-workers for hexagonally-arranged single FeCo layers, both smooth and granular, grown epitaxially on

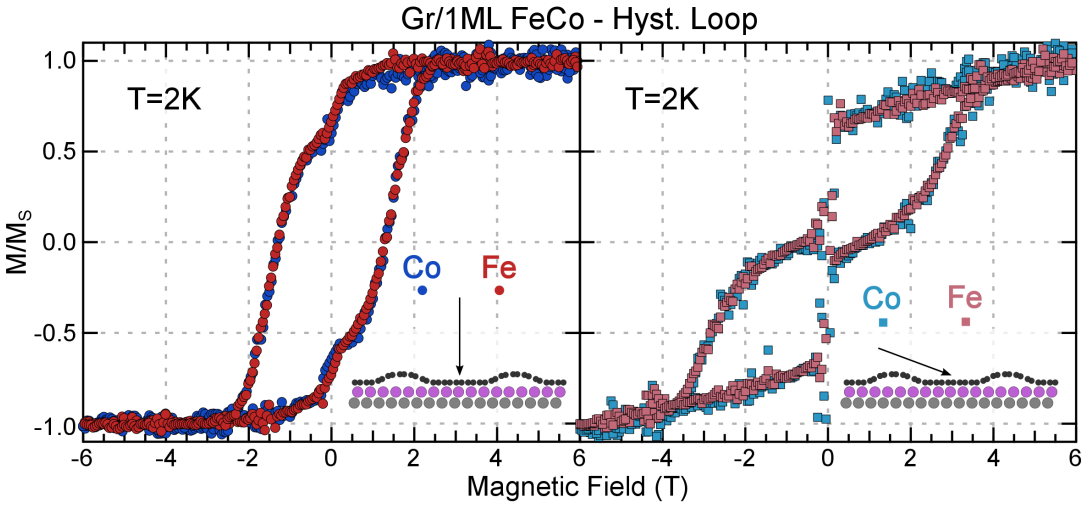

Figure 2.18: Element-selective hysteresis loops for the Gr/1 ML FeCo sample acquired at T= 3 K for Fe (red/pink) and Co (blue/light blue) at normal (left) and grazing (right) incidence.

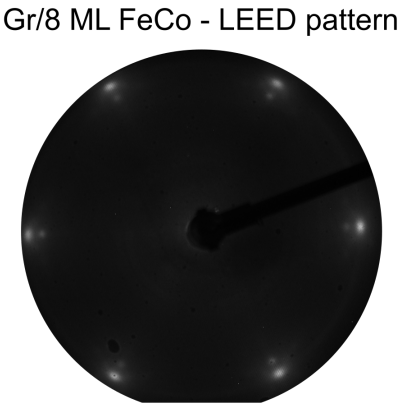

Figure 2.19: LEED pattern for 8 ML FeCo co-intercalated between the Gr sheet and the Ir(111) growth substrate.

Pt(111) [97]. Element-sensitive hysteresis loops acquired for Fe and Co in the two experimental geometries (Fig. 2.18 left and right panels) confirm this picture. Furthermore, the Fe and Co hysteresis loops perfectly mimic each other, suggesting a strong ferromagnetic (double)exchange coupling between the two species [106]. This definitely indicates that the two elements do not form independent segregated islands but do magnetically couple, forming a single magnetic unit. It is worth noting that the wasp-waisted character of the hysteresis loops, acquired along the hard magnetization axis (right panel of Fig. 2.18), is enhanced in this configuration, probably pinpointing to more complex magnetic domains in this stretched FeCo arrangement.

When a higher quantity (8 ML) of Fe and Co is co-intercalated beneath the Gr sheet,

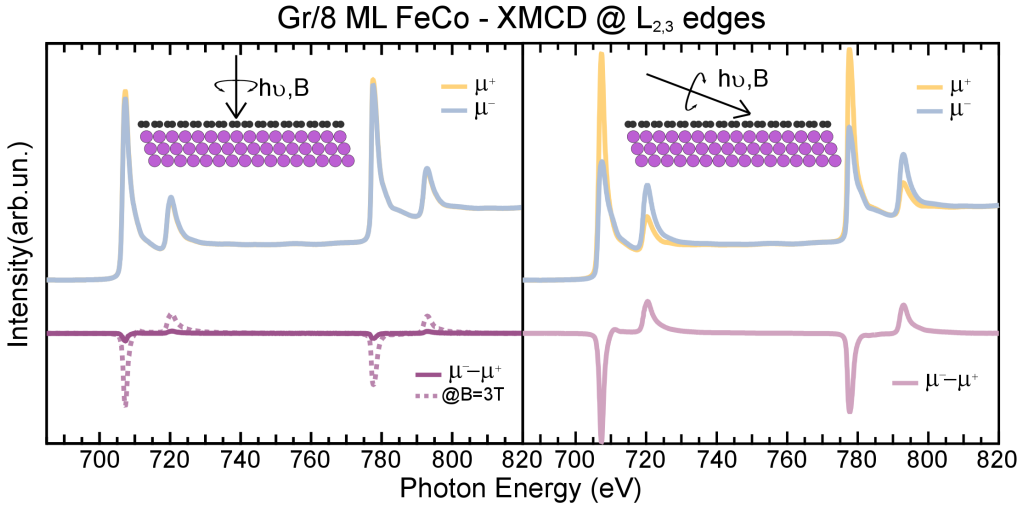

Figure 2.20: XMCD spectra at the $L_{2,3}$ absorption edges of Fe and Co for Gr/8 ML FeCo acquired at room temperature and in remanence condition both at normal (left) and grazing (right) incidence. The experimental geometry is sketched in the inset.

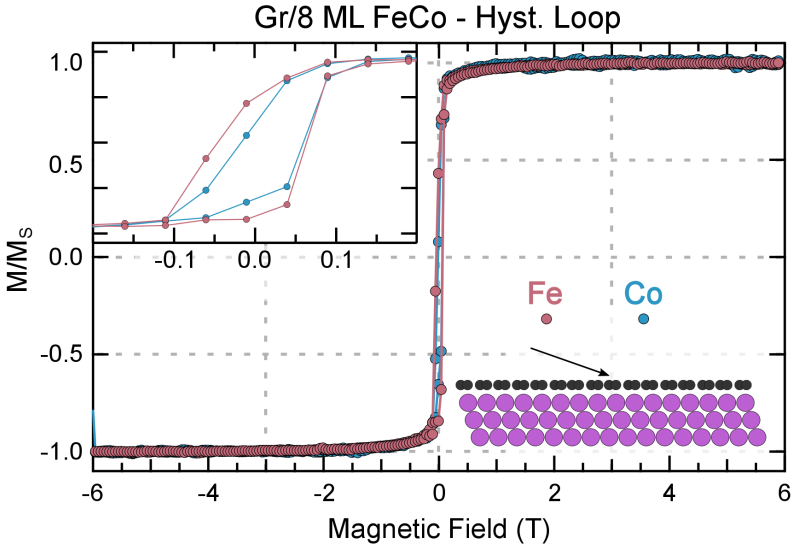

Figure 2.21: Element-selective hysteresis loops for the Gr/8 ML FeCo sample acquired at T= 3 K for Fe (pink) and Co (light blue) at grazing incidence, *i.e.*, along the easy magnetization axis.

the LEED pattern (Fig. 2.19) exhibits a structural arrangement commensurate with the Gr lattice, in agreement with what already described for Gr/Co. The moiré rippling is released and a FeCo film is formed almost commensurate with the Gr layer. Furthermore, the magnetic moments of the 8 ML FeCo intercalated alloy prefer to align parallel to the surface plane, indicating a tuning of the out-of/in-plane magnetic anisotropy for different FeCo thickness. In the left panel of Fig. 2.20, the XMCD spectrum, acquired applying a magnetic field of 3 T, highlights the small remanent signal, again probably due to the wasp-waisted hysteresis along the hard magnetization axis, due to the presence of complex magnetic domains *(i)* antiferromagnetically coupled or *(ii)* with different coercive fields [88–90]. The element-resolved hysteresis loops of Fe and Co acquired along the easy magnetization direction of the film confirm the coupling of the two magnetic species also at higher coverages.

Finally, we comment on the results of the spin and orbital moments as determined via the sum rules (Eqs. 2.2.2 and 2.2.3) applied to our experimental data. When a single Co layer is intercalated beneath Gr, both S_{eff} and L are enhanced with respect to their bulk value [105] because of the concomitant effects of reduced dimensionality and stretched lattice, and are fairly comparable with what is reported for Co islands on Pt(111) [5], Co monolayers on Rh(111) [108] and on Pt(111) [109], and what is theoretically predicted for Gr/Co [72]. When Fe and Co are co-intercalated beneath Gr, we observe an increase of both spin and orbital magnetic moments for Fe, as compared to the bulk values [105]. Furthermore, we remark an increase of a factor two in the L/S_{eff} ratio with respect to what is reported in the literature for a single Fe layer intercalated below Gr [103], while the magnetic properties of Co is not strongly affected by the presence of Fe atoms. When a higher quantity of FeCo is intercalated at the Gr/Ir interface, both the spin and the orbital magnetic moments of Fe are strongly enhanced with respect to bare Fe, with slightly reduced values compared to the single FeCo layer. In particular, $S_{eff}(L)$ increases from 1.95 μ_B (0.17 μ_B) for bare Gr/Fe to 2.86 μ_B (0.27 μ_B) for the Gr/FeCo sample. Notably, the magnetic moments of such (ultra)thin films are further increased with respect to the bulk FeCo sample (see Tab.2.1), because of reduced dimensionality effects as well as structural deformation induced by epitaxial growth on Gr/Ir.

	Co L	**Co** S_{eff}	Co L/S_{eff}	**Fe** L	**Fe** S_{eff}	Fe L/S_{eff}	average M
bcc FeCo(100)	0.15±0.03	1.93±0.13	0.08±0.02	0.20±0.06	2.43±0.21	0.08±0.03	2.36±0.43
IP Fe				0.17±0.03	1.95±0.17	0.09±0.02	2.12±0.20
IP Co	0.19±0.02	1.94±0.09	0.10±0.02				2.13±0.11
IP FeCo	0.22±0.04	2.13±0.18	0.10±0.03	0.27±0.08	2.86±0.27	0.09±0.04	2.74±0.57
OOP Co	0.26±0.06	1.98±0.11	0.13±0.04				2.24±0.17
OOP Fe [103]						0.049±0.01	
OOP FeCo	0.22±0.05	1.98±0.15	0.11±0.03	0.31±0.07	2.59±0.25	0.12±0.03	2.55±0.52

Table 2.2: Spin and orbital contribution to the magnetic moment, expressed in units of μ_B, of Fe and Co, as estimated via the sum rules, for the different investigated samples.

2.3 Conclusions

In this chapter we have thoroughly described the intercalation of $3d$ ferromagnetic metals/alloys beneath Gr, starting from the well-characterized Gr/Co interface and then proposing a viable route to optimize the Gr/ferromagnet magnetic state. In particular, *(i)* the enhanced corrugation of the Gr/1 ML Co(Fe, FeCo) induces a site-dependent polarization field, which can drive the self-assembly of the molecular units; *(ii)* it is possible to switch the easy magnetization direction by only increasing the amount of intercalated ferromagnetic metal/alloy, as deduced by angle-dependent XMCD measurements and *(iii)* by co-evaporating Fe and Co on a hot Gr/Ir(111) substrate, a magnetically coupled FeCo alloy is formed, exhibiting maximum magnetic moment because of both alloy formation and dimensionality effects. The structural growth of intercalated FeCo resembles that of pure Co(Fe), commensurate to the Ir(111) surface and to the Gr lattice, respectively at the early stages and for high (8 ML) FeCo quantity.

The ferromagnet-intercalated Gr substrate not only drives the self-assembly of the molecular adsorbates, providing a template for well-ordered spin architectures, but is the key enabler of the magnetic aligning. Maximizing the magnetic moment of the molecular support is then fundamental to further stabilize the magnetic state of molecular units against thermal fluctuations, up to device working temperature.

Chapter 3

Molecular architectures on Co-intercalated Gr/Ir(111)

Electronic interactions of adsorbed π conjugated planar molecules with metallic centers at the interface with a metal may induce charge transfer, distortion of the ligand field and reduction of electron-electron correlations because of hybridization with the metal extended states. Any alteration of the molecule structural/electronic configuration at the interface with the metallic support would affect the magnetic state of the molecular spin network. It is evident that a full understanding of the interaction mechanism, together with the possibility of disentangling the role of the organic ligands from that of the metal center, is of outermost importance to optimize the magnetic response of our graphene-supported TMPc molecular architectures. In this chapter we will investigate the long-range ordering and the adsorption geometry of FePc, Copper-Phthalocyanine (CuPc) and Manganese-Phthalocyanine (MnPc) adsorbed on Gr/Co, to prove that the peculiar Gr/Co substrate provides a suitable template to obtain spin networks with evenly spaced molecular building blocks. We will then study, with a combined X-ray absorption and photoemission spectroscopy approach, the Gr-mediated electronic interaction channels, separating the role of the common organic ligand and of the metallic centers with different occupation of the d metal states. Finally, we will examine the effects of the Gr corrugation, by monitoring the TMPc-Co interaction when the Gr sheet lies flat and commensurate on Co layers, with an increased C-Co distance.

TMPcs ($H_{16}C_{32}N_8TM$) are square-shaped planar molecules constituted by an organic cage (Pc) hosting at its centre a transition metal core, usually in a 2^+ oxidation state. The d states, immersed in a D_{4h} ligand field, split according to the irreducible symmetry representation as b_{2g} (d_{xy}), a_{1g} (d_{z^2}), two degenerate e_g orbitals ($d_{xz,yx}$) and the b_{1g} state ($d_{x^2-y^2}$), lying higher in energy [18]. Among all the TMs that can be placed at the centre of the Pc ring, we chose Mn, Fe and Cu, with different symmetry of the spin-polarized $3d$ metal states, as reported in Fig. 3.1. Indeed, the S=1 spin magnetic moment of isolated FePc molecules is carried by one of the two degenerate e_g orbitals and by the a_{1g} state, with a dominant out-of-plane character. On the other hand, CuPc has S=1/2 with only one single hole in the purely in-plane b_{1g} orbital, while MnPc, with its open d^5 shell and it S=3/2 spin ground state, presents a mixed character, with two half-filled molecular orbitals protruding out of the molecular plane (e_g and a_{1g}) and one unpaired spin in the b_{2g} state with planar symmetry [18].

In this chapter we will test the Gr-based magnetic template described in Chap.2 in driving the ordered assembly of the TMPc network, as well as in protecting the molecular electronic/magnetic configuration. To enlighten the open interaction channels, we will investigate the role of the different occupancy and symmetry of the molecular orbital carrying the magnetic moment in the Gr-mediated TMPc-Co electronic interaction.

3.1 Moiré-driven molecular self assembly

TMPc molecules are known to easily self-assemble in ordered architectures when deposited on suitable template surface. The adopted structural arrangement is mainly determined by their common organic cage, driven by a delicate balance between molecule-molecule and molecule-substrate interaction [111]. In particular, on reactive surfaces, e.g., Co, metal-organic molecules arrange in a random fashion, because of strong chemical interaction with the substrate that suppresses molecular diffusion [112]. On the other hand, on weakly interacting patterned surfaces, e.g., Au(110), TMPc deposition induces a $1\times$n reconstruction of the plastic gold surface to accommodate the molecules in a one-dimensional chain, as determined by P. Gargiani and co-workers for FePc, CoPc and CuPc in Ref. [31] and reported in Fig. 3.2. However, this configuration is associated with a reduction (FePc)/quenching (CoPc) of the molecular magnetic moments, since the out-of-plane protruding molecular orbitals get filled by electron injection from the gold surface [48]. In light of this, it is evident that decoupling the adsorbed molecules from the metallic surface is crucial to pre-

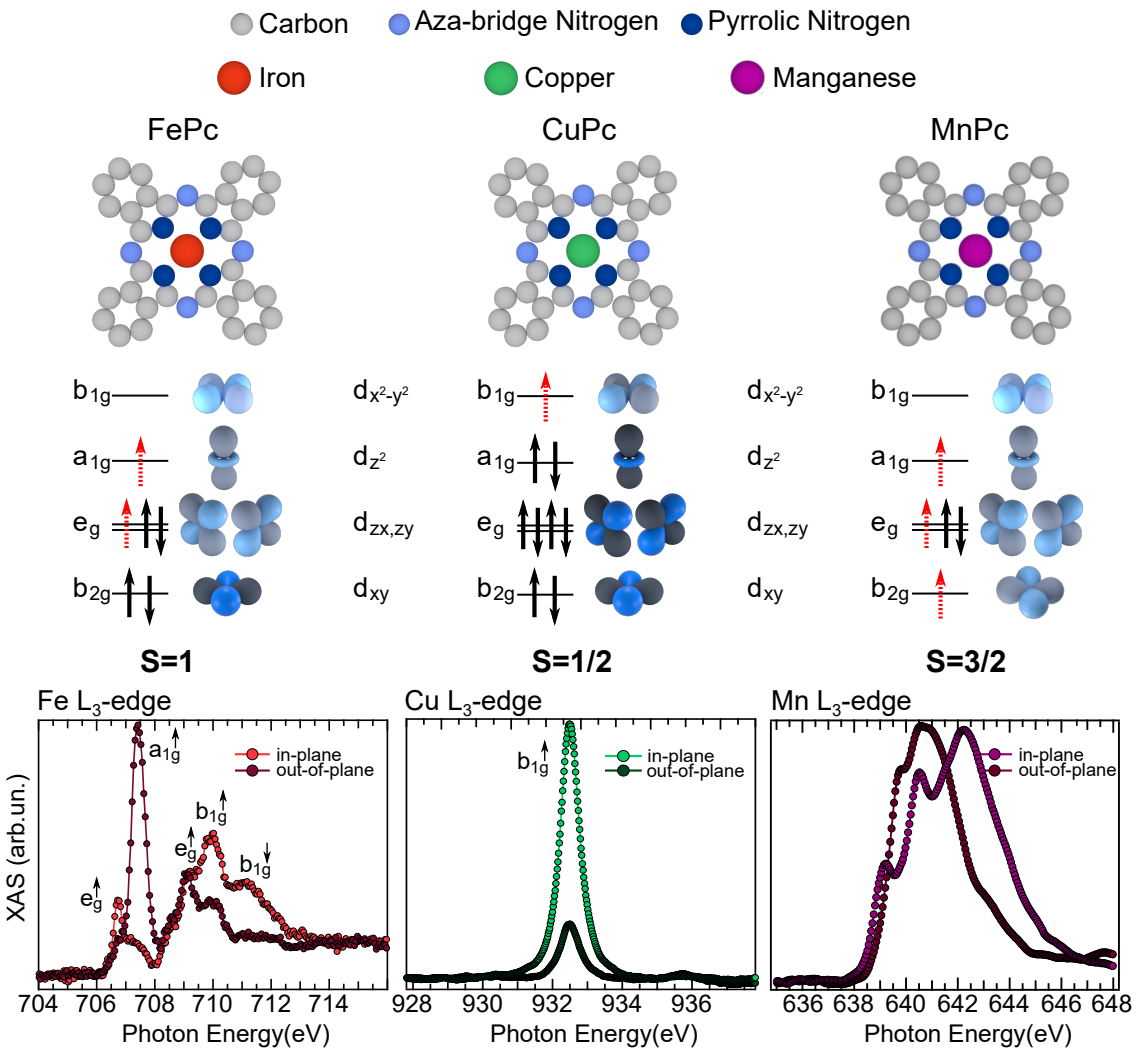

Figure 3.1: Electronic ground state configuration of TMPc (TM=Fe, left, Cu, center, Mn, right) molecules. In the upper panel a sketch of the the molecules and of the metal $3d$ states is presented. In the lower panel the X-ray absorption spectrum at the metal L_3 edges for thick TMPc films (TF) is presented, acquired with in-plane (lighter curve) and out-of-plane (darker curve) polarized radiation.

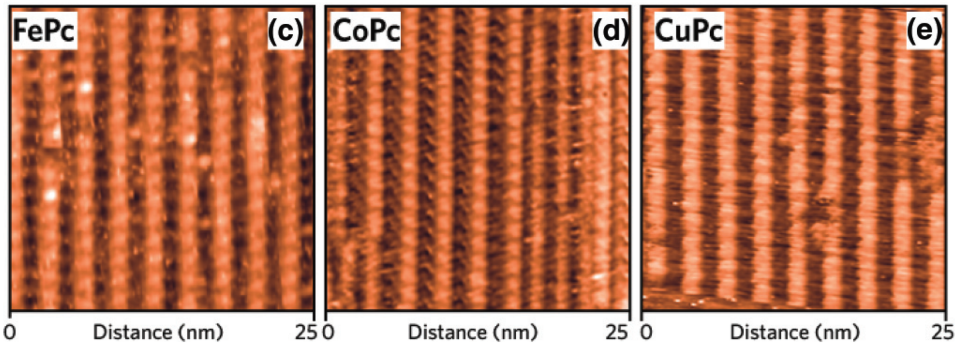

Figure 3.2: STM images of TMPcs (TM= Fe, left, Co, centre, Cu, right) self-assembled in nanochains on the reconstructed Au(110) surface. Image from Ref. [48].

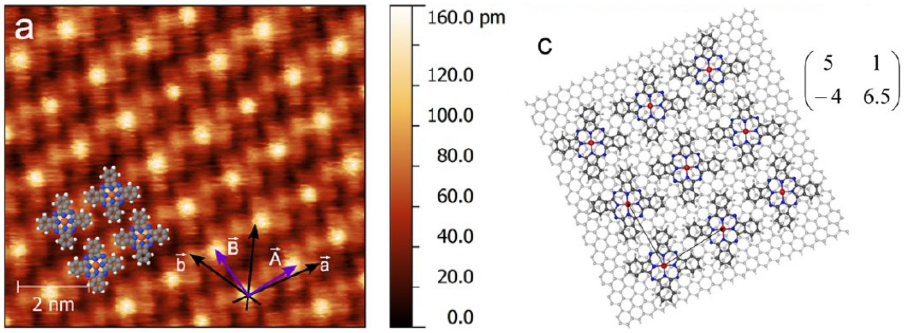

Figure 3.3: STM image (left) and structural model (right) for CoPc molecules adsorbed on pristine Gr/Ir. Figure from Ref. [110].

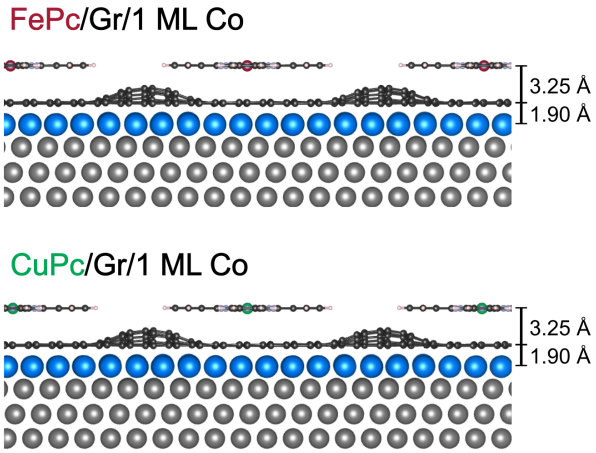

Figure 3.4: Theoretical simulations optimizing the geometry of the Gr/Co/Ir full moiré unit cell plus an adsorbed FePc (top) and CuPc (bottom) molecule.

serve the electronic/magnetic state of the molecular units, e.g., by interposing a Gr buffer layer between the adsorbed molecules and the metallic support [39, 58]. When TMPcs are adsorbed on the inert Gr/Ir(111) they weakly interact with the substrate and arrange in a square-shaped pattern, mainly driven by molecule-molecule interaction (Ref. [110] and Fig. 3.3). However, as detailed in the previous chapter, upon Co intercalation the Gr structure is strongly altered, presenting an enhanced rippling with a pronounced surface potential modulation depending on the C-Co distance. This highly corrugated support can act as an effective template to drive the long-range ordering of well-separated molecular units. In this section we want to investigate how the TMPc molecules arrange on the magnetic Gr-Co substrate, in order to determine whether they form an ordered spin network, driven by the presence of preferential adsorption sites, or not.

Theoretical structural relaxations[1] were carried out to predict the molecular arrange-

[1]Courtesy of Dr. Claudia Cardoso, Dr. Daniele Varsano and Dr. Andrea Ferretti.

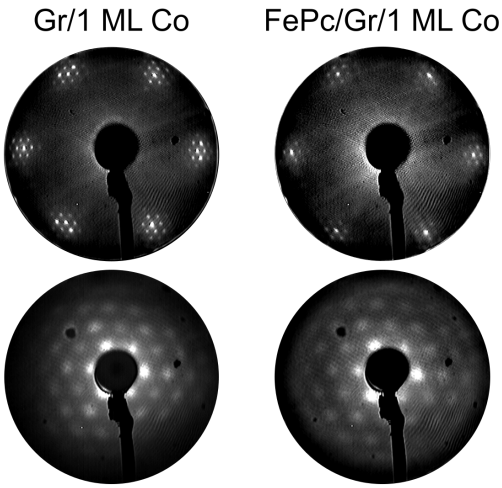

Figure 3.5: LEED pattern of Gr/1 ML Co before (left) and after (right) FePc deposition acquired with a primary beam energy of 140 eV (top) and 15 eV (bottom).

ment at the TMPc-Gr/Co interfaces, using DFT with the PBE exchange-correlation potential and including van der Waals interactions. The Gr/1 ML Co/Ir(111) system was simulated with a supercell consisting of a Co/Ir slab, made up by one Co and three Ir layers, with a 9×9 in-plane periodicity and an overlaying 10×10 graphene layer, also relaxed with one FePc (CuPc) molecule adsorbed on graphene. In the previous chapter we have mentioned that, upon intercalation of 1 ML Co, two inequivalent adsorption regions arise in the Gr sheet, namely valleys and hills depending on the C-Co distance, and could affect the arrangement of TMPc molecules at the early deposition stages. This picture was confirmed by theoretical calculations, confirming that the C-Co distance is the driving force of the surface potential modulation across the moiré unit cell. The geometry relaxation performed with the additional TMPc (TM= Fe, Cu) molecule revealed a similar adsorption configuration for FePc and CuPc: trapped in the valley site of the Gr/1 ML Co moiré and sitting at a distance of 3.1-3.2 Å (slightly depending on the considered exchange functional), flat-lying with the molecular plane parallel to the sample surface, in agreement with recent STM results [113]. This indicates that the adsorption configuration is independent of the central transition metal ion, confirming recent experiments on TMPcs deposited on Gr/Ir(111) revealing a comparable desorption temperature for TM= Fe, Co, Cu, suggesting a negligible contribution of the central metal ion and a dominance of van der Waals-like interactions [49].

In Fig. 3.5 we report the LEED patterns acquired for pristine (left) and FePc-covered (right) Gr/1 ML Co. The LEED pattern is typical of moiré superstructures, with satellite

spots associated to the superlattice, and is only slightly smeared but not altered, both for high (top) and low (bottom) primary beam energy, upon FePc adsorption. This is a first evidence that the molecules adapt to and preserve the long-range order of the surface [74], as also determined for CuPc and MnPc on Gr/1 ML Co, for which similar measurements were performed.

In order to confirm the trapping of TMPc molecules on the valley regions of the Co-intercalated Gr substrate, we monitored the evolution of the C1s core level at increasing molecular coverage, to address how the inequivalent C sites are affected by the molecular deposition. In the left panel of Fig. 3.6 the C1s core level at increasing molecular density is presented, while the detailed analysis of the XPS spectrum for 0.2-0.3 ML[2] TMPc on Gr/1 ML Co is reported in the central panel of the same figure. The spectral lineshape is common to all the samples: the two peaks of the corrugated Gr sheet (valleys at 284.9 eV and hills at 284.4 eV, following the fit procedure detailed in Sec.2.1.1) and the molecular contributions from the C atoms in the benzene (C_B) and pyrrole rings (C_P) together with their less intense shake-up satellites [39, 114, 115]. The details of the fitting curves are summarized in Tab.3.1. It can be noticed that the C_B-C_P separation decreases from 1.6 eV for CuPc [114] through 1.4 eV for FePc [116] to 1.1 eV for MnPc [115], indicating that lowering the occupation of the d orbitals makes the two C species less inequivalent. This splitting evolution for different filling of the 3d states can be attributed to an increasing hybridization of the metal and ligands e_g wavefunctions, that for MnPc and FePc lie very close in energy [117] and significantly mix [118].

In the right panel of Fig. 3.6 the evolution of the relative intensity of the C1s peaks attributed to Gr C atoms strongly (valley, blu) and weakly (hill, pink) bonded to the Co monolayer is reported. It is well-known that, in a layer-by-layer growth approximation, the intensity of a core level peak decreases at increasing thickness of the adsorbate film according to $I = I_0 e^{-d/\lambda cos(\theta)}$ (see Sec.A.2.1 and Ref. [119]). In particular, I and I_0 are the peak intensity of the covered and pristine sample, respectively, d is the thickness of the adlayer, λ is the inelastic electron mean free path, and θ is the angle between the surface normal and the escaping direction of the collected photoelectrons. Hence, if the Gr/1 ML Co substrate provides non equivalent adsorption sites, their evolution at increasing TMPc coverage would follow different trends. Indeed, we can notice that only the peak associated

[2]The complete monolayer is here defined as in Ref. [110], as a compact square packing densely covering the Gr sheet.

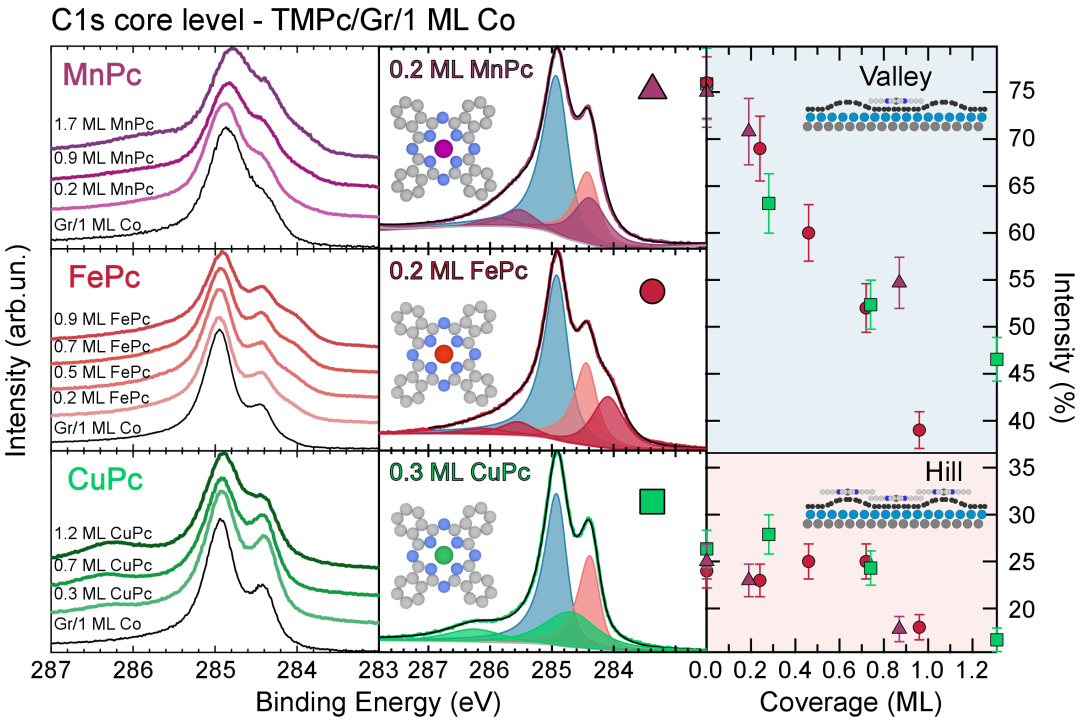

Figure 3.6: Left: C1*s* core level evolution from the bare Gr/Co (black) at increasing molecular density. Center: selected C1*s* core level and fitting curves of 0.2-0.3 ML TMPc, TM= Mn (top), Fe (center), Cu (bottom). Right: Evolution of the Gr-related C1*s* components at increasing TMPc coverage, TM= Mn (triangles), Fe (circles) and Cu (squares).

to the valleys of the Gr-Co is reduced for molecular coverages up to 0.7-0.8 ML, indicating that the molecules preferentially occupy the valley sites, leaving the hills uncovered. Only once the valleys are filled, at around 0.7-0.8 ML, they start to adsorb on the hills of the highly corrugated moiré [74].

The molecules trapped in the valley sites of the rippled Gr layer are expected to adsorb flat-lying with the molecular plane parallel to the surface. This prediction is confirmed by exploiting X-ray search-like-light effect at the N K absorption edge. Linearly polarized radiation can select molecular orbitals with symmetry matching the polarization vector, hence allowing for the determination of the (eventual) tilting angle when the molecular orbitals have a distinct dipolar character [120]. In Fig. 3.7 we present the NEXAFS spectra at the N K absorption edge for TMPc (TM=Mn, Fe, Cu) adsorbed on Gr intercalated with 1 ML Co (left), in comparison with a thick molecular film (right, see Fig. 3.7 for film thicknesses). All the spectra can be divided in two energy regions: the first one, ranging from 398 eV to 405-406 eV photon energy, dominated by the transition from the N1*s* core level to the empty states with π^* symmetry, and the second one above

Peak	BE (eV) (±0.1 eV)	FWHM (eV) (±0.1 eV)	Intensity %
	MnPc		
C_B	284.4	0.6	1.00
C_P	285.5	0.6	0.35
	FePc		
C_B	284.1	0.6	1.00
C_P	285.5	0.6	0.28
	CuPc		
C_B	284.7	0.7	1.00
C_P	286.3	0.7	0.37

Table 3.1: Fitting parameters of the pseudo-Voigt components used to model the molecular contribution to the C1s core level of 0.2-0.3 ML TMPc/Gr/1 ML Co, data in Fig. 3.6.

406 eV where the final states have a specific σ^* character. The main spectral features are common to all the TMPc molecules: there is a first doublet (unresolved for FePc and CuPc) accounting for transitions from the 1s core level of the two inequivalent N_{aza} and N_{pyr} atoms to the Lowest Unoccupied Molecular Orbital (LUMO), with a mixed C $2p_\pi$- N $2p_\pi$ character and highly delocalized over the Pc ring. The distance between the *pyrrole* contribution and the *aza-bridge* one is strongly dependent on the central transition metal ion, decreasing at increasing occupation of the 3d levels. This is a fingerprint of stronger ligand-metal hybridization for open 3d shells, affecting the electronic environment surrounding the N atoms bonded to the metal centre [121, 122]. The second feature, at around 1 eV higher photon energy, can also be decomposed in two contributions attributed to the $N_{aza/pyr}$ →LUMO+1 transitions, while the third feature is associated to excitations towards a C-based molecular orbital with small N 2π contribution [121]. Furthermore, we notice in the low photon energy range a residual σ^* signal for all the three TMPcs, both at the interface with Gr/Co and in a thick molecular film. This can be attributed to a LUMO rehybridization [123] as well as to the dipole-allowed $e_u \rightarrow b_{1g}$ transition [124], and/or to a minor distortion of the organic backbone upon adsorption [124–126]. However, the observed slight intermixing is not even comparable to what observed for TMPc adsorbed directly on metal surfaces, e.g, FePc on Co(001) [127] or MnPc on Ni(111) [115], where a definite molecular deformation/fragmentation due to the interaction with the metallic substrate induces a significant distortion of the molecular structure [128].

The pronounced dichroic response when the system is excited with horizontally and vertically polarized radiation confirms the flat-lying adsorption geometry of TMPcs and, since the electronic interaction is screened by the presence of the graphene buffer layer,

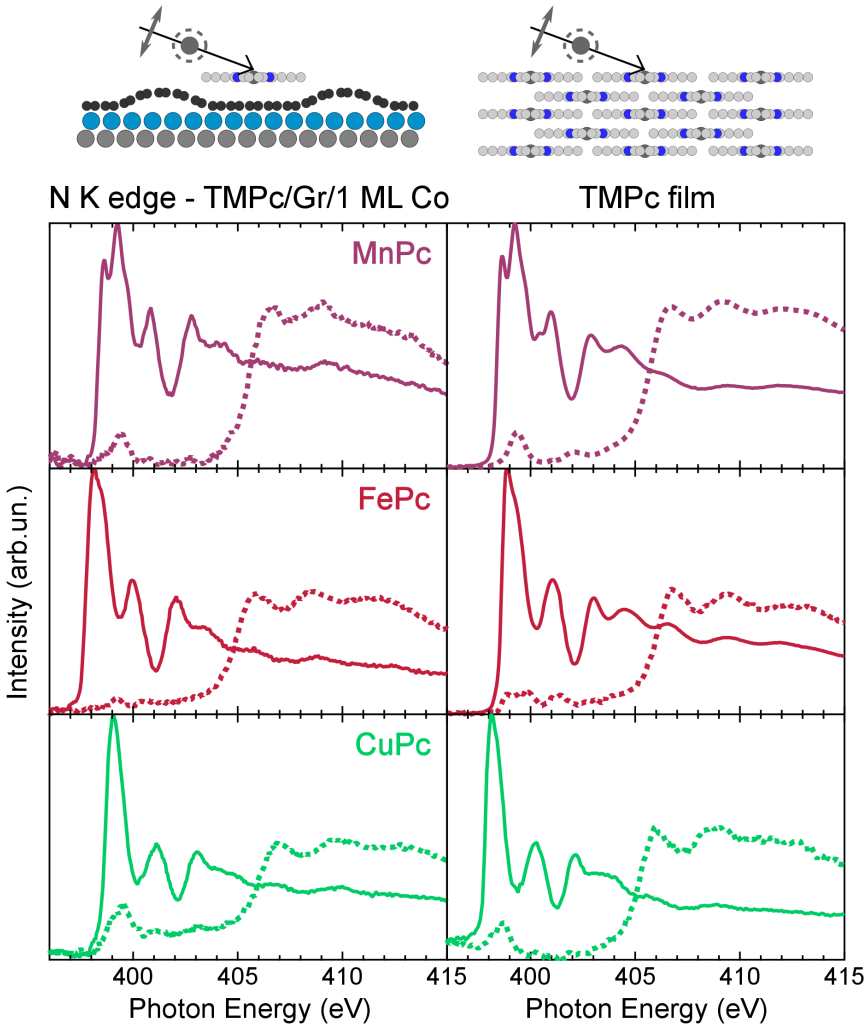

Figure 3.7: NEXAFS measurements at the N K-edge for TMPcs, TM= Mn (top), Fe (center), Cu (bottom) deposited on Gr/1 ML Co (left), compared with a thick molecular film (right, film thickness: 30 Å for MnPc and FePc, and 20 Å for CuPc). Experimental geometry in the top part of the figure.

without distortion (e.g enlargement of the molecular ring, elongation of the bond lengths, tilting of the ligands etc...) as is indeed observed when TMPcs are adsorbed directly on a ferromagnet [129, 130]. These findings confirm what is theoretically predicted, indicating that the highly corrugated moiré superstructure effectively acts as a template to drive the ordered assembly of intact, flat, well-separated, and periodically arranged TMPc molecular spin units.

3.2 TMPc-Co interaction mediated by highly corrugated graphene

The Gr sheet effectively screens the molecule-Ir(111) electronic interaction, preserving the electronic/magnetic state and structural configuration of the molecular units upon adsorption, as deduced by the X-ray absorption response at the C and N K absorption edge at increasing FePc density on Gr/Ir reported in Ref.39,58. However, the effectiveness of the Gr decoupling role strongly depends on the graphene-support interaction. In particular, L. Massimi and co-workers recently reported the appearance of an interface state when FePc are in contact with Gr/Ni(111), attributed to a non-perfectly screened charge transfer from the Ni(111) surface to the Fe d states, through the Gr spacer [131]. In this section we will investigate the TMPc-Co electronic interaction, mediated by a Gr sheet strongly interacting with the intercalated Co layer [70], disentangling the effects of the common organic cage from that of the central metal ion, for different occupancy and symmetry of the $3d$ metal states.

When TMPc molecules are directly adsorbed on metallic surfaces the N and C K-edge absorption spectra are strongly modified because of molecule-substrate interaction [123, 127] and/or molecule fragmentation upon adsorption [115]. We expect that, by interposing the inert Gr between TMPc molecules and reactive Co layer(s), we are able to screen the electronic interaction and protect the structure of the molecular backbone from being deformed upon adsorption.

The NEXAFS measurements at the N K absorption edge for CuPc at the interface with highly corrugated Gr/Co fully resembles that of a 20 Å-thick molecular film, proving the efficient electronic decoupling mediated by the Gr buffer layer, as reported in the bottom panel of Fig. 3.7. The N K absorption spectrum of FePc/Gr/Co, central panel of Fig. 3.7, present only a slight changing in the intensity ratio of the out-of-plane features, without any evidence for a strong N-mediated charge transfer/orbital intermixing. Finally, in the top panel of Fig. 3.7 we report the NEXAFS spectrum at the N K-edge acquired for MnPc molecules interfaced with Gr/Co. The spectral linehsape exhibits no dramatic change in the position, width and sequence of the spectral features, pinpointing to a preservation of the ground state configuration. Notably, no shift in the edge onset, fingerprint of strong Mn-Co interaction [123], is observed.

Further details on the electronic interaction channels involving the common organic

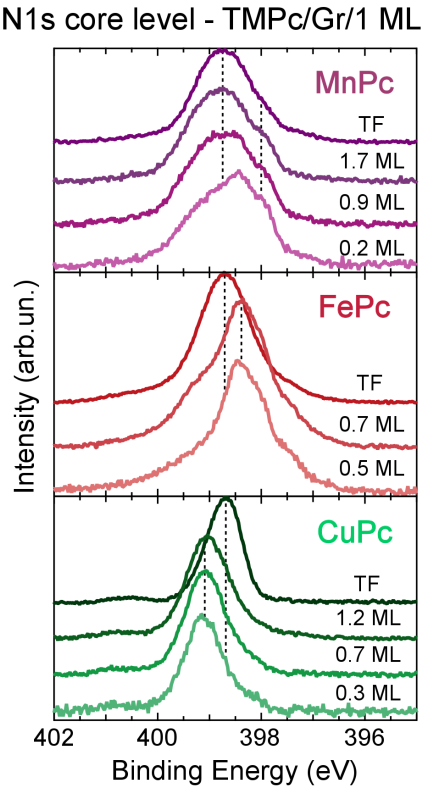

Figure 3.8: N1*s* core level for TMPcs, TM= Mn (top), Fe (center), Cu (bottom) deposited on Gr/1 ML (top) at increasing molecular coverage, up to 30 Å for MnPc and FePc and 20 Å for CuPc.

macrocycle can be disclosed by photoemission spectropscopy experiments performed at the N1*s* core level. In Fig. 3.8 the N1*s* core level acquired at increasing TMPc density are presented and compared with the spectrum of a thick molecular film. The N1*s* spectrum of TMPc films (darker curve in Fig. 3.8) exhibits a symmetric lineshape that can be deconvoluted in two equally intense features, representing the four *pyrrolic* and four *aza-bridge* N atoms experiencing a slightly different electronic environment, as already noticed in the N K-edge NEXAFS measurements.

CuPc molecules at the interface with the rippled Gr/Co support exhibit a N1*s* XPS spectrum (bottom panel of Fig. 3.8) with preserved symmetric lineshape, but blueshifted by 0.5 eV with respect to the 20 Å-thick film. The evolution at increasing molecular density reveals the developing of spectral weight at low binding energies, indicating that the blueshifting arises from CuPc molecules in contact with the Gr/Co support. This is in contrast with experiments on CuPc deposited on more interacting substrates, e.g., Au [132], Al [133], and Co [134], where a smaller shift (∼0.3 eV) towards lower binding energies can be ascribed to charge screened by the surface and/or weaker electronic interaction. This

suggests a different kind of electronic interaction and/or different screening/polarization effects at the interface with Gr, that can be also affected by Gr interacting with the Co substrate [135].

The N1*s* spectrum of FePc molecules deposited on Gr/1 ML Co (central panel of Fig. 3.8) presents an overall shift of the spectral weight towards lower binding energies accompanied by a deformation of the core level lineshape, with a complex superposition of different contributions. When the valley sites are filled and FePc molecules start to adsorb on the hills of the moiré superstructure, a high binding energy tail emerges and eventually dominates the spectrum in the 30 Å-thick molecular film. A similar trend can be observed in the core level evolution of MnPc molecules, with the spectrum of 0.2 ML MnPc/Gr/1 ML Co being heavily distorted, especially in the low binding energy region, in comparison with the MnPc 30 Å-thick film. Also in this case, when the molecules start to adsorb at higher distances from the intercalated Co layers, the spectrum progressively recovers the lineshape of free-standing-like MnPcs, suggesting a release of the electronic coupling moving away from the intercalated Co layer. The shift towards lower binding energies as well as the lineshape deformation is much more pronounced when FePc and MnPc are placed directly in contact with reactive magnetic surfaces [115, 134]. In particular, the N1*s* core level of FePc and MnPc, respectively interfaced with Co and Ni, exhibits a ∼1.0 eV shift of the core level centroid towards lower binding energies. Such a large shift cannot be justified in terms of charge screening effects, and it was attributed to strong molecule-substrate chemical interactions [115, 134].

By combining X-ray absorption and photoemission spectroscopy at the C and N sites of the organic macrocycle, we can deduce that the molecules adsorb intact and flat-lying on the Gr/Co support, without any strong interaction/deformation involving the common Pc ring. The organic cage of the TMPc molecules is immersed in a complex potential when placed in contact with the valleys of the Gr moiré superstructure, reflected in a distorted lineshape of the N1*s* core level. However, even if the Gr buffer layer is able to (partially) decouple the organic Pc rings from the reactive Co surface, other interaction channels may involve directly the transition metal ions [136]. To (separately) address this contribution, we now focus on the role of the metallic centers, to unravel how the different occupancy and symmetry of the *d*-related molecular orbitals are reflected in the molecule-substrate electronic interaction at the TMPc/Gr/Co interfaces, by a joint X-ray absorption and photoemission spectroscopy study.

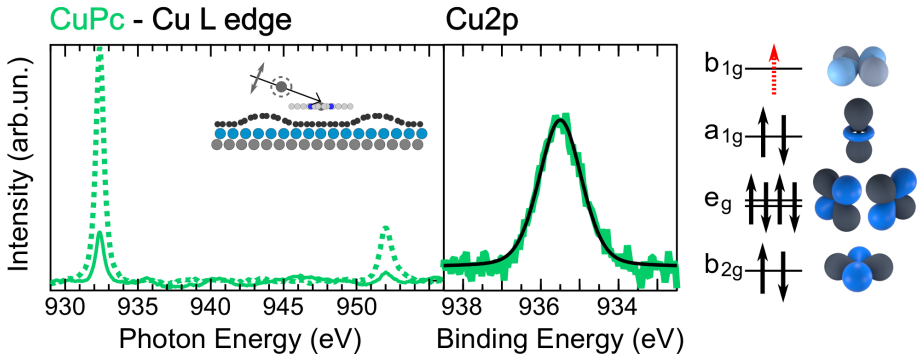

Figure 3.9: NEXAFS at the Cu $L_{2,3}$ edges (left) and XPS of the Cu2p core level (right) for 0.3 ML CuPc deposited on Gr/1 ML Co.

Starting from the electronic interaction at the Cu metal centre, we recall that its electronic structure is simple, as with its $3d^9$ configuration it has one single hole in the $d_{x^2-y^2}$ state (Fig. 3.1). Accordingly, the absorption spectrum (left panel of Fig. 3.9) is characterised by a single white line at 932.5 eV ($2p_{3/2} \rightarrow 3d$, L_3), and its replica at around 20 eV higher photon energy ($2p_{1/2} \rightarrow 3d$, L_2), in fair agreement with the literature on CuPc thick films [137, 138]. The Cu2p core-level can be also modelled with a single peak, without lineshape deformation at the interface with Gr/Co, but with a similar 0.5 eV blueshift as observed for the N1s core level [137, 138]. Since the shift towards higher binding energies is common to all the atomic species composing the molecule (C, N and Cu), we can confidently conclude that it can be attributed to electrostatic effects. The weak Cu-Co interaction can be understood by looking at the electronic configuration of the central Cu atom. In particular, the Cu^{2+} ion has no out-of-plane protruding states that can be affected by the presence of the intercalated reactive metal and, consequently, the decoupling role of the Gr sheet is effective for this molecular unit.

Turning to the Fe-Co electronic coupling, we remind that the (most agreed) ground state configuration of FePc is ^3E_g, with a $b_{2g}(d_{xy})^2$ $e_g(d_{xz,yz}/d_\pi)^3$ $a_{1g}(d_{z^2})^1$ $b_{1g}(d_{x^2-y^2})^0$ $3d$ occupation sequence. When FePc molecules are directly in contact with a reactive surface, like Ni(111), the absorption spectrum looses its fine structure, and the remaining features are shifted in energy, because of the rising of a new final state, with mixed Fe-Ni character, as suggested by J. Uihlein and co-workers [139]. The authors then interposed a Gr sheet between the FePc molecules and the Ni(111) surface, and, in this case, the spectral lineshape fully resembles that of an isolated molecule, confirming the efficient screening of the molecule-metal charge transfer/orbital intermixing processes [139].

To address the effect of the altered surface potential upon Co intercalation between

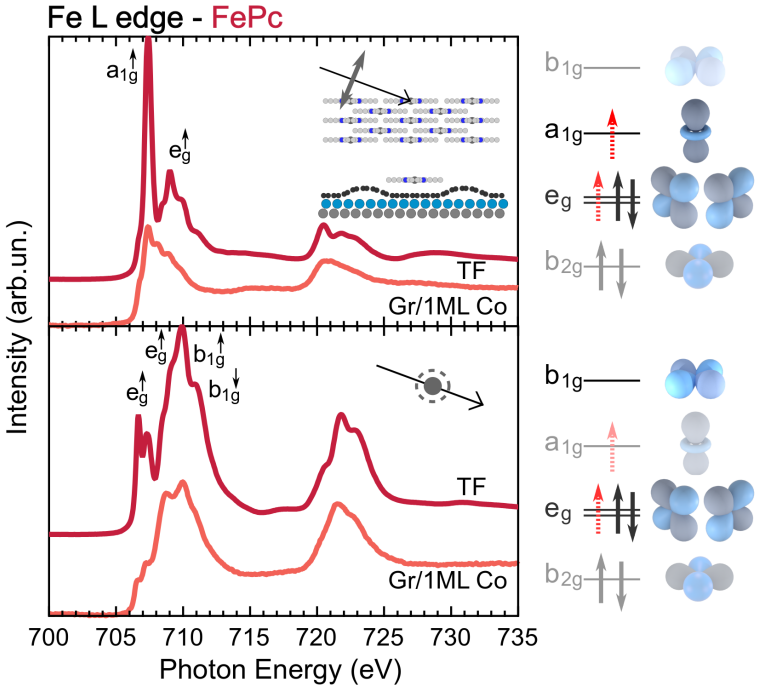

Figure 3.10: NEXAFS measurements at the Fe $L_{2,3}$ edge for FePc molecules at the interface with Gr/Co (orange curve) in comparison with that of a 30 Å-thick molecular film (red curve), acquired with vertically (top) and horizontally (bottom) polarized radiation. In the right panel a sketch of the molecular orbital is reported, with the one involved in the transitions being highlighted.

Gr and Ir, we performed NEXAFS measurements at the Fe $L_{2,3}$ edges for FePc in a thick molecular film and at the interface with Gr/Co, as reported in Fig. 3.10. In the top part of the figure, the out-of-plane polarized molecular orbitals are probed, dominated by a sharp line at 707.5 eV due to the $2p_{3/2} \rightarrow a_{1g}(d_z^2)$ transitions [140]. Upon adsorption on Gr/Co this feature is reduced, suggesting that a charge-transfer mechanism involving this out-of-plane protruding metal state occurs at the FePc-Gr/Co interface. The other prominent feature at 709.0 eV is generally attributed to transitions from the $2p_{3/2}$ core level to the degenerate $e_g(d_{xz,yz})$ metal-related molecular orbitals. This final state also has a projection perpendicular to the surface plane and participates to the Gr-mediated FePc-Co interaction, being reduced at the interface with Gr/Co, filled by the electron injection from the intercalated Co layer. The spectrum acquired with in-plane-polarized radiation presents an evident evolution involving the peak at 706.0 eV, attributed to $2p_{3/2} \rightarrow e_g(d_{xz,yz})$ transitions, towards an empty state with out-of-plane character, experiencing a charge transfer from the extended states of the Gr/Co substrate [74].

To shed more light on the charge transfer mechanism, X-ray photoemission measurements were performed at the Fe2p core level for increasing molecular coverage. The Fe2p

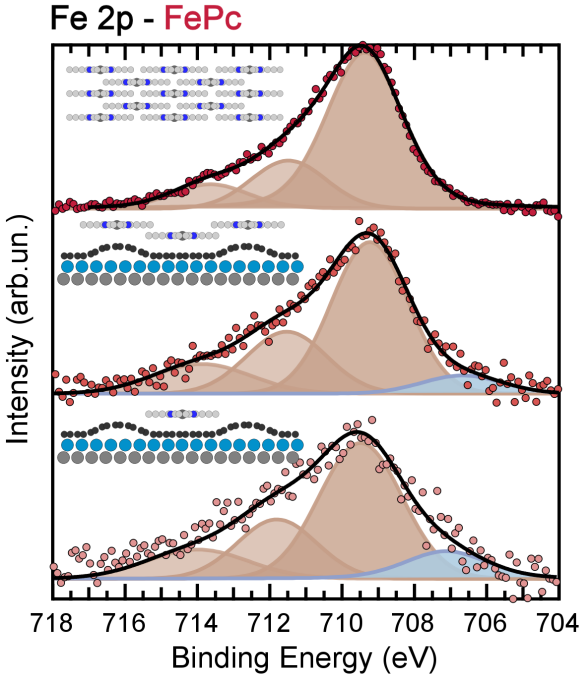

Figure 3.11: Fe2p core-level photoemission measurements for FePc trapped in the valleys (bottom) and covering the hills (center) of the Gr/Co substrate, compared with the signal of a 30 Å-thick molecular film (top), as sketched in the figure.

XPS spectra of less (bottom) and more (centre) than a single FePc layer adsorbed on the highly corrugated Gr/1 ML Co substrate are reported in Fig. 3.11, together with the signal measured for a thick FePc film. The Fe2p core level presents a broad and asymmetric lineshape, associated with a multiplet structure due to the interaction of unpaired electrons in the photoemission final states of the Fe^{2+} ion. We modelled the spectrum taking into account the partially-resolved fourfold Zeeman split $m_J = -\frac{3}{2}, -\frac{1}{2}, \frac{1}{2}, \frac{3}{2}$ with two 2.5 eV-wide Gaussian peaks located at 709.4 eV and 711.5 eV, plus a broader satellite feature located at higher binding energies (713.4 eV) [116, 141]. This approach very well reproduces the XPS spectrum of the thick FePc film, but a fourth peak, accounting for 12% of the total area, is needed to take into account the extra spectral weight in the low binding energy side of the spectrum when FePc molecules are at the interface with Gr/Co. The broadening towards lower binding energies has been observed for TMPcs adsorbed directly on metal surfaces, and it is a fingerprint of charge transfer from the substrate to the molecular adlayer, altering the oxidation state of the Fe ions [47, 116, 126, 142]. This component is reduced at increasing FePc coverage, indicating that the weak charge transfer mechanism is confined at the interface.

Finally, given its open d^5 shell and its complex multiplet configuration, the Mn^{2+}

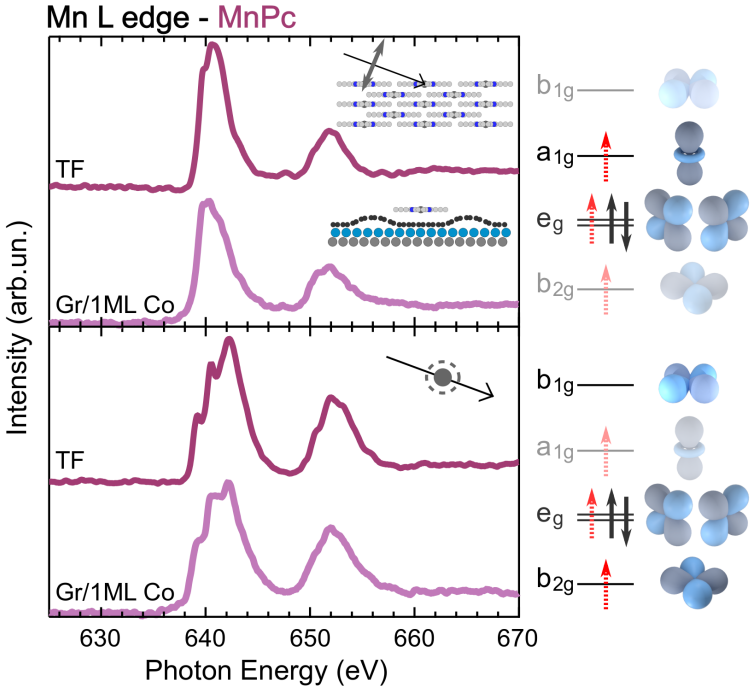

Figure 3.12: NEXAFS measurements at the Mn $L_{2,3}$ absorption edge, acquired with out-of-plane (top) and in-plane (bottom) polarized light, for MnPc at the interface with Gr/Co and in a 50 Å-thick molecular film, as sketched in the figure.

central ion may open several interaction channels with the Co layer, even through the Gr spacer. NEXAFS spectra at the Mn $L_{2,3}$ absorption edge for a thick MnPc film reflect the ^4E_g ground state of the Mn ion, with a $b_{2g}(d_{xy})^1\ e_g(d_{xz,yz}/d_\pi)^3\ a_{1g}(d_{z^2})^1\ b_{1g}(d_{x^2-y^2})^0$ configuration [47,137]. This means that, in its ground state, MnPc has final empty states both lying inside and protruding from the molecular plane and hence does not exhibit a definite dichroic response to vertically- and horizontally-polarized radiation [47]. It is worth noting that, contrary to all the other TMPc molecules, MnPcs adsorbed on surfaces are expected to relax to a D_{2h} symmetry in a Jahn-Teller manner [143], and the Mn-N_{pyr} bonds across the x- and y-axes may be no longer equivalent and, therefore, the $d_{xz} - d_{yz}$ degeneration should be lifted [144], making this molecular interface even more complex.

If no decoupling layer separates MnPcs from the ferromagnetic support, a chemical reaction occurs at the interface and the molecules fragment, as suggested by J. Uihlein and colleagues for MnPc on Ni(111). The Mn $L_{2,3}$ absorption spectrum is strongly altered compared to the thick molecular film, as reported in Ref. [115].

In Fig. 3.12 we report the spectrum of a 50 Å-thick MnPc film (dark curves), acquired with out-of-plane (top) and in-plane (bottom) electric field polarizations. The spectrum consists of two energy regions: the L_3 (638-647 eV) and L_2 (649-657 eV) absorption peaks

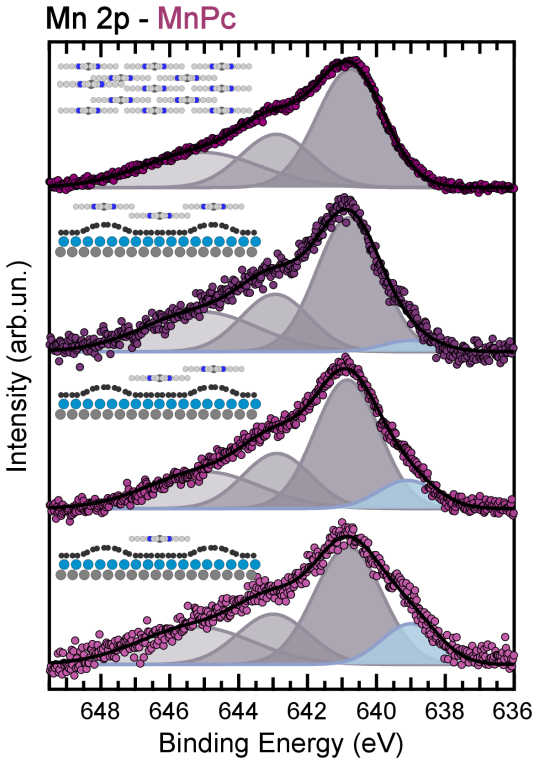

Figure 3.13: Mn2p core-level photoemission measurements for MnPc/Gr/Co at increasing molecular coverage from bottom to top, as sketched in the figure.

respectively attributed to transitions from the $2p_{3/2}$ and $2p_{1/2}$ core level to the empty $3d$ states mainly located on the central Mn ion. The L_3 peak, excited by photons with in-plane polarization, is constituted by three distinct features at 639.2 eV, 640.5 eV and 642.2 eV, while the out-of-plane response is less structured and characterized by two broad contributions at around 639.8 eV and 640.7 eV. A one-to-one correspondence between the absorption peaks and final empty molecular orbitals is prevented by the considerable multiplet/correlation effects of the open d^5 shell. The in-plane polarized molecular orbitals (bottom panel of Fig. 3.12) are not altered upon adsorption on the highly corrugated Gr-Co heterostructure, except for a slight overall reduction of the absorption signal, indicating an efficient decoupling role played by the Gr sheet. On the other hand, the out-of-plane molecular orbitals exhibit a more marked evolution at the interface with Gr-Co, with the feature at 640.5 eV being depleted. This can be attributed to charge injection in the molecular orbitals/multiplet configurations contributing to the reduced absorption peak. However, no shift of the pre-existent feature/rising of new ones is observed, suggesting a preservation of the ground state configuration upon adsorption, as found for MnPcs adsorbed on other inert substrate, e.g., graphite [145].

The Mn2p core level at increasing density of MnPc on Gr/Co and for a 30 Å-thick molecular film are reported in Fig. 3.13. The Mn2$p_{3/2}$ core level, similarly to what observed for Fe2p, presents a broad asymmetric lineshape, also fitted in a partially-resolved Zeeman splitting approach. Following the same procedure described for FePc/Gr/Co, this model reproduces the XPS spectrum of the thick molecular film, but again it is not able to reproduce the signal increase at the low binding energy region for mono- and sub-monolayers. Similarly to FePc at the interface with rippled Gr/Co, a fourth component needs to be added when MnPc are at the interface with Gr/Co, with an intensity equal to 13% of the total spectral area. A similar Fe- and Mn-Co interaction mechanisms suggests that the opening of TMPc-Co charge transfer channel is activated by the out-of-plane protruding molecular orbitals with a dominant 3d character, and is similar for the two molecular units.

The role of the central transition metal ion is crucial in the molecule-substrate electronic interaction as mediated by the moiré superstructure of Gr/Co. If no metal states with out-of-plane symmetry are available, as in the case of CuPc, screening/polarization effects dominate the coupling while, for less filled 3d shells, e.g., Fe and Mn, a weak charge transfer from the Co layer to the out-of-plane protruding metal states is observed. In particular, the interaction between TMPc molecules and the intercalated Co layer comes out to be different within the rippled superstructure. At the early deposition stage, *i.e.*, when the molecules are trapped in the valleys, a hybridization of TM-related out-of-plane orbitals with the underlying Co is only partially screened by the presence of the Gr buffer layer. At higher molecular densities, *i.e.*, when the molecules sit at higher distances from the reactive Co, this hybridization is released and TMPcs are fully decoupled.

3.2.1 The role of graphene corrugation

The structural/magnetic configuration of the Gr/Co support can be tuned by increasing the thickness of the intercalated Co film, as detailed in Chap.2. In particular, when more that 4 ML Co are intercalated beneath the Gr sheet, the Gr-Co lattice mismatch is reduced and the Gr sheet lies, within the resolution limits of our LEED, commensurate and flat on the thicker Co film. Theoretical simulations of flat commensurate Gr/Co predict an increased C-Co distance of about 2.05 Å (to be compared with a minimum of 1.90 Å for Gr/1 ML Co), hence we expect that the TM-Co interaction through the Gr spacer is weakened/released when TMPcs are adsorbed on this substrate, sitting at higher distances

from the Co film. In this section we will address how the different electronic and structural environment affects the interaction between adsorbed TMPcs and the intercalated Co film.

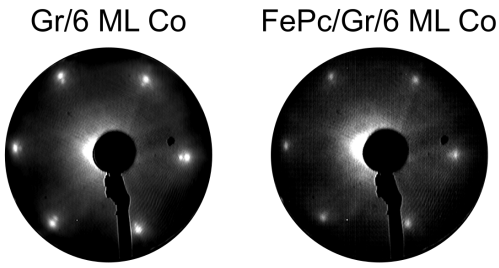

Figure 3.14: LEED pattern of Gr/6 ML Co before (left) and after FePc deposition acquired with a primary beam energy of 140 eV.

In Fig. 3.14 we report the LEED pattern acquired for pristine Gr/6 ML Co and after FePc deposition. It is evident that molecular adsorption does not alter the long-range periodicity of the Gr-Co commensurate substrate, as was observed for the highly corrugated Gr/1 ML Co substrate.

NEXAFS measurements performed at the N K absorption edge can unveil the TMPc adsorption geometry when the rippling of the Gr sheet is released. In Fig. 3.15 we present the absorption spectra acquired at the N K-edge for CuPc, FePc and MnPc molecules interfaced with flat commensurate Gr/Co (left) and in a thick molecular film (right). The NEXAFS spectra reveal that also in this case the molecular building blocks adsorb mostly flat-lying with the molecular plane parallel to the sample surface. The spectral lineshape does not exhibit any substantial evolution at decreasing Gr corrugation for CuPc and FePc molecules, fairly retaining the features of weakly interacting TMPc molecules in a thick film, as also observed for the similar FePc/Gr/Ni(111) system [139]. For MnPc, the intensity ratio of the first doublet is altered at the interface with Gr/7 ML Co pinpointing to a different degree of participation of *aza-bridging* and *pyrrolic* N atoms in mediating the Mn-Co coupling, as also suggested by J. Uihlein and co-workers for MnPc adsorbed on the flat commensurate Gr/Ni(111) in Ref. [115].

To further enlighten the role of the organic macrocycle in mediating the electronic coupling between the molecular adlayer and the intercalated thicker Co film, we present the C and N1*s* core level spectra for TMPcs on Gr/4-6 ML Co respectively in the left and right panels of Fig. 3.16. We want to emphasize that the differences in the Gr-related peak for this substrate are due to the different Co thickness, lower for MnPc and higher for CuPc, as discussed in the previous chapter. If we compare the fitting parameters

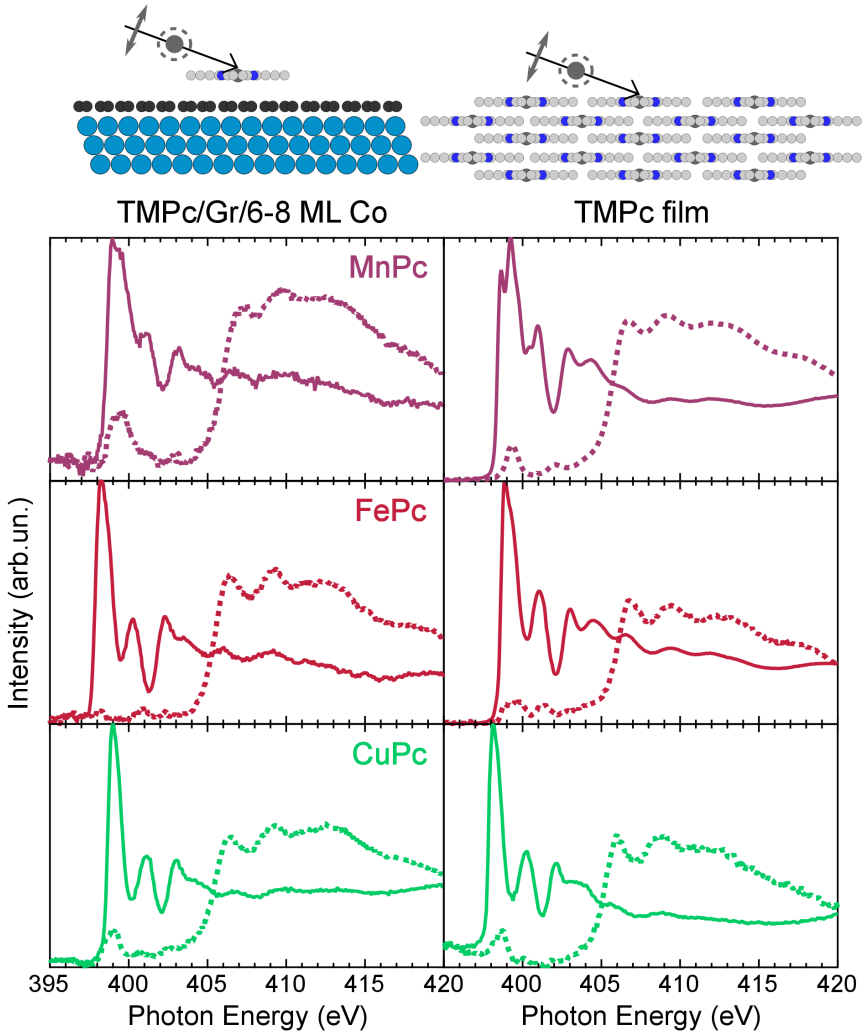

Figure 3.15: NEXAFS measurements at the N K-edge for TMPcs, TM= Mn (top), Fe (center), Cu (bottom) deposited on Gr/6-8 ML Co (left), compared with a thick molecular film (right). Experimental geometry in the top part of the figure.

Peak	**BE (eV)** (±0.1 eV)	**FWHM (eV)** (±0.1 eV)	**Intensity %**
	MnPc		
C_B	284.3 (284.5)	0.7	1.00
C_P	285.6 (285.8)	0.7	0.35
	FePc		
C_B	284.4 (284.4)	0.6	1.00
C_P	285.8 (285.8)	0.7	0.36 (0.30)
	CuPc		
C_B	284.4 (284.6)	1.0	1.00
C_P	285.9 (286.0)	1.0	0.29

Table 3.2: Fitting parameters of the pseudo-Voigt components used to model the molecular contribution to the C1s core level of 0.3 ML MnPc (top), 0.5 ML FePc (center) and 0.8 ML CuPc (bottom) deposited on Gr/4-6 ML Co. Data reported in Fig. 3.16.

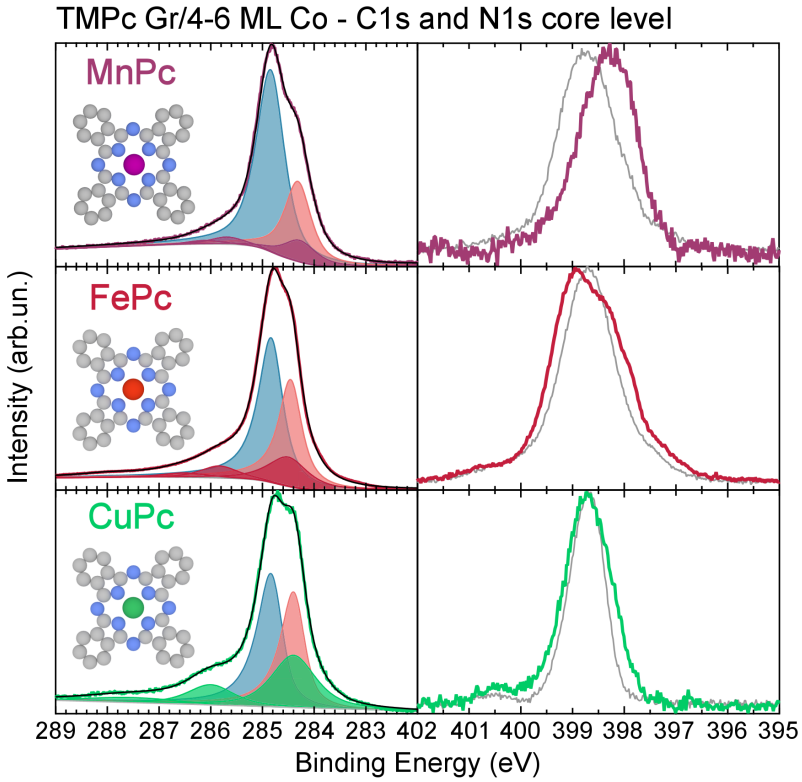

Figure 3.16: C (left) and N (right) 1*s* core levels for 0.3 ML MnPc (top), 0.5 ML FePc (center) and 0.8 ML CuPc (bottom) adsorbed on Gr/4-6 ML Co.

reported in Tab.3.2 with the ones in Tab.3.1, respectively, modelling the C1*s* core level of TMPcs on Gr/4-6 ML and 1 ML Co, and with what is reported in the literature for thick molecular films (from Ref. [115, 116, 146], in parenthesis), we can confirm that the FePc- and CuPc-Co coupling is reduced in this configuration. On the other hand, the C1*s* core level of MnPc molecules does not evidence any evolution when the substrate corrugation is removed and the TMPc-Co distance increased, since the peak positions remain compatible with what was measured at the interface with the rippled Gr/Co moiré and still do not recovery the bulk-like values. This suggests that the contribution of the organic macrocycle in the electronic interaction is significant for MnPc, because of stronger ligand-metal hybdridization for less filled 3*d* shells [143].

When our molecular building blocks are deposited on flat commensurate Gr/6-8 ML Co, an overall broadening of the N1*s* core level is observed. Besides, the centroid is located at the same binding energy as the thick molecular film for FePc and CuPc, indicating no significant N-mediated molecule-substrate charge transfer/orbital intermixing in this configuration. Regarding MnPcs, the spectral lineshape is again shifted towards lower binding energy, suggesting an involvement of the N atoms in the electronic interaction with

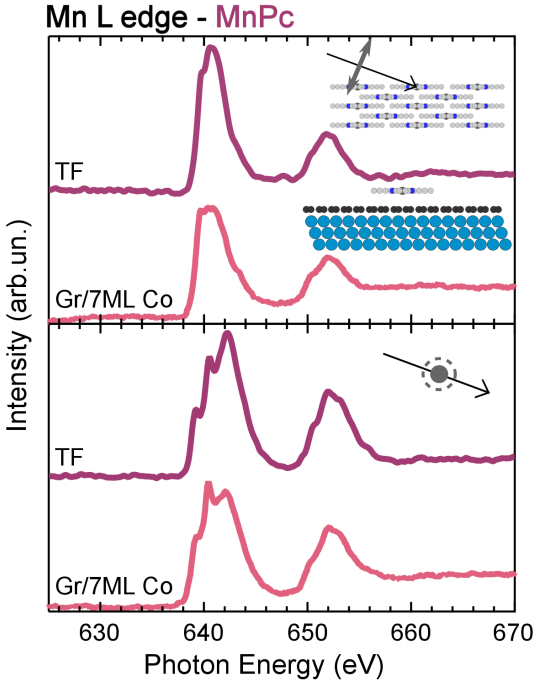

Figure 3.17: NEXAFS measurements at the Mn $L_{2,3}$ absorption edge, acquired with out-of-plane (top) and in-plane (bottom) polarized light, for MnPc at the interface with Gr/Co and in a thick molecular film, as sketched in the figure.

the Gr-Co substrate, in agreement with what is observed by absorption spectroscopy and with recent literature on the similar MnPc/Gr/Ni(111)system [115]. However, the spectral lineshape recovers its symmetry in all the samples, pinpointing to a unique configuration, in which the organic macrocycle is fully decoupled for FePc and CuPc, while it slightly contributes to a Mn-Co interaction channel, weakened by the release of the Gr rippling and by the increased MnPc-Co distance.

Turning to the metal-related molecular orbitals, we notice that the out-of-plane spectrum of MnPc (top panel of Fig. 3.17) fairly recovers the bulk-like lineshape, suggesting that the interaction channel responsible for the Mn-Co electronic coupling described in the previous section is absent. On the other hand, the intensity ratio between the in-plane features is altered, with the peaks at 639.2 eV and 642.2 eV being reduced. This spectrum fairly reproduces that of MnPc adsorbed on the similarly flat commensurate Gr/Ni(111) substrate [115], for which the opening of a new N-mediated Mn-Co charge transfer channel was proposed, and agrees with the slight redshift observed for the C and N 1s core levels.

The effect of the released corrugation is evident also for FePc. Indeed, the metal states both protruding out and lying inside the molecular plane have recovered their intensity, as deduced by the NEXAFS spectra at the Fe $L_{2,3}$ edges in the left panel of Fig. 3.18.

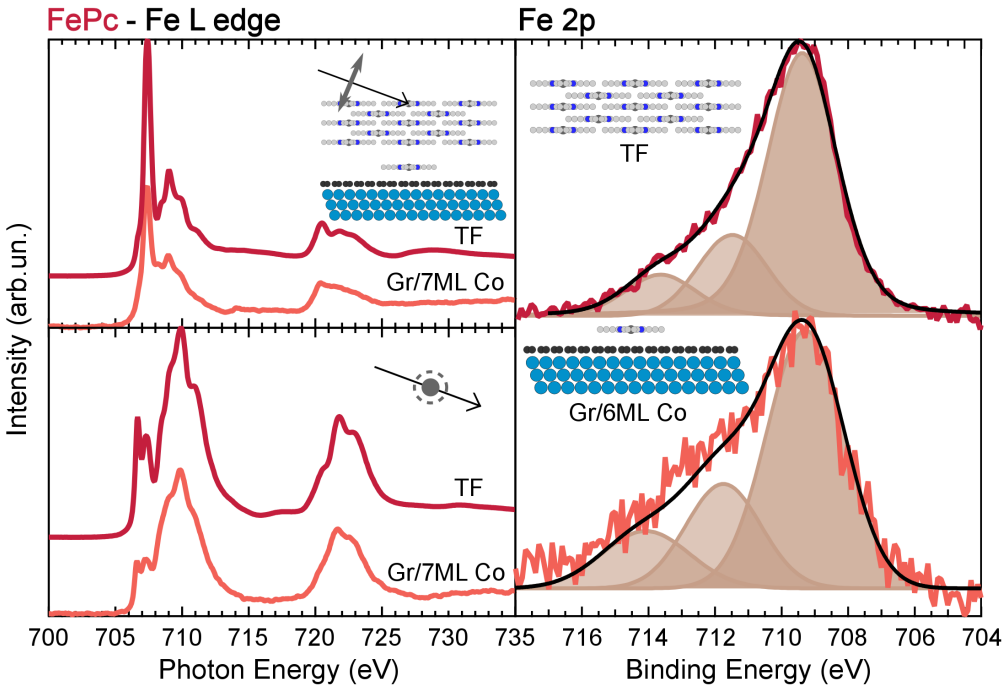

Figure 3.18: NEXAFS measurements at the Fe $L_{2,3}$ absorption edge, acquired with out-of-plane (top) and in-plane (bottom) polarized light, for FePc at the interface with Gr/Co and in a thick molecular film, as sketched in the figure.

This suggests that no charge transfer/orbital intermixing process occurs for FePc at the interface with flat commensurate Gr/Co. This is also confirmed by XPS measurements at the Fe2*p* core level, reported in the right panel of Fig. 3.18 for FePc in a thick molecular film and in contact with the Gr/Co substrate. By comparing the two spectra we notice that no extra signal in the low binding energy side of the core level can be detected, corroborating the release of the Fe-Co electronic interaction when FePc molecules are adsorbed on a flat Gr sheet and sitting at higher distance from the intercalated Co film.

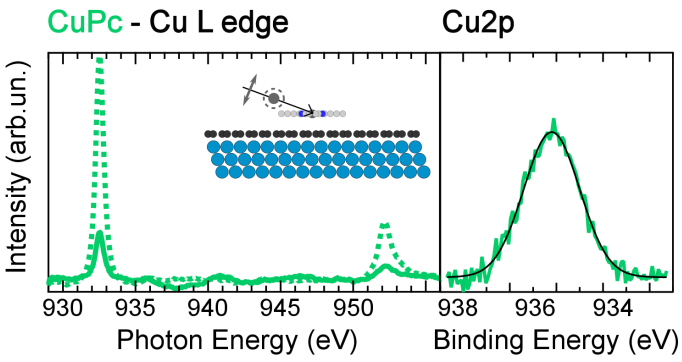

Figure 3.19: NEXAFS at the Cu $L_{2,3}$ edges (left) and XPS of the Cu2*p* core level (right) for 0.8 ML CuPc deposited on Gr/6 ML Co.

Finally, in Fig. 3.19 we report the X-ray absorption (left) and photoemission (right) spectra acquired at the Cu sites for CuPc on flat commensurate Gr/Co. Both measurements reveal a lineshape fully resembling that of CuPc thick films, indicating that the Cu 2^+ ion is not affected by the presence of the reactive Co surface beneath the Gr sheet. It is worth highlighting that, in this configuration, the position of the centroid has recovered the bulk-like value. This suggests that the rigid 0.5 eV blueshift observed for the XPS spectra of CuPc/Gr/1 ML Co, can be ascribed to electrostatic effects probably due to the surface polarization field, rising because of the enhanced Gr corrugation.

3.3 Conclusions

In this chapter we characterized the structural arrangement and the electronic interaction channels at the TMPc/Gr/1 ML Co interfaces, preparatory to the investigation of the TMPc-Co magnetic coupling. In particular, we have proved that the highly corrugated Gr-Co substrate, with a strongly site-dependent surface potential modulation, provides inequivalent adsorption sites driving the self-assembly of well-ordered Kagome lattices made up by equally sized and evenly spaced molecular spin units. The graphene-induced decoupling is complete in the case of CuPc, while an interaction channel involving the out-of-plane molecular orbitals located on the central metal ion remains open for MnPc and FePc. In particular, at the early deposition stages we observed an intermixing between the Co layer and the Mn(Fe) ions out-of-plane orbitals, inducing an extra component in the Mn(Fe) core levels and a re-distribution of the Mn(Fe) empty states. At higher molecular coverage, when TMPcs start to occupy the top sites of the moiré superstructure, the TM-Co interaction is reduced. Finally, we have investigated the role of Gr corrugation in the charge transfer channel involving the out-of-plane protruding molecular orbitals. We found that, when a thick Co film is intercalated, the substrate corrugation is released and the molecule-substrate distance is increased. As a result, the adsorbed TMPcs are almost fully decoupled by the Co film, without any evidences of orbital filling/intermixing both for the organic cage and for the magnetic centers.

Chapter 4

Graphene-mediated magnetic coupling

Molecular spin interfaces are emerging as key enablers for exploring magnetic interactions in spintronic applications, but it is crucial to achieve a well-ordered molecular network with unaltered magnetic state upon adsorption and robust magnetic remanence, up to device working temperature. The deep understanding of the fundamental coupling mechanisms between metal-organic molecules and magnetic surfaces can allow to fully control the electronic and magnetic functionalities of the hybrid spin architectures. In this chapter we present element-sensitive XMCD experiments performed for FePc, CuPc and MnPc on Gr/Co, unravelling a sizable TM-Co magnetic coupling, with tunable sign and strength depending on the occupancy and symmetry of the magnetically active molecular orbitals. Theoretical calculations reproduced the experimental results and unveiled super-exchange pathways selected by the molecular orbital located on the central transition metal ion. In particular, 180° and 90° super-exchange mechanisms, respectively leading to strong antiferromagnetic and weak ferromagnetic coupling, were identified. Temperature-dependent XMCD measurements revealed the robustness of the magnetic response against thermal fluctuations, with exchange energies depending on the symmetry of the spin polarized molecular orbitals and on the relative orientation between the molecule and substrate easy magnetization directions.

The magnetic properties of TMPcs can be dramatically altered by chemical modification of the molecule [147,148] and/or upon adsorption on a metallic substrate due to orbital intermixing with the surface extended states and molecular symmetry reduction [149], as well as chemisorption-induced bond length variations [150]. The absence of charge transfer, both intramolecular between ligand and metal ion and with the surface, can preserve the magnetic properties of the metal-organic paramagnets, saving the magnetic moment of the molecule-metal substrate complex, as well as guaranteeing charge and spin injection across the molecule-metal interface [26, 48, 151]. When TMPc (or the similar metal porphyrine) molecules are directly deposited on a magnetic surface, they always couple ferromagnetically with the underlying ferromagnet due to a (in)direct exchange interaction [33,150,152]. The picture gets more complicated when a paramagnetic buffer layer (e.g. oxygen, Gr...) is interposed between the magnetic substrate and the adsorbed metal-organic molecules, changing the structural environment, screening the electronic interaction and eventually opening more complex super-exchange paths [41, 44, 46, 76, 112, 153–155].

Molecular spin interfaces in which the electronic-magnetic configuration of the spin units is preserved, thanks to the presence of the Gr buffer layer, and, concurrently, stabilized against thermal fluctuations are attracting the attention of the scientific community. In this chapter we present a systematic investigation of the key parameters involved in the coupling mechanism, to enlighten the fundamental forces driving the process.

4.1 Super-exchange pathways

4.1.1 FePc/Gr/Co: a 180° super-exchange interaction

The XMCD spectrum of FePc acquired at the Fe $L_{2,3}$ edge at T=3 K and in a NI experimental geometry, hence probing the molecular orbitals lying parallel to the surface plane, is presented in Fig. 4.1 (left), together with the element-selective Fe (red) and Co (blue) hysteresis loops acquired in the same conditions (right). From the experimental data reported in Fig. 4.1, the strong Fe-Co AFM coupling is unambiguous, given the antiparallel alignment between Fe and Co magnetizations. In this experimental geometry the most probable transitions are, as detailed in Sec.3.2, from the Fe $2p_{3/2}(2p_{1/2})$ to the projection of the e_g orbital in the molecular plane, at around 706–708 eV, but the strongest contribution arises from transitions to the empty b_{1g} molecular orbital, excited with a photon energy of around 710 eV (L_3) and 722 eV (L_2) [58, 140]. The adsorbate spin state cannot

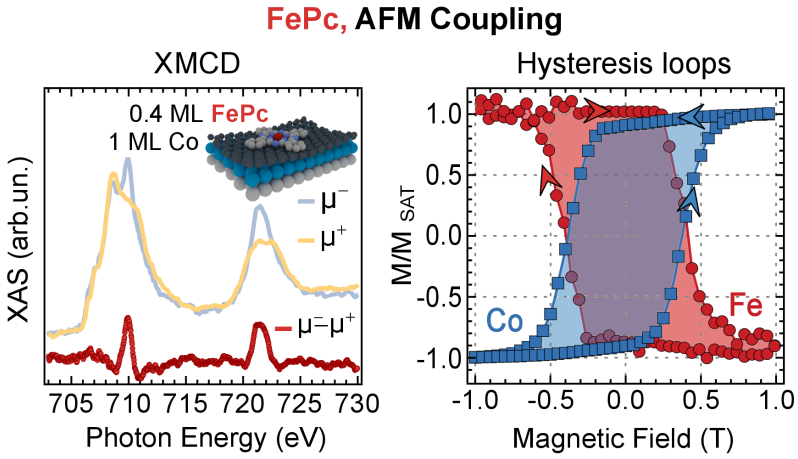

Figure 4.1: Remanent X-ray Absorption Spectroscopy (XAS) and XMCD spectra (left) and element-selective hysteresis loops for 0.4 ML FePc on Gr/1 ML Co/Ir(111), highlighting the strong Antiferromagnetic (AFM) coupling. The measurements were performed at NI,*i.e.*, along the easy magnetization axis of the molecule-metal complex, at T=2 K.

be univocally determined by applying the orbital and effective spin sum rule to the XMCD spectra in Fig. 4.1 because of (i) final state effects and partial overlap between the L_2 and L_3 absorption edges; (ii) strong magnetic coupling, inhibiting the magnetic saturation of the Fe ions, (iii) errors induced by the background subtraction procedures, due to the very dilute nature of the magnetic species [156]. However, the XAS and XMCD lineshape agrees well with the one reported for a thick FePc film [140], with only slightly altered intensity. Accordingly, we can conclude that the electronic interaction with the Gr/Co substrate plays a minor role and does not alter the spin and orbital configuration of the adsorbed FePc molecule, also confirmed by theoretical calculations, see Tab.4.1.

The magnetic properties of the adsorbed TMPc molecules are preserved thanks to the presence of the Gr buffer layer, and no hybrid Fe-Co state is formed. However, it can be noticed from the hysteresis loops in Fig. 4.1 that the magnetic moment of the metal-organic adsorbate fully mimics the magnetization of the substrate, in every configuration and at any field, taking on its easy magnetization direction and coercivity. This means that they form a single magnetic unit, and it is not possible to control the molecule and substrate magnetizations independently [33].

Theoretical calculations[1], performed using the Quantum ESPRESSO package with the PBE+U (U= 4 eV [144, 157]) method and taking into account for the first time the full (9×9 Ir and 10×10 C) moiré cell *plus* an adsorbed FePc molecule, confirm the

[1]Courtesy of Dr. Claudia Cardoso, Dr. Daniele Varsano and Dr. Andrea Ferretti.

	TM	N mol	C mol	C Gr	Co
FePc	-2.10 (2.20)	0.20 (-0.03)	0.22 (-0.19)	-0.42	120.58
CuPc	+0.54	0.48	0.06	-0.42	120.61

Table 4.1: The spin polarization, as given by Lödwin charge analysis, is reported for each atomic species in a full moiré cell, *i.e.*, for 1 TM atom, 8 N atom, 32 C mol atoms, 200 C Gr atoms, and 81 Co atoms, and in an isolated FePc molecule (in parenthesis).

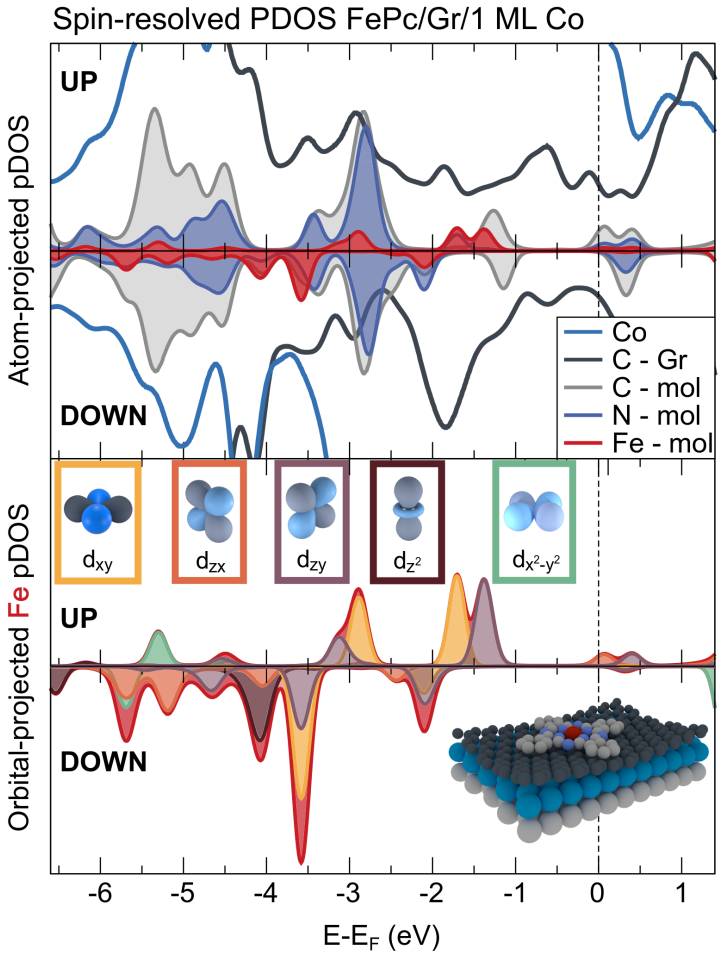

Figure 4.2: The theoretically calculated spin-resolved density of states is reported as projected on the different atomic species (top) for a single FePc molecule on Gr/1 ML Co/Ir(111). The pDOS of the central Fe ion is then decomposed in spherical harmonics and projected on the *d* orbitals (bottom).

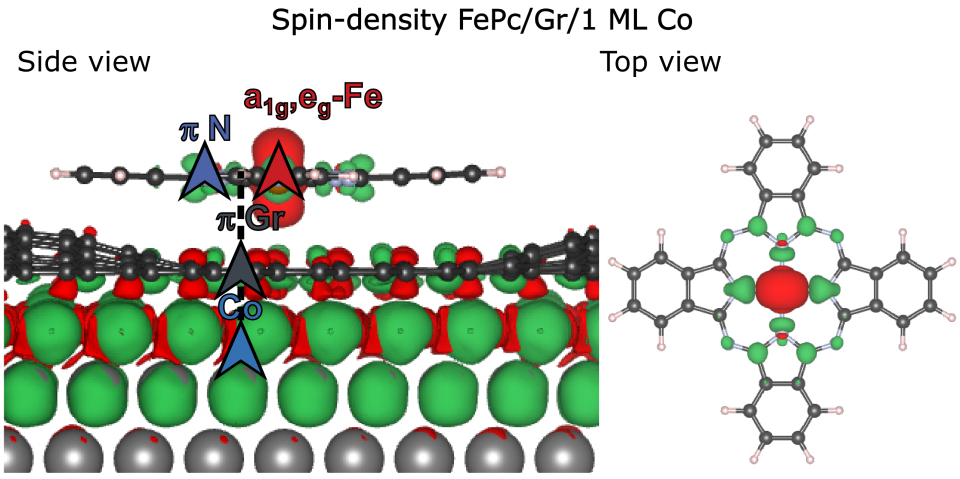

Figure 4.3: Theoretically calculated spin density distribution plots of FePc adsorbed on Gr/Co from the side (left) and top (right) views. The proposed 180° super-exchange path is highlighted.

interpretation of the experimental data reported above. In the top panel of Fig. 4.2 the atom- and spin-projected partial density of states (pDOS) is reported, revealing an induced magnetization in the C and N atoms of the FePc molecules, as well as on the central Fe atom, aligned antiparallel to each other (*i.e.*, Gr↓, N↑, Fe ↓, as sketched in Fig.4.3). Löwdin charge analysis was used to quantify the net magnetic moments induced on the atomic species involved in the magnetic coupling and the results are summarized in Tab.4.1, together with the values obtained for an isolated FePc molecule. It can be noticed that the magnetization on the central Fe ion is not altered upon adsorption on the rippled Gr/Co surface, while that located on the N atoms of the organic macrocycle is strongly enhanced, confirming their role in transmitting the magnetic information, actively mediating the magnetic coupling. The contribution of the d orbitals with different symmetry can be separated by projecting the Fe pDOS onto spherical harmonics, as presented in the bottom panel of Fig. 4.2. The magnetization of the Fe centers is carried by either two or three orbitals (depending on the specific exchange functional), the a_{1g} (d_{z^2}) state and either one or both the e_g ($d_{xz,yz}, d_\pi$) orbitals, suggesting that the driving forces of the magnetic coupling reside in the out-of-plane symmetric molecular orbitals. The path through which the magnetic polarization is transmitted is pictured in Fig. 4.3, by theoretically-calculated spin up (down) density isosurfaces in green (red). The π orbitals of Gr carry a small negative magnetic moment due to the hybridization with the spin-polarized Co states. This induces a positive magnetization in the π orbital of the N *aza* atoms and over the C and N atoms in the pyrrol rings, closer to the Fe^{2+} ion centre. Finally, a net negative spin

polarization is found at the Fe sites, with the isosurface resembling the shape of the d_{z^2} and of the d_π orbitals. Indeed, these detailed theoretical simulations fully support a 180° super-exchange coupling scheme, involving the π orbitals of the Gr sheet as well as of the molecule organic ligand, antiferromagnetically coupled to the central TM ion [76,154,158].

Macroscopic magnetism generally emerges from short-ranged interactions between adjacent units. To achieve magnetic interactions over a large distance, a super-exchange mechanism can be invoked, where the bridging over non-magnetic organic ligands mediates higher-order virtual hopping processes. In TMPc/Gr/Co spin interfaces, both the Gr layer and the molecules organic ligands can mediate the coupling between the central transition metal ions and the magnetic Co film. DFT finds that TMPc molecules on Gr/Co sit at an average TM-Co distance of 5.25 Å (see Sec.3.1 for details), independent on the nature of the transition metal core. This means that direct exchange interactions, requiring a non-vanishing overlap between the Fe(Cu, Mn) and Co wave-functions, can be excluded. Other possible interaction channels at such high distances could be (i) a direct coupling with the Co-induced magnetic polarization of the Gr layer and/or (ii) magnetic dipole-dipole interactions.

The first mechanism can be excluded because, given the small Gr magnetic moment and

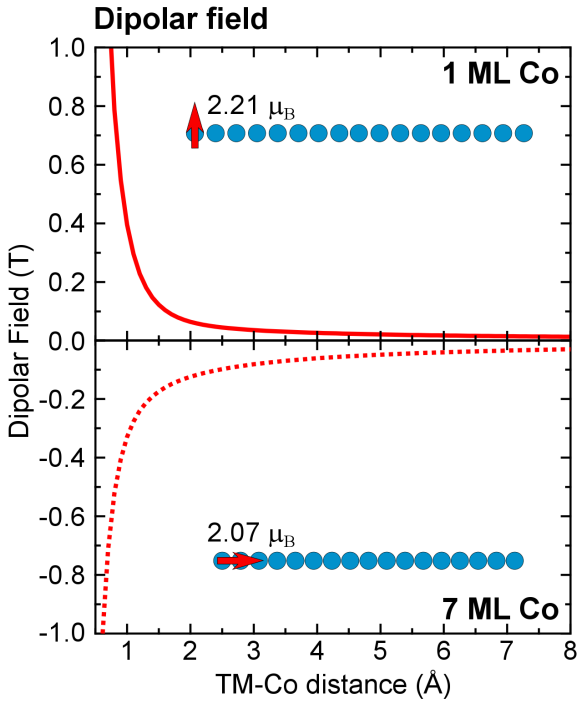

Figure 4.4: Dipolar field calculated for 2000×2000 point-like dipoles, with moment 2.3 μ_B (2.07 μ_B) and arranged pseudomorphic to the Ir(111)(Gr) lattice, as reported in the top(bottom) panel as a function of the distance z.

the fairly large Gr-Fe distance (3.25 Å), it cannot be the dominant mechanism driving such a strong AFM alignment, resistant against a 6 T magnetic field. We want to emphasize that, when the nanomagnet has reduced lateral coordination (e.g. single atoms/small clusters of Co on Gr/Ni(111) [41]) they considerably hybridize with the Gr layer and lie closer to it (C-Co distance$\sim$ 2Å). Accordingly, the Co-Ni magnetic coupling is mainly due to direct exchange interaction between the single Co atoms spin and the Ni-induced spin polarization of the Gr π states. Finally, when separating 3D magnets, Gr efficiently acts as a barrier for spin currents, allowing for perpendicular spin transport only via tunnelling [159–161].

In order to estimate an ensemble of the contribution from the dipolar field generated by the intercalated Co layer(s), we modeled this system as point-like dipoles with a magnetic moment of 2.21 μ_B (2.07 μ_B) for 1 ML (7 ML) Co (as deduced in Tab.2.2, in Chapter 2), arranged pseudomorphic to the Ir(111) (graphene) surface. The resulting dipolar field is then calculated as:

$$\vec{B}_{dip} = \frac{\mu_0}{4\pi} \sum_i 3\frac{(\vec{\mu}\cdot\vec{r}_i)\vec{r}_i}{r_i^5} - \frac{\vec{\mu}}{r_i^3} \tag{4.1.1}$$

The results are depicted in Fig. 4.4 and, at the DFT-calculated TM-Co distance, the dipolar field is less than 0.05 T for both configurations. In light of this, a super-exchange interaction is the most probable coupling mechanism. These findings are in agreement with recent literature on both planar [44] and non-planar [42] molecules adsorbed on a Gr/ferromagnet support.

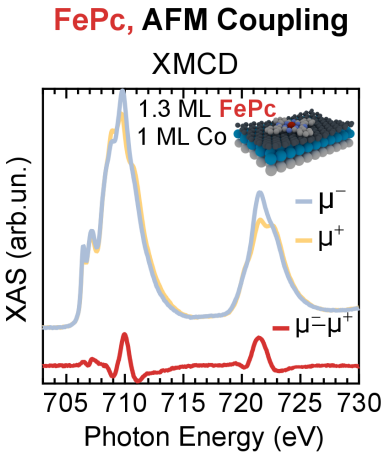

Figure 4.5: XAS and XMCD measurements performed at the Fe $L_{2,3}$ absorption edge for 1.3 ML FePc deposited on Gr/1 ML Co/Ir(111). The spectra were acquired at a temperature of 3 K, in remanence conditions and in a NI experimental geometry.

In Fig. 4.5 we report the XMCD measurements at the Fe $L_{2,3}$ absorption edge acquired for 1.3 ML FePc/Gr/1 ML Co, hence when the second molecular layer is developing. It

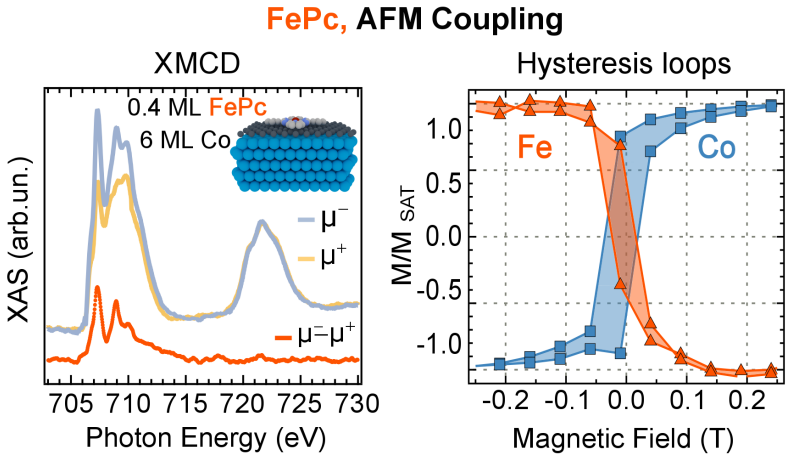

Figure 4.6: Remanent XAS and XMCD spectra (left) and element-selective hysteresis loops for 0.4 ML FePc on Gr/6 ML Co/Ir(111), highlighting the strong AFM coupling. The measurements were performed at GI, *i.e.*, along the easy magnetization direction of the molecule-metal complex, at T=2 K.

can be noticed that the AFM Fe-Co alignment is preserved, but with slightly reduced dichroism. This could be attributed to a less-efficient action of the super-exchange interaction mechanism, as well as to a Ferromagnetic (FM) coupling between FePcs in the first and in the second layer.

In the configuration reported above, the stability and strength of the Fe-Co magnetic coupling is affected by the perpendicular orientation of the molecule-substrate easy magnetization directions, as the FePc molecule is intrinsically easy-plane while the Gr/1 ML Co substrate has an out-of-plane easy-axis magnetic anisotropy. In order to overcome this issue, a second experiment was performed investigating the magnetic response of FePc molecules adsorbed on Gr/6 ML Co, *i.e.*, in the configuration where both the molecule and the substrate exhibit an easy-plane magnetic anisotropy. The XAS spectra acquired with positive and negative helicities and the corresponding XMCD difference spectrum are reported in Fig. 4.6 acquired at low temperature and in a GI experimental geometry. The dominant transitions are, in this case, towards the a_{1g} state at 707.5 eV, with a fully out-of-plane d_{z^2} spatial symmetry, and the projection of the e_g states along the z direction, at around 709.0 eV. We first notice that the AFM alignment is preserved in this configuration, despite the different structural and electronic environment surrounding the FePc molecule (see Sec.2.1), less interacting with the underlying Gr/Co support.

For the sake of completeness we report in Fig. 4.7 the spectra acquired at the Fe $L_{2,3}$ edge for FePc deposited on Gr/1 ML (left) and 6 ML Co (right) acquired both in a normal

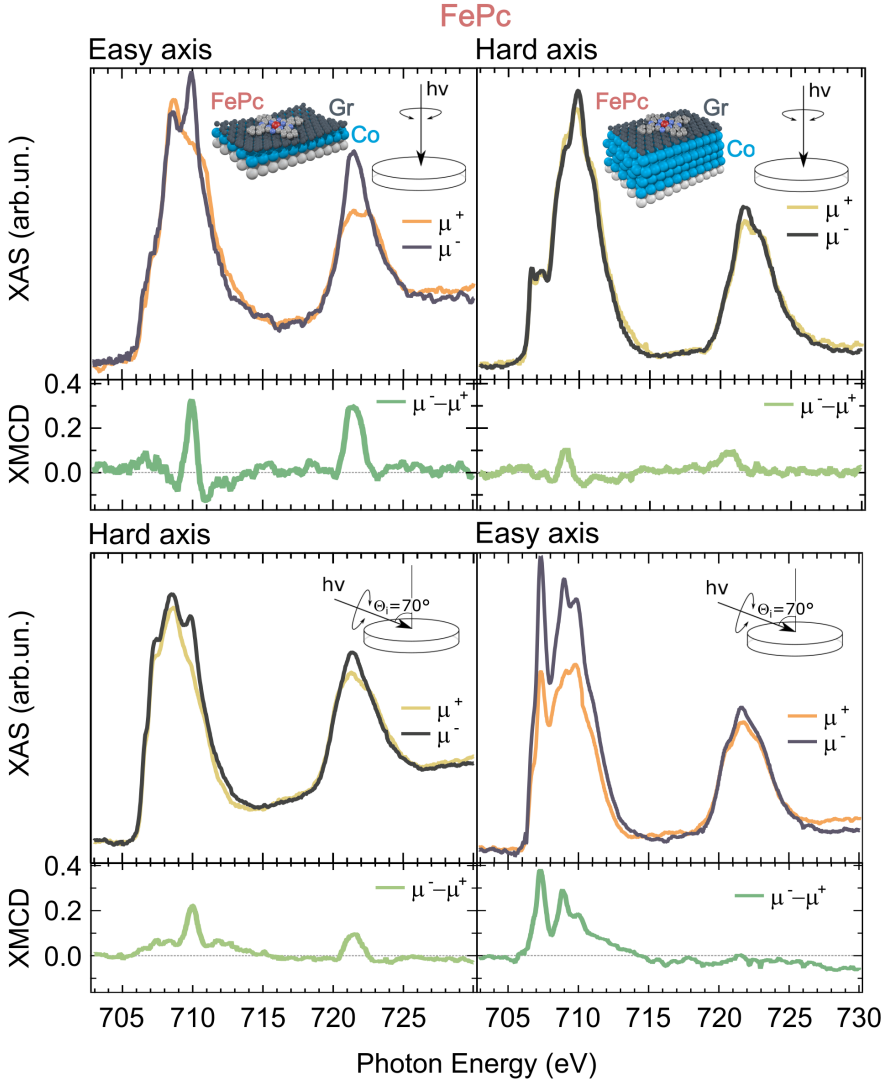

Figure 4.7: XAS and XMCD measurements at the Fe $L_{2,3}$ edges for FePc deposited on Gr/1 ML (left) and 6 ML (right) Co, as sketched in the figures. The spectra were acquired in remanence conditions, at T= 3 K and in a normal (top) as well as grazing (bottom) incidence geometry, as reported as an inset.

(top) and grazing (bottom) experimental geometry. If we compare the top and the bottom line we notice that the easy magnetization direction of the molecules switches from easy-axis (FePc/Gr/1 ML Co) to easy-plane (FePc/Gr/6 ML Co) at increasing Co thickness, hence assuming that of the substrate.

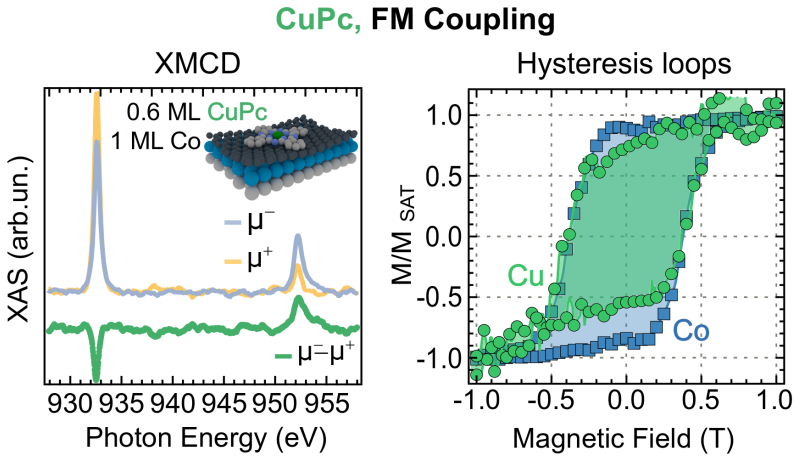

Figure 4.8: Remanent XAS and XMCD spectra (left) and element-selective hysteresis loops for 0.6 ML CuPc on Gr/1 ML Co/Ir(111), highlighting the weak FM alignment. The measurements were performed at NI, *i.e.*, along the easy magnetization axis of the molecule-metal complex, at T=2 K.

4.1.2 CuPc/Gr/Co: a 90° super-exchange interaction

In the case of FePc on Gr-Co the antiparallel alignment was driven by the symmetry-matching between the Gr π states and the molecular orbitals protruding out of the molecular plane. In order to deepen our knowledge in such coupling mechanisms as well as unravel the role of the TM centres and of the spin-polarized molecular orbital symmetry, we selected a TMPc unit with a purely in plane $3d$ state carrying the magnetic moment. The isolated CuPc molecule, with its d^9 electronic configuration, presents only one hole in the b_{1g} state, a molecular orbital with 27% N$2p$ weight and a Cu fully in plane $d_{x^2-y^2}$ contribution [162, 163]. This would allow to investigate the role of the orbital occupancy and symmetry in the Gr-mediated TM-Co magnetic coupling.

In Fig. 4.8 the experimental data acquired for a submonolayer coverage of CuPc adsorbed on Co-intercalated Gr with out-of-plane magnetic anisotropy are presented. As detailed in Sec.3.2, the XAS spectrum at the Cu $L_{2,3}$ absorption edge is characterized by two sharp white lines located at 932.5 eV and 952.0 eV, respectively due to the transitions from the Cu $2p_{3/2}$ and $2p_{1/2}$ core levels to the half-empty b_{1g} orbital, with a $d_{x^2-y^2}$ planar symmetry. It is impressive that the magnetic coupling has switched from AFM to FM, as can be noticed by the sign switching of the dichroic response, from positive (*i.e.*, opposite to Co) for FePc to negative (*i.e.*, same as Co) for CuPc.

As detailed in Sec.3.1, theoretical simulations find an identical adsorption geometry, with similar flat-lying orientation and molecule-substrate distance, for FePc and CuPc

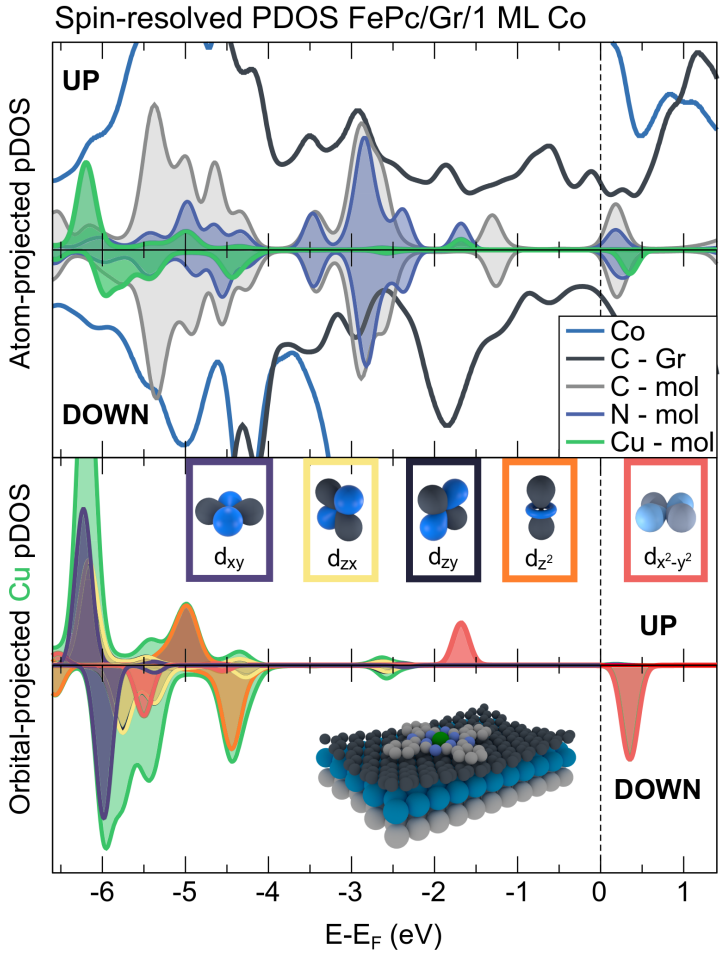

Figure 4.9: The calculated spin-resolved projected density of states is reported as projected on the different atomic species (top) for a single CuPc molecule on Gr/1 ML Co/Ir(111). The pDOS of the central Cu ion is then decomposed in spherical harmonics and projected on the d orbitals (bottom).

molecules on Gr/Ir(111) intercalated with 1 ML of Co. Therefore, since we can rule out any structural effect, only the occupancy and symmetry of the molecular orbitals can be responsible for the switching from AFM to FM coupling. Lüdwin charge analysis was performed also for this system, resulting in much weaker magnetic moments of the molecular C atoms (see also Tab.4.1), and a magnetization equally distributed over the Cu ($d_{x^2-y^2}$ state) and the surrounding N *pyrrole* atoms, as clarified by the net magnetizations reported in Tab.4.1. The spin-resolved projected DOS highlights the negligible contribution of the C-based molecular states, while a clear spin imbalance, aligned with that of Co, can be noticed for N and Cu, rising from the $d_{x^2-y^2}$ orbital, as expected and confirmed by further projection of the DOS onto spherical harmonics (bottom panel of Fig. 4.9).

In this case, as pictured in Fig. 4.9, the coupling mechanism was identified to be a

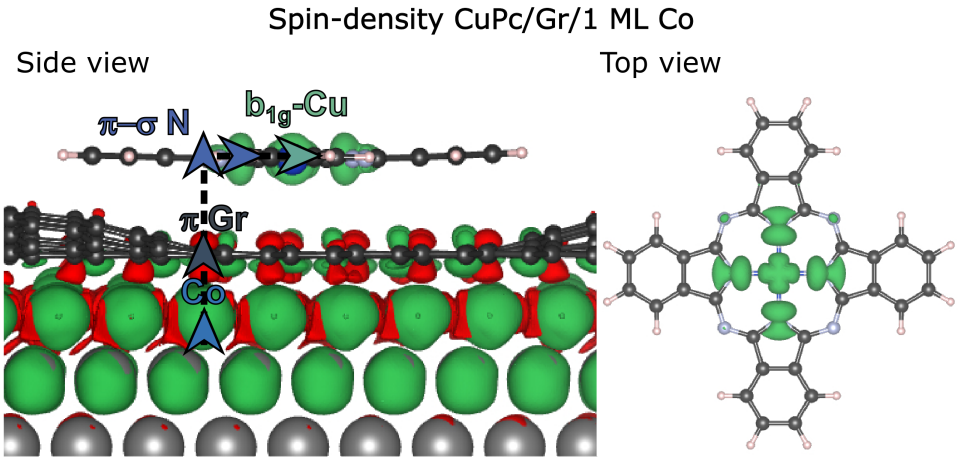

Figure 4.10: Theoretically calculated spin-resolved isosurfaces of CuPc adsorbed on Gr/Co from the side (left) and top (right) views. The proposed 90° super-exchange path is highlighted.

90° super-exchange interaction. In particular, the magnetic coupling is mediated by the π orbitals of the Gr sheet and of the organic ligands, as well as through the σ orbitals of the macrocycle, in a 90° symmetry rotation of the mediating orbitals, strongly hybridized with the $d_{x^2-y^2}$ state located on the central Cu ion and only weakly affected by adsorption (see Sec.3.2) [129]. Accordingly, this super-exchange mechanism usually favors a (weaker) FM coupling.

Given that the spin-polarized molecular orbitals lie parallel to the molecular plane for this case, the magnetic anisotropy of the CuPc molecules is strongly easy-axis and, hence, parallel to that of the Gr/1 ML Co substrate. When adsorbed on an in-plane magnetized surface, as Gr/8 ML Co, it exhibits a frustrated coupling, without zero-field magnetic remanence, as confirmed by the experimental data in Fig. 4.11. A fitting of the magnetization curve, assuming a magnetic moment J of 0.5 $\pm$ 0.1 μ_B, revealed an exchange energy as low as (1.6$\pm$0.1)$\times 10^{-5}$ eV, confirming the magnetization frustration. Indeed, the out-of-plane anisotropy of adsorbed CuPc molecules is so strong [162] that the exchange field of the substrate is not able to rotate the magnetic moment of the adsorbed molecule, but just mixes $\uparrow$ and $\downarrow$ states in equal amounts leading to zero remanence, as also observed for the strongly out-of-plane anisotropic $TbPc_2$ deposited on in-plane magnetized Ni films [33].

The proposed Gr-based molecular spin architectures present a tunable AFM/FM magnetic alignment, respectively, driven by a 180° and a 90° super-exchange path, triggered by the symmetry of the molecular orbitals carrying the magnetic state, as unraveled with

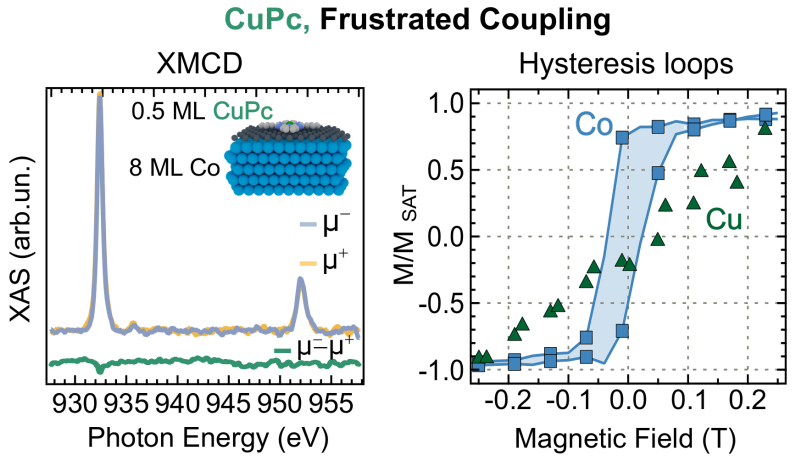

Figure 4.11: Remanent XAS and XMCD spectra (left) and element-selective hysteresis loops for 0.5 ML CuPc on Gr/8 ML Co/Ir(111), exhibiting no residual dichroism due to the frustrated coupling. The measurements were performed at GI, *i.e.*, along the easy magnetization direction of the Co-intercalated Gr substrate, at T=2 K.

a twinned experimental/theoretical approach. The pivotal role in this scenario is played by the transition metal center and by the spin-polarized molecular orbitals. As will be detailed in the next section, selecting the proper central metal ion can further optimize the magnetic response of the TMPc/Gr/Co spin interface.

4.2 MnPc/Gr/Co: can we optimize the spin interface?

To further optimize the magnetic state of TMPc networks self-assembled on the rippled Gr/Co support, we selected a molecular spin unit with high magnetic moment and high MAE. Among all TMPcs, MnPc molecules have the highest magnetic moment (3.2 μ_B) and MAE (2.7 meV) with an easy axis perpendicular to the surface plane [164]. Accordingly, it is the perfect candidate to improve the robustness against thermal fluctuations of the network magnetic state, once coupled with Co-intercalated Gr and with sufficiently high exchange energies.

In Fig. 4.12 the XMCD spectra at the Mn $L_{2,3}$ edge and the field dependence of the magnetization are presented for a thick MnPc film, as acquired at NI and GI. The film has a clear easy-axis magnetic anisotropy with paramagnetic behaviour, without a detectable magnetic remanence at temperature as low as 3 K. Furthermore, as also reported by T. Kataoka and co-workers for a MnPc crystal in its β polymorph [165], magnetic fields as high as 6 T are not able to fully align the molecular spins and saturate the magnetization, as evident in the hysteresis loops in Fig. 4.12. Indeed, as evaluated with a Langevin fit (T=2.8

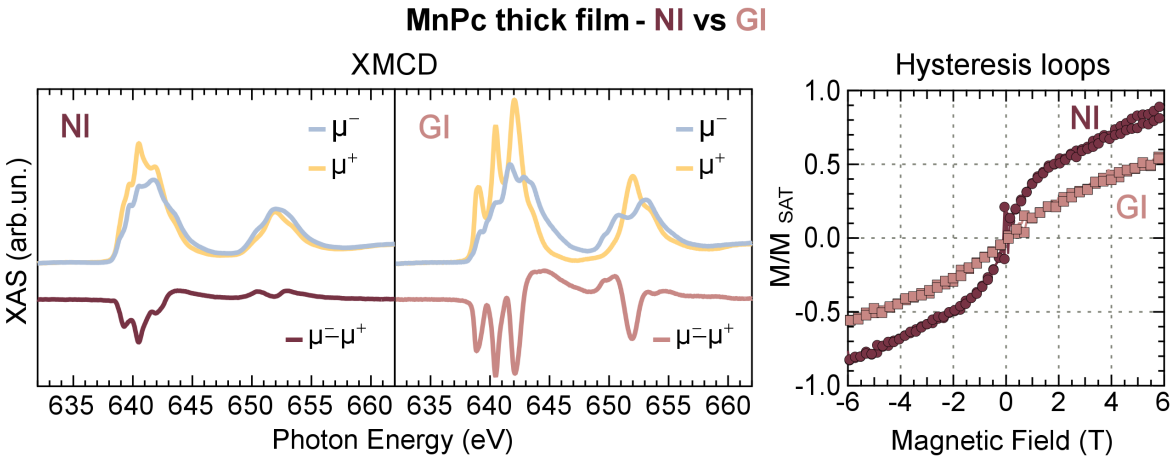

Figure 4.12: XMCD spectra for a thick MnPc film, as acquired in a normal (left) and grazing (center) incidence experimental geometry, immersed in a magnetic field of 6 T and at a temperature of 3 K. In the right panel the field-dependence of the XMCD signal is reported, measured in the same experimental conditions.

± 0.3 K, J=1.4 ± 0.2 μ_B) of the magnetization curves, we are only able to reach around 80% of the saturation magnetization by applying a 6 T magnetic field along the easy magnetization direction. Nevertheless, the XMCD measurements reported in Fig. 4.12 perfectly resemble the shape associated to the ^4E_g ground state configuration via cluster-model calculations, as reported in Ref. [165]. This confirms that MnPcs have a S=3/2 spin ground state associated with a $b_{2g}(d_{xy})^1\ e_g(d_{xz,yz}/d_\pi)^3\ a_{1g}(d_{z^2})^1\ b_{1g}(d_{x^2-y^2})^0$ $3d$ states occupation. This implies that both out-of-plane and in-plane symmetric molecular orbitals are available, matching the symmetry criteria for activating both the 180° and the 90° super-exchange paths described in the previous section and depicted in Fig. 4.13.

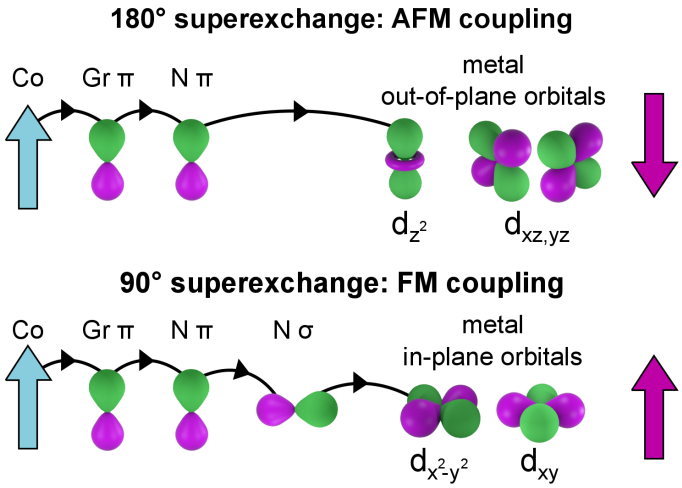

Figure 4.13: 180° (top) and 90° (bottom) super-exchange interaction paths, for details see Sec.4.1.

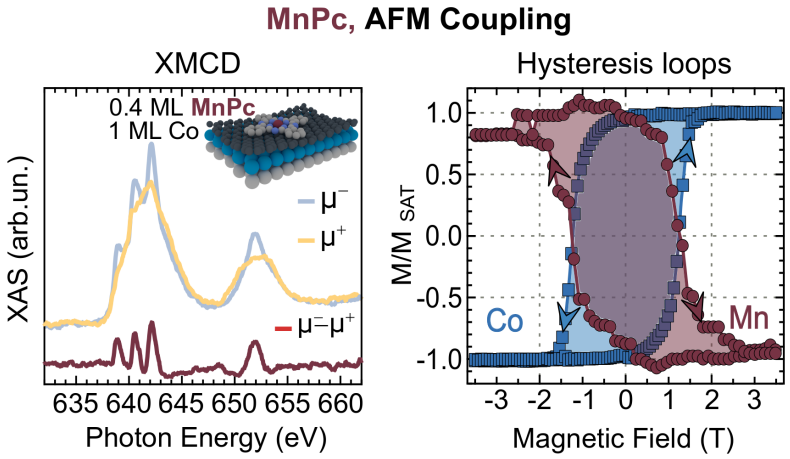

Figure 4.14: Remanent XAS and XMCD spectra (left) and element-selective hysteresis loops for 0.4 ML MnPc on Gr/1 ML Co/Ir(111), confirming the strong AFM alignment. The measurements were performed at NI, *i.e.*, along the easy magnetization axis of the molecule-metal complex, at T=2 K.

In Fig. 4.14 the XAS and remanent XMCD measurements acquired at the Mn $L_{2,3}$ absorption edges in a NI experimental geometry are reported. In this configuration the contribution of the in-plane symmetric molecular orbital is probed. The spectral lineshape is not altered upon adsorption with respect to a thick MnPc film, as presented in Fig. 4.12, preserving the three main features at 638.9 eV, 640.5 eV and 642.1 eV of the L_3 edge, with the L_2 being less structured. Therefore, we can conclude that the ground state configuration is protected by the Gr layer and is not modified upon adsorption on Gr/Co. However, a direct attribution of the XAS feature to a precise electronic transition is hindered in MnPc by strong electron correlation effects, as explained in Sec.3.2, and hence identification of the contribution of the single molecular orbitals is precluded. Nevertheless, we can notice that the AFM alignment is undoubtedly confirmed by element-resolved hysteresis loops in the right panel of Fig. 4.14. This means that, when magnetically polarized molecular orbitals protruding out of the molecular plane are available, the 180° super-exchange path is triggered and dominates the coupling, inducing an AFM order. In this case the molecule and substrate easy magnetization axes are aligned, hence the 180° super-exchange mechanism optimizes the stability against thermal fluctuations of the magnetic response, as will be detailed in the next section.

A similarly strong AFM alignment is observed when MnPc molecules are deposited on In-Plane (IP) Gr/Co substrates, Fig. 4.15, supporting the effectiveness of the 180° superexchange path in driving a strong AFM alignment also when the molecule and sub-

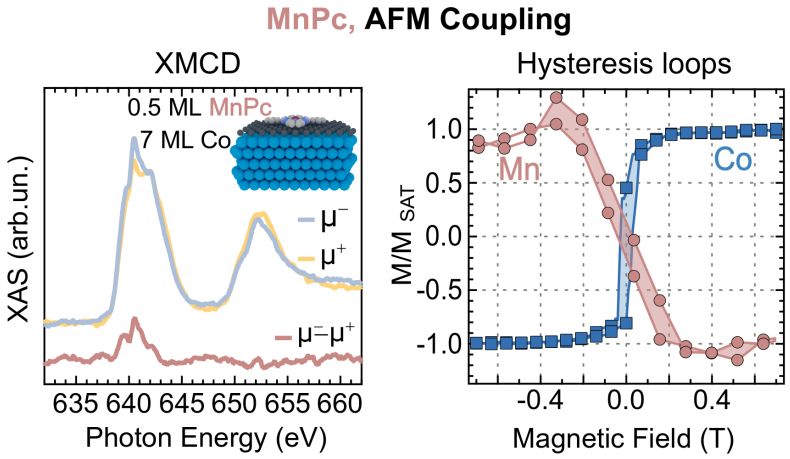

Figure 4.15: Remanent XAS and XMCD spectra (left) and element-selective hysteresis loops for 0.5 ML MnPc on Gr/7 ML Co/Ir(111), highlighting the strong FM alignment. The measurements were performed at GI, *i.e.*, along the easy magnetization axis of the molecule-metal complex, at T=2 K.

strate easy magnetization directions are perpendicular to each other, in analogy to what is found for in-plane anisotropic FePc adsorbed on the out-of-plane polarized Gr/1 ML Co.

Theoretical calculations have not been performed on this peculiar molecular spin interface because of (i) the large number of holes in the Mn^{2+} d^5 configuration and (ii) the strong correlation effects. However, being the adsorption geometry mainly driven by the organic anchor of the molecules and almost insensitive to the central transition metal atom (see Sec.3.1 for details), we can reasonably assume that the structural arrangement of MnPc on Gr/1 ML Co is similar to that of FePc and CuPc molecules on the same substrate, with identical planar configuration (as confirmed by XAS experiment at the N K-edge, Sec.3.1) and Mn-Co distance.

4.3 Robustness against thermal fluctuations of the magnetic response

To test the stability of the proposed super-exchange mechanisms, XMCD measurements were carried out at increasing sample temperature, as reported in Figs.4.16 and 4.17. The experiments were performed by changing the temperature of the cryostat and wait for proper thermalization, the data were normalized by the integral of the averaged $(\mu^+ + \mu^-)/2$ signal and then compared to the signal acquired at low sample temperature (3 K)

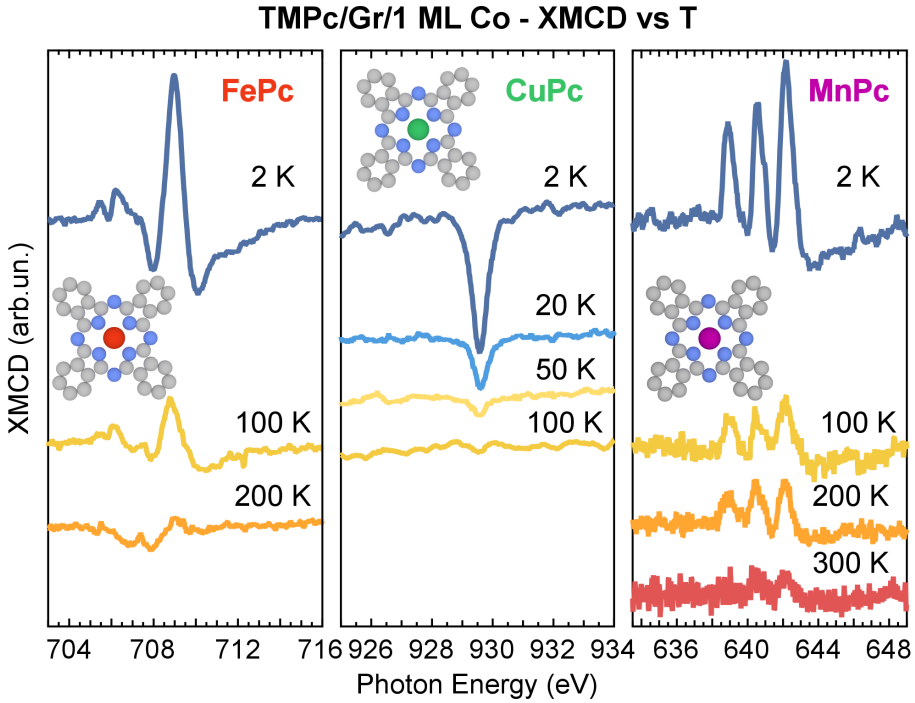

Figure 4.16: Evolution of the XMCD spectra at increasing sample temperature for FePc (left), CuPc (centre) and MnPc (right) molecules on Gr/1 ML Co.

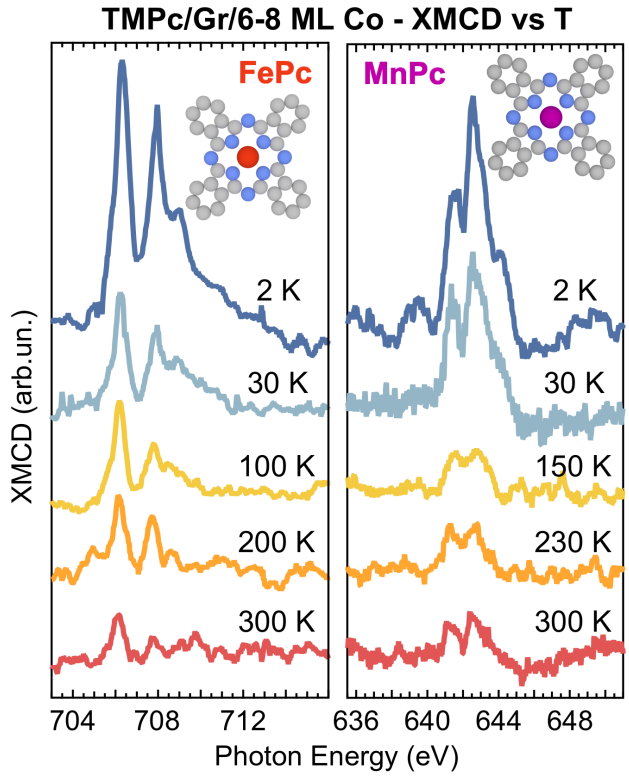

Figure 4.17: Evolution of the XMCD spectra at increasing sample temperature for FePc (left) and MnPc (right) molecules on Gr/6-8 ML Co.

in Fig. 4.18. We want to emphasize that the whole measurement session was performed over several hours without re-applying the magnetic field, indicating that the magnetic state survives time and X-ray exposure.

We can identify three configurations with RT remanence: MnPc adsorbed on both Out-Of-Plane (OOP) and IP anisotropic Gr-Co and FePc when the easy magnetization directions of the molecules and the substrate are aligned (FePc/Gr/6 ML Co). From the presented experimental results it can be noticed immediately that the 180° super-exchange path is much stronger than the 90° one, since the magnetic state of CuPc molecules vanishes already at 50 K, while the one of FePc and MnPc survives respectively up to 200 K and 300 K on the rippled Gr/1 ML Co. The different robustness against thermal fluctuations for FePc and MnPc can be ascribed to the higher spin magnetic moment of the Mn centres as well as to the parallel(perpendicular) orientation between the easy magnetization directions of the Gr/Co substrate and the MnPc(FePc) molecules in this configuration. When TMPcs are adsorbed on Gr/IP Co, only FePc and MnPc exhibit a non-zero magnetic coupling. We can notice that the trend is similar for the two samples, even though the easy magnetization directions of the molecular units are different [76, 166]. This indicates that, despite the large predicted easy-axis magnetic anisotropy of the MnPc molecules, the proposed super-exchange mechanism is still efficient even in this configuration, with the MnPc and Gr/Co easy magnetization direction being perpendicular to each other.

The temperature dependence of the XMCD signal can be used to extrapolate, by approximating the substrate with its exchange field, the exchange energy of the coupled magnets. Indeed, a fit function of the form:

$$M_{TM}(T) = M_{Co}(T)[\frac{2J+1}{2J}coth(\frac{2J+1}{2J}\cdot\frac{E_{ex}}{k_BT}) - \frac{1}{2J}coth(\frac{1}{2J}\cdot\frac{E_{ex}}{k_BT})] \tag{4.3.2}$$

was used to model the experimental data in Fig. 4.18, the square brackets containing the explicit form of the Brillouin function $B_J(\frac{E_{ex}}{k_BT})$, according to Refs. [44, 153]. We want to point out that the XMCD spectrum of Co was also probed at each temperature, resulting in a stable, nearly constant magnetization in both configurations. With this model we assume that the thermal fluctuations of the molecules and of the substrate are strongly correlated to each other. The fit results are reported in Tab.4.2.

The adopted J values are the spin magnetic moments, as the exchange energy only deals with the spin contribution to the magnetic moment, of the isolated molecule, fully

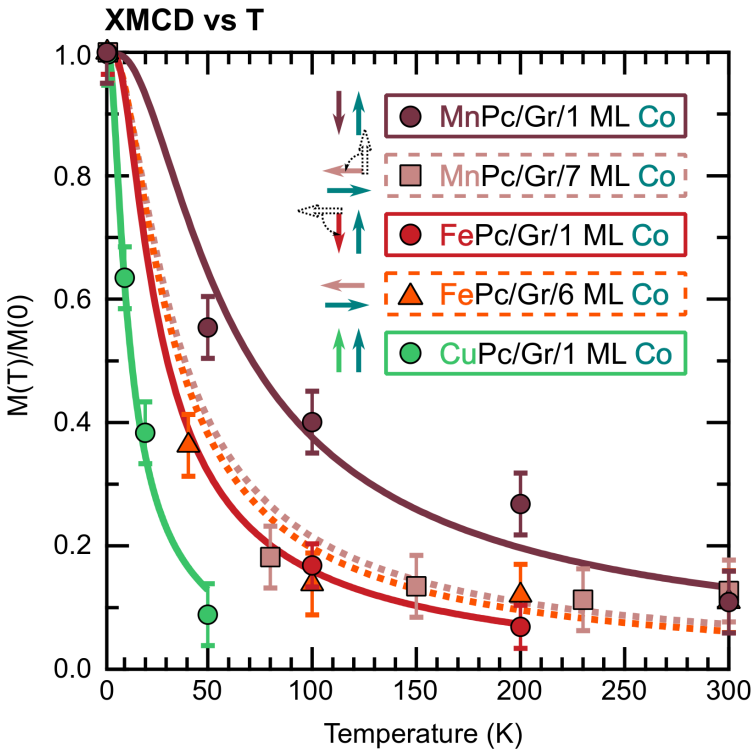

Figure 4.18: Temperature dependence of the XMCD intensity, normalized with respect to the extrapolated 0 K value. The curves (solid for TMPc on OOP Gr/Co and dashed for TMPc on IP Gr/Co) represent the Brillouin-fit performed over the experimental data.

Configuration	J	E_{ex} (meV)
FePc/Gr/1 ML Co	1.0	2.1 ± 0.6
FePc/Gr/6 ML Co	1.0	2.8 ± 0.5
CuPc/Gr/1 ML Co	0.5	0.6 ± 0.2
MnPc/Gr/1 ML Co	1.5	6.2 ± 0.7
MnPc/Gr/7 ML Co	1.5	3.4 ± 0.4

Table 4.2: Exchange energies for the investigated configurations, as extracted by the Brillouin fit over the experimental data, details in the text.

preserved upon adsorption on Gr/Co thanks to the Gr buffer layer. An exchange energy as high as 6.2 meV is found for MnPc/Gr/1 ML Co, and it is the highest value for this peculiar class of systems. The magnitude of the exchange energy needs to be compared with the intrinsic MAE of the molecular compounds, and always outweighs them (MAE_{MnPc}=2.72 meV and MAE_{FePc}=-1.18 meV [2]) in the cases studied in this thesis. This means that the stabilized magnetic state may be only ascribable to the Gr-mediated TMPc-Co super-exchange coupling, winning the competition with the intrinsic magneto-crystalline anisotropy of the molecular units [167].

We want to emphasize that, when planar magnetic molecules are adsorbed directly on magnetic surfaces, exchange energies around 70 meV are found, as estimated by M. Bernien and co-workers for Fe porphyrin on Co [168] and confirmed by S. Bhandary and his collaborators for FeP on different facets of Co and Ni [150]. However, for this class of systems the metal-related molecular orbitals are strongly hybridized with the metal extended state and the magnetic state of the adsorbed molecular units is affected by interaction. In the present case, even though the magnetization is induced by coupling with the intercalated Co layer(s), the magnetic moment of the adsorbed TMPcs is protected by the presence of Gr. Notably, the Gr layer plays a dual role: on the one hand it decouples the adsorbed molecule, preventing orbital intermixing with the substrate that would reduce/quench the molecular magnetic moments; on the other hand it enables and actively mediates an effective spin interaction between the adsorbed molecules and the intercalated Co layer(s).

4.4 Conclusions

In this chapter we have presented the magnetic response of molecular spin interfaces constituted by TMPc adsorbed on the tunable Gr/Co support. We have demonstrated, via a twinned experimental and theoretical approach, that two different super-exchange paths are available and couple the central transition metal ion with the intercalated Co layer(s). The sign and strength of the magnetic coupling depends on the occupancy and symmetry of the spin-polarized molecular orbitals located on the TM centers. In particular, when the magnetic moment of the molecular units is carried by molecular orbitals with a dominant

[2] The minus sign in the MAE of FePc molecules indicating an in-plane easy magnetization direction, contrary to the out-of-plane one of the (positive MAE) MnPcs.

out-of-plane symmetry, a strong AFM alignment is driven by a 180° Co d_{z^2}– Gr π– Pc π– Fe d_{z^2},d_{π} super-exchange mechanism, stabilizing the magnetic state of the adsorbed molecules against thermal fluctuations up to 300 K when the molecule and substrate easy magnetization directions are aligned. On the other hand, when this path is hindered and the spin-polarized molecular orbitals lie parallel to the molecular plane, a weaker parallel alignment is induced by a 90° super-exchange path, involving the σ orbitals of the Pc cage. This interaction channel leads to a much weaker FM coupling, fragile against thermal excitation. Finally, we have identified MnPc molecules as ideal candidates to optimize the magnetic state of the spin interface, with both perpendicular and in-plane orientations, thanks to their relatively high magnetic moment and out-of-plane easy axis.

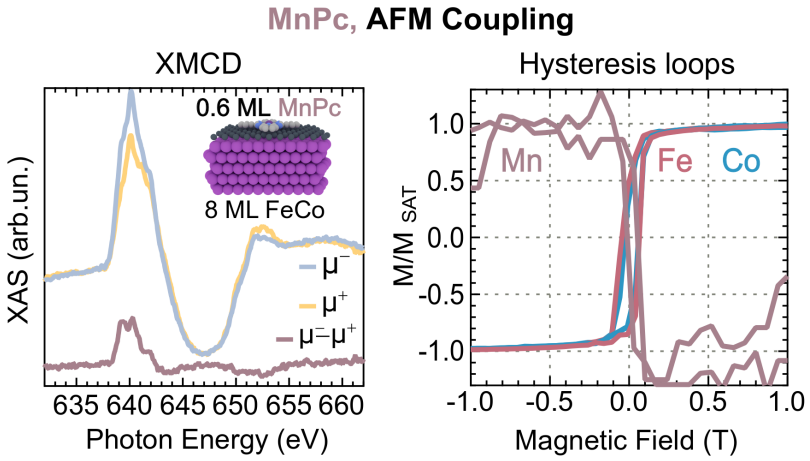

Figure 4.19: Left: XMCD measurements at the Mn $L_{2,3}$ absorption edges acquired in remanence conditions and at low sample temperature (3 K), without background subtraction. Right: magnetization curves acquired for Fe (red), Co (blue) and Mn (pink), highlighting the AFM alignment.

The magnetic state of the spin interface is driven by a strong super-exchange coupling with the intercalated Co layer(s). The sign and the strength of the magnetic coupling is determined by the symmetry of the molecular states carrying the magnetic moment as well as by the stable magnetic state of the substrate. In the following sections we will present some preliminary results on *(i)* the effects of the enhanced Gr/FeCo magnetic moment on the robustness of the molecular magnetic response against thermal fluctuations, to strengthen the coupling and increase RT remanence; *(ii)* electron injection at the MnPc/Gr/Co interface, to alter the charge density distribution across the molecule and investigate how it impacts on the N-mediated magnetic coupling.

4.5 Perspectives: Optimization of the substrate magnetic state

In Chap.2 we proposed the simultaneous intercalation of Fe and Co as a viable route to increase the magnetic moment of the GrFM substrate. The MnPc-FeCo coupling through Gr can enlighten how the magnetic moment of the FM layer influences the exchange energy and, accordingly, the robustness of the molecular magnetic state against thermal fluctuations.

In Fig. 4.19 we report the XMCD measurements performed at the Mn $L_{2,3}$ absorption edges for 0.6 ML MnPc deposited on Gr/8 ML FeCo, at low sample temperature and at

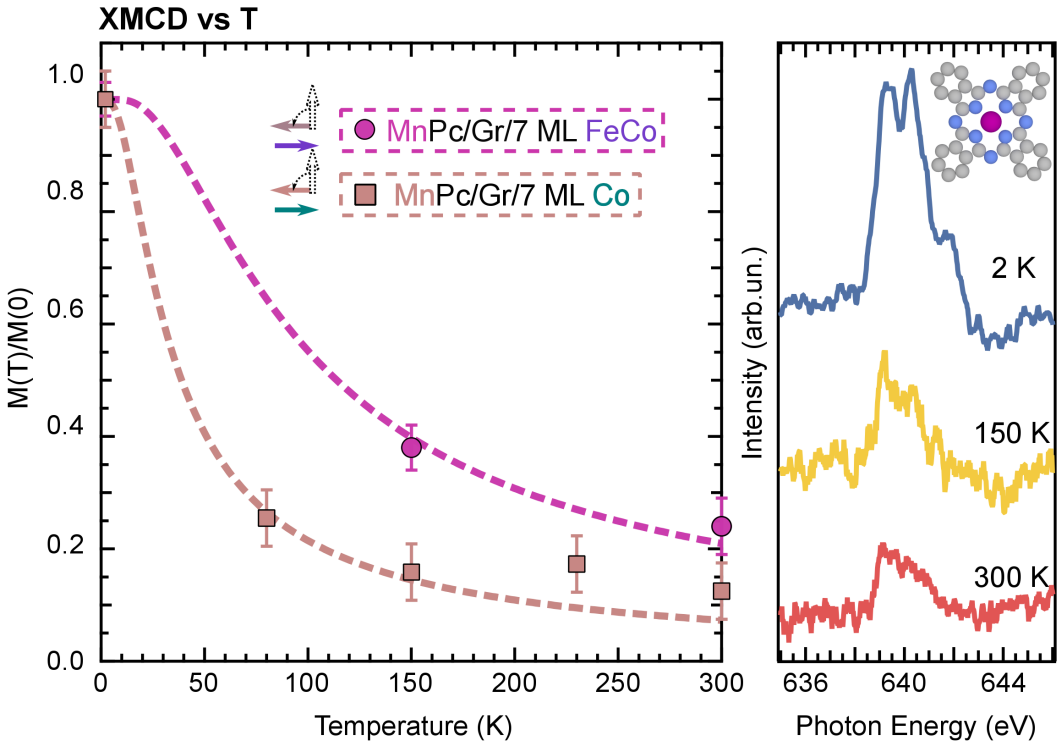

Figure 4.20: Integrated XMCD signal (raw data in the right panel) at increasing sample temperature. The Brillouin fitting curve is superimposed as a dashed curve to the experimental data.

GI. In the right panel of Fig. 4.19 the element-sensitive hysteresis loops acquired for Mn (pink), Fe (red) and Co (blue) in the same experimental conditions are also presented. The AFM coupling is confirmed also when Fe is co-intercalated with Co, as can be deduced by XMCD measurements performed in remanence (left in Fig. 4.19) and as a function of the applied magnetic field (right in Fig. 4.19). The shape of the XMCD spectrum is similar to the one measured for MnPc/Gr/Co acquired at low temperature and at GI (Fig. 4.15), with similar strength against the applied magnetic field. This suggests that the electronic and magnetic interactions between adsorbed MnPc molecules and intercalated magnetic metals are similar for pure Co and FeCo alloys.

To prove that this concept effectively optimizes the spin architecture, we performed XMCD measurements as a function of sample temperature, presented in Fig. 4.20. The remanent dichroic signal at RT is around 25% of the one at 3 K, more than two times higher than the best configuration studied for bare Co (*i.e.*, for aligned molecule-substrate easy magnetization directions). A Brillouin fit was performed, according to Eq.4.3.2 with a similarly preserved J=3/2 fit parameter, and an exchange energy as high as 9.9 ± 1.0 meV was determined. This confirms that the enhanced magnetic activity of both the

molecular units, with suitable TM centers, and the ferromagnetic substrate can effectively optimize the magnetic state of the TMPc/Gr/FM interfaces.

4.6 Perspectives: Tuning the magnetic coupling via electron injection

In the previous sections we investigated the role of the symmetry of the molecular orbitals located on both the organic Pc ring and the transition metal centres. In particular, we found that the symmetry-matching between orbitals with out-of-plane character is crucial to determine the strong AFM coupling. We now want to alter the charge density distribution via electron injection with alkali metals, K in the present case, to see how this will affect the super-exchange interaction and the magnetic coupling. Among all TMPcs, MnPc molecules exhibit the lowest energy gap [169] and ionization potential, with the highest electron affinity [170], hence making it the perfect candidate for charge-transfer investigations.

The tuning of TMPc properties by electron(hole) doping has been intensively investigated for thick TMPc films [171, 172], but only few examples are available for molecular layers at the interface [173]. In particular, differently from other TMPcs, for MnPc molecules three (instead of two) K-doped phases were identified, being K_1MnPc, K_2MnPc and K_4MnPc [172]. This difference was attributed to the presence of the Mn $3d$ orbital being very close to the chemical potential and lying in-between the purely organic a_{1u} and e_g ligand orbitals. B. Mahns and co-workers infer that the first donated electron is transferred to a molecular orbital with a predominant Mn $3d$ character, while additional doping leads to the occupation of the ligand e_g states [172]. S. Stepanow and co-workers performed scanning tunneling microscopy investigation of Li-decorated CuPc molecules on Ag(001). They identified two different adsorption configurations for the Li atoms: at lower coverages, it preferentially occupies a ligand site, donating charge to the organic LUMO orbital while, when the Li density is increased, electrostatic repulsion drives the deposition of Li ions on top of the metal site [173].

The K adsorption site inside the molecule is crucial to determine whether it donates the charge to the organic ligands or to the transition metal centres. To address this issue we performed NEXAFS measurements for MnPc deposited on Gr/1 ML Co at increasing K density, both at the Mn $L_{2,3}$ and at the N K absorption edges, as reported in Fig. 4.21.It

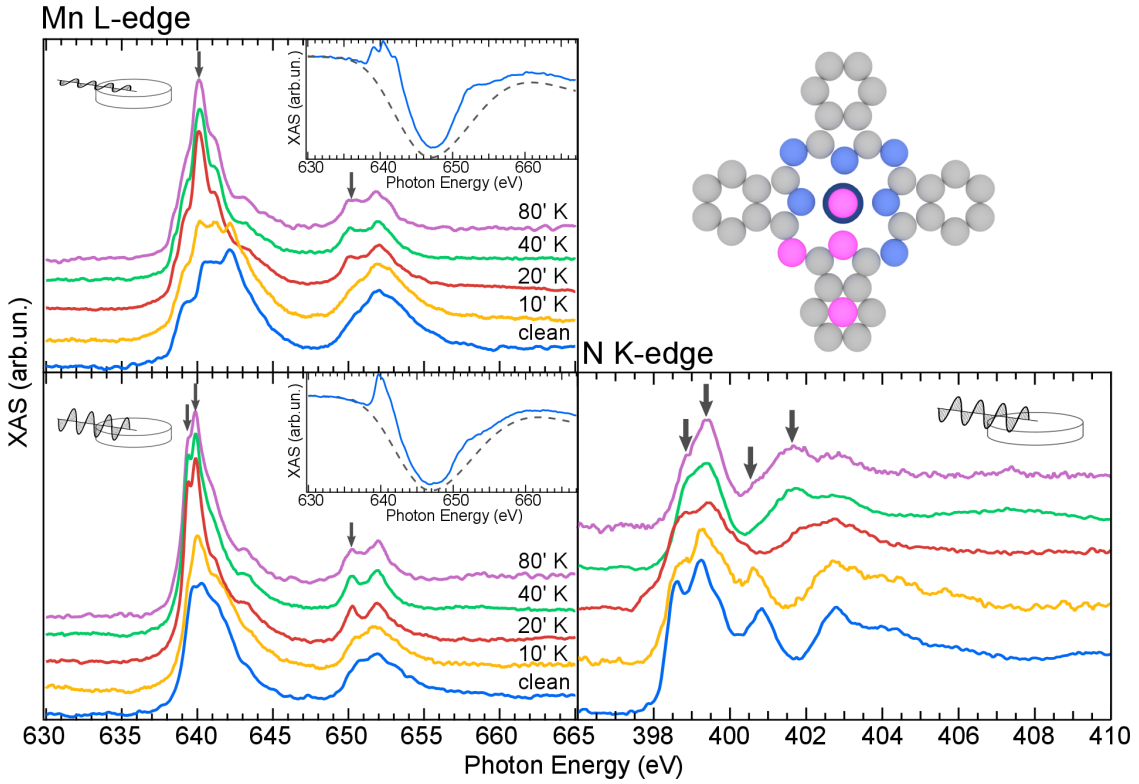

Figure 4.21: NEXAFS measurements at the Mn $L_{2,3}$ (left) and N K absorption edges acquired with out-of-plane (bottom) and in-plane (top) polarized light at increasing K coverage. In the top right part the possible K adsorption sites are sketched.

can be noticed that, upon alkali doping, the absorption response at the Mn $L_{2,3}$ edges to horizontally and vertically polarized radiation becomes isotropic. In particular, the spectrum gets gradually dominated by the sharp feature located at around 640 eV photon energy, while the other peaks slowly smear. S. Stepanow *et al.* found a similar evolution at increasing electron doping of MnPc/Ag(001) and attributed it to an intermediate-to-high spin transition due to crystal field modification, while the valence state of the Mn centres was found to be preserved [173]. On the contrary, B. Mahns and his collaborators observed a reduction of the Mn ions, towards an Mn(I) configuration [172]. To check for any alteration of the Mn valence state, in Fig. 4.22 we compare the NEXAFS measurement at the Mn L_3 edge for the saturated MnPc/Gr/Co sample with the spectrum acquired for Mn_2O, Mn_2O_3 and MnO_2, in which the Mn ions are in a 2^+, 3^+ and 4^+ oxidation state, respectively. The spectral lineshape of K-doped MnPc/Gr/Co is fairly similar to Mn(II) in Mn_2O and with Li-decorated MnPc/Ag(001) [173], with preserved Mn(II) valence state. Accordingly, we deduce that the valence state of the Mn centers is not reduced upon K doping and that a similar intermediate-to-high spin transition occurs.

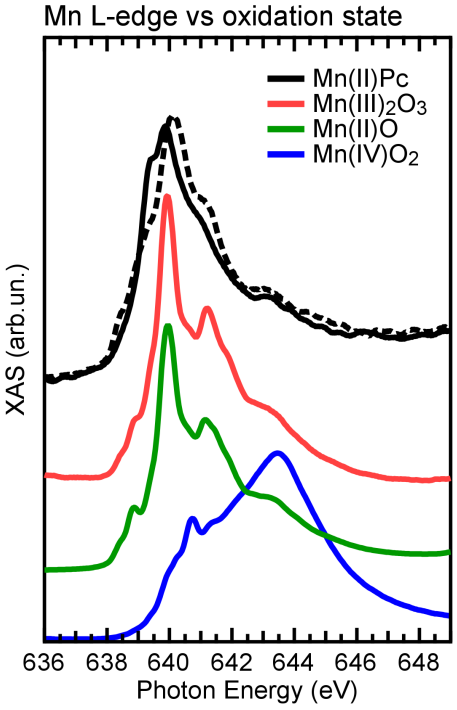

Figure 4.22: NEXAFS measurements at the Mn L_3 absorption edge for the K-doped MnPc/Gr/1 ML Co sample in comparison with what recorded for Mn in different oxidation states, namely Mn(II)O, $Mn(III)_3O_2$ and $Mn(IV)O_2$.

In Fig. 4.21 it can be observed that, for longer K dosing, no change in the NEXAFS spectra at the Mn $L_{2,3}$ edges occurs, while a remarkable evolution can still be noticed in the π^*-polarized N K edge (right part of Fig. 4.21). Notably, a sudden quenching of the *aza*-related peak can be observed at the early doping stages, while higher K coverage are required to fully quench the transitions towards the LUMO+1 orbital and cause a ∼1 eV shift of the fourth features towards lower photon energies. These significant changes upon electron injection pinpoint towards a complex evolution of the electronic environment surrounding the transition metal centers, strongly modifying the ligand field.

In order to check how the altered charge density distribution inside the MnPc molecule is reflected in the MnPc-Co magnetic coupling, XMCD measurements were performed at the Mn $L_{2,3}$ edges, with and without a 6 T magnetic field, for MnPc/Gr/1 ML Co at increasing K doping, as reported in the left panel of Fig. 4.23. Remarkably, the sign of the magnetic alignment is switched, being AFM in the pristine case and FM in the fully doped sample. Since the response to linearly polarized radiation gradually becomes isotropic upon electron injection, we also monitored the evolution of the magnetic response both in a NI and GI experimental geometries for subsequent K deposition, as reported in the central and right panel of Fig. 4.23. The loss of anisotropy is confirmed in this case: the clean sample has a clear easy-axis magnetic anisotropy, that turns easy-plane at the early K deposition stages and ends up almost isotropic for the fully doped sample, in agreement with what found by S. Stepanow and his collaborators [173].

To shed more light on the sign-switching of the magnetic coupling, we acquired the magnetization curves by monitoring the field-dependence of the dichroic signal both at 642 eV (maximum dichroism for the pristine MnPc/Gr/Co sample, F_1 in the following)

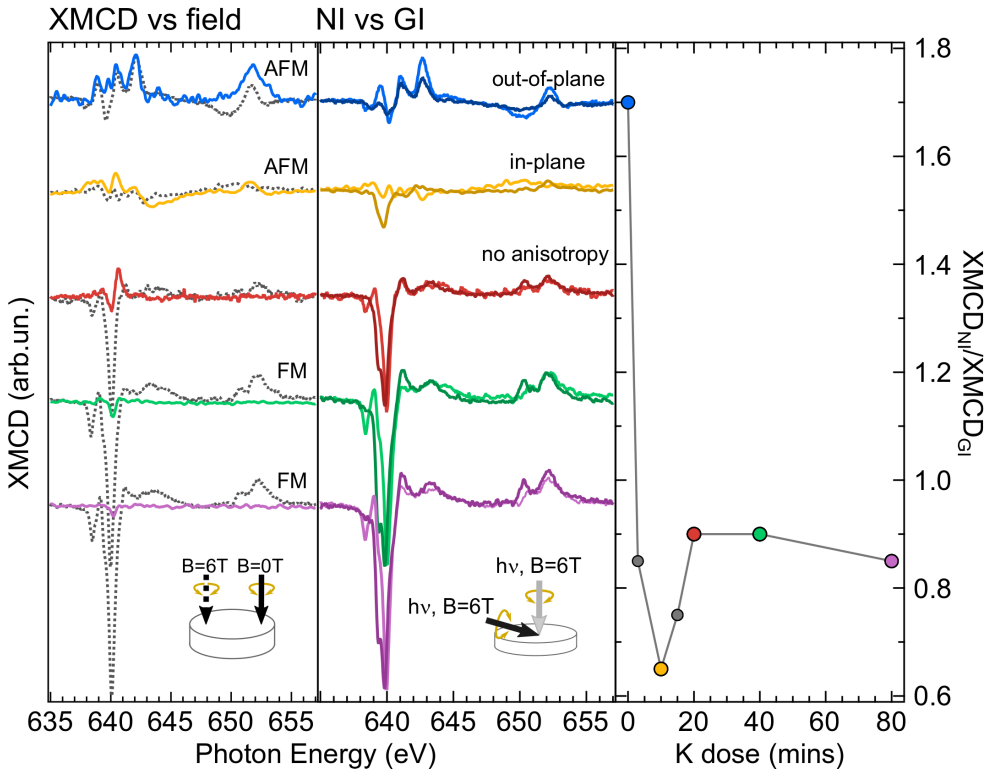

Figure 4.23: Left: XMCD measurements acquired with the sample immersed in a 6 T magnetic field, applied along the easy magnetization direction of the system (grey dashed lines) and in remanence conditions (full colored lines) at increasing K doping. Center: XMCD measurements performed with a 6 T magnetic field applied at NI (*i.e.*, along the easy magnetization axis of the pristine system, lighter lines) and at GI (*i.e.*, along the hard magnetization axis of the pristine system, darker lines). Right: evolution of the ratio between the integrated signals reported in the central panel at increasing K deposition.

and at 640 eV (maximum dichroism for the doped configuration, F_2 in the following), see Appendix A.2.3 for details. The results are presented in Fig. 4.24. The hysteresis loops for the clean sample are quite similar at the F_1 and F_2 features: they share the AFM alignment with Co and resemble its coercive field. When the sample is first exposed to K, the F_1 field evolution exhibits a reduced amplitude but maintains its square shape, while the F_2 trend is suddenly switched with a pronounced paramagnetic behavior. At further K depositions, the dichroism at F_1 feature vanishes at any field, while the F_2 peak dominates the spectrum and determines the magnetic state of the sample, parallel to that of Co but with small zero-field remanence.

We presented an overview on some preliminary results, testing the possibility to further tune the magnetic properties of our molecular spin interfaces by: enhancement of the substrate magnetic moment upon FeCo alloy intercalated below Gr; alteration of the

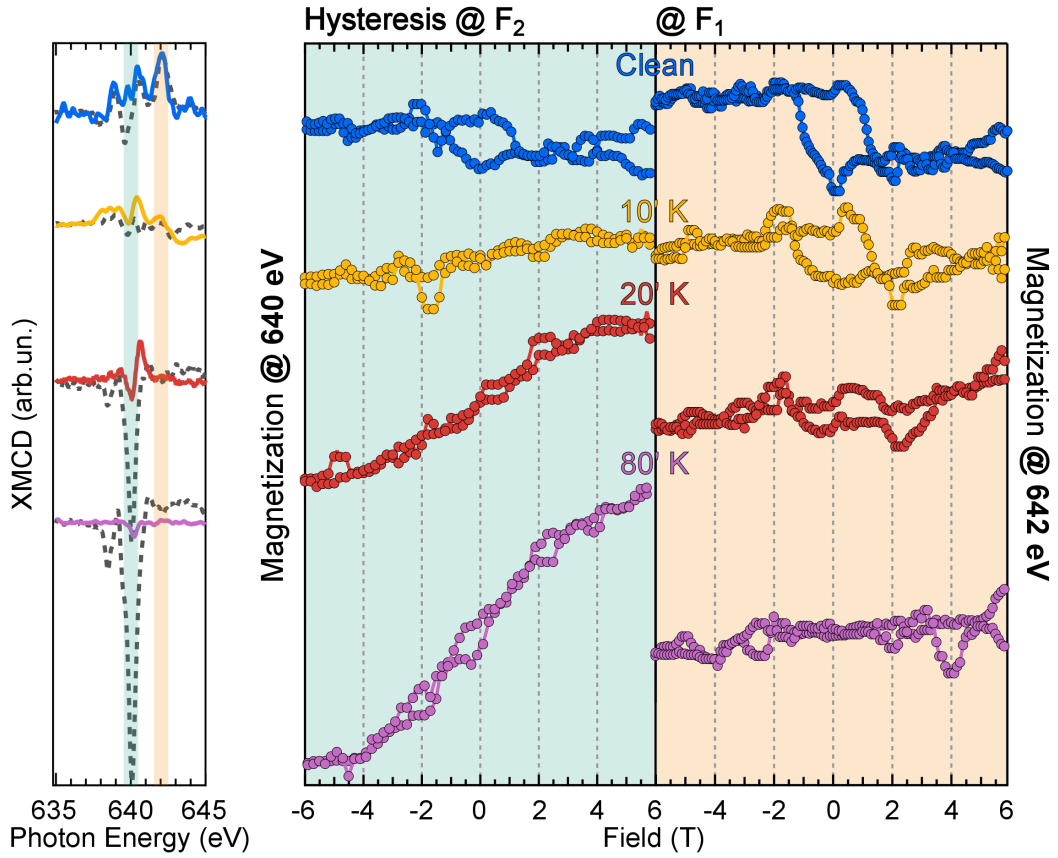

Figure 4.24: Magnetization curves at increasing K doping, acquired by monitoring the field-evolution of the dichroic signal at 640 eV (left) and 642 eV (right).

charge density distribution across the MnPc molecules via electron injection.

A similar AFM alignment was found for MnPc on Gr/FeCo, attributable to a 180° super-exchange interaction mediate by the Gr sheet and by the molecular orbital located on the Pc ring. The optimized magnetic configuration for Gr/FeCo/Ir(111) increased by around 40% the molecule-ferromagnet exchange energy, with an unprecedented value of 10 meV and an extremely high RT remanence. Furthermore, electron doping at the MnPc/Gr/Co interface led to an intermediate-to-high spin transition of the MnPc unit, followed by a switching of the magnetic coupling from AFM to FM, with tunable properties depending on the doping level.

A new platform is now open to design magnetic molecules and spin interface architectures with optimized magnetic response and with the desired functionalities. The work started with this Ph.D. thesis can indeed be further developed, following the proposed paths.

Chapter 5

Conclusions

In this thesis we have provided a systematic study of novel molecular spin architectures, magnetically coupled with ferromagnetic layer(s) intercalated below a Gr carpet. The presented experimental results propose a route to obtain well-ordered spin networks, with a stable structural arrangement and preserved electronic/magnetic state, magnetically coupled with an intercalated ferromagnetic metal/alloy. These complex spin architectures are almost completely electronically decoupled from the FM substrate and the magnetic coupling is quite strong, though the distance between the molecule metallic centers and the magnetic support is more than 5 Å. Furthermore, an important challenge accomplished is that the magnetic state of the system is robust against thermal fluctuations and survives up to RT for the spin interfaces with AFM coupling. The open questions and the challenging tasks proposed in the introduction of this thesis were accomplished, as detailed in the following.

1. *identify a suitable support for molecular spin interfaces with long-range ordering*: the Gr/Ir(111) substrate intercalated with ferromagnetic metals/alloys is a strategic support for novel spin networks. A single Co layer, sandwiched between the Gr sheet and the Ir(111) growth surface, arranges pseudomorphic to the Ir(111) surface, preserving the symmetry of the moiré superstructure but with enhanced corrugation. This induces the formation of inequivalent adsorption regions with a site-dependent surface potential modulation, that effectively traps the polarizable TMPc molecules driving the assembly of a well ordered Kagome lattice. The twinned experimental/theoretical approach disclosed a minimum energy landscape with TMPcs evenly-spaced in the valley regions of the rippled Gr sheet, flat-lying

with the molecular plane parallel to the sample surface and sitting at a distance of 5.15 Å from the intercalated Co layer, independently on the TM centers.

2. *control the charge transfer/orbital intermixing at the interface between the molecular units and the Gr-based support*: the TMPcs electronic interaction with the reactive ferromagnetic metal is (partially) screened by the presence of the Gr layer, shielding the electronic occupation and the symmetry of the molecular orbitals carrying the magnetic moment. Theoretical predictions confirmed that the ground state of the isolated TMPc unit is preserved upon adsorption, with unaltered magnetic moments. Hence, we propose a route to obtain an ordered network of molecular units with almost intact structural, electronic and magnetic configurations that can magnetically couple with the Co layer(s) through Gr.

3. *ensure thermal stability of the magnetic state*: a remarkable magnetic coupling is found between TMPcs and the Gr/Co support. In particular, it is driven by an effective 180° super-exchange interaction, triggered when the spin-polarized molecular orbitals, located on the transition metal center, have an out-of-plane symmetry, as is the case for FePc and MnPc. The magnetization is transferred from the Co states to the N π orbitals, through hybridization with Gr, overlapping with symmetry-matching TM d_π states. This mechanism favors an AFM TM-Co alignment, robust against thermal fluctuations. When this super-exchange path is hindered, as for CuPc with a single unpaired spin in a molecular orbital lying inside the molecular plane, an extra step is required and a 90° super-exchange channel opens up. The magnetic interaction is mediated by the N π through the N σ orbitals, strongly hybridized with the in-plane symmetric state of the Cu ion. This leads to a weaker FM coupling between the adsorbed CuPc molecules and the intercalated Co layer(s). By monitoring the evolution of the molecular magnetic state at increasing sample temperature we were able to extrapolate the exchange energies and we identified, by accurately selecting the magnetically active metal center, the optimized configurations, with non-vanishing magnetic remanence up to room temperature. In particular, MnPc molecules experience an exchange energy of 6.2 meV with Gr/1 ML Co, a value more than three times higher than those reported so far in the literature. This scenario, completely supported by the theoretical spin density calculated on the whole moiré cell, is robust against different exchange and correlation

functionals.

The choice of an effective superexchange path can ensure the stability against thermal fluctuations, even at RT, and it can be further improved with a fine control of the relative orientation of the molecule and substrate easy magnetization directions and of the magnetic moment of the Gr/FM support. This new class of systems can open a platform to design molecular spin network with optimized magnetic response. A further objective will be to *(i)* maximize the magnetic moment of the substrate, to enforce the coupling with the TMPc building block; *(ii)* tuning the symmetry and the charge density distribution of the molecular orbitals carrying the magnetic moment.

We have provided an optimized novel procedure to form a smooth and homogeneous FeCo alloy sandwiched between the Gr sheet and the Ir(111) surface. The increased magnetic activity of the FeCo alloys, with the highest magnetic moment and magnetic anisotropy energy among the $3d$ transition metals/alloys, is reflected on the thermal stability of the adsorbed MnPc magnetic state. Temperature-dependent measurements unraveled an exchange energy with an unprecedented value of around 10 meV, with an intense RT remanent magnetic activity. This value for the exchange energy is much smaller than what reported in the literature for metal-organic molecules directly in contact with FM surfaces. However, in those configuration the adsorbed molecule and the underlying ferromagnet form a single magnetic entity, with strongly hybridized molecule-metal states. The insertion of a Gr layer changes this picture, preventing strong chemical bonding and formation of frontier orbitals with hybrid molecule-metal contributions. Despite the increased molecule-metal distance and the hindered orbital intermixing, the molecular spin interfaces proposed in this thesis present a remarkably stable magnetic state, surviving up to RT.

The role of the symmetry of the molecular orbitals carrying the magnetic moment is crucial on the effectiveness of the activated super-exchange channel(s). We altered the charge density distribution of the frontier molecular orbitals via electron injection through alkali metal deposition, inducing an intermediate-to-high spin transition of the MnPc molecules as well as a switching of the magnetic coupling sign, from AFM to FM. In particular, a new molecular state arises and dominates the magnetic activity of the molecular spin interface, with isotropic magnetic response aligned parallel to the applied magnetic field and to the Co magnetization.

Direct adsorption on metallic surfaces

- Deformed molecular structure

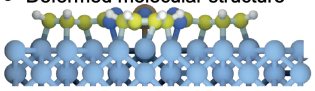

- Formation of hybrid electronic states

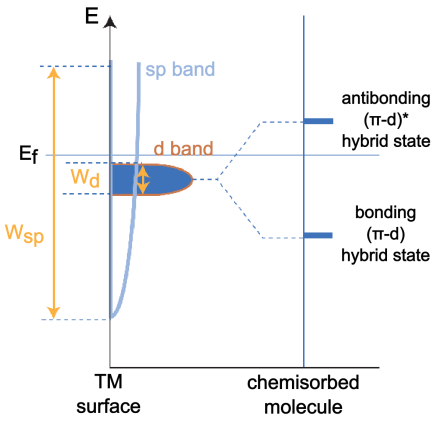

Cinchetti M. et al., Nat. Mater. 16, 507-515 (2017)

- Quenching of the magnetic moment

	μ_S (μ_B)	μ_L (μ_B)
Crystal FePc	0.90	0.53
at the interface with Co	0.52	0.04
Au	0.14	0.09

- Thermally stable magnetic coupling

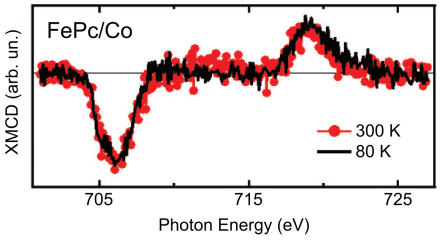

Annese E. et al., Phys. Rev. B 87, 054420 (2013)

Insertion of the graphene spacer

- Intact molecule

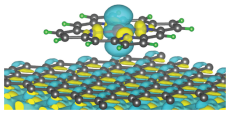

- Preserved molecular orbitals

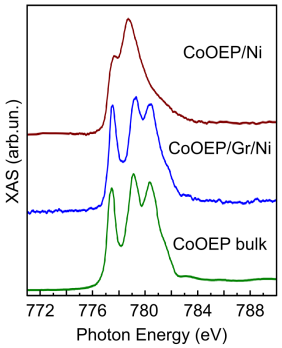

- Preserved magnetic moment

	m_s (μ_B)
CoOEP	~1
at the interface with Gr/Ni	0.87

- No room temperature remanence

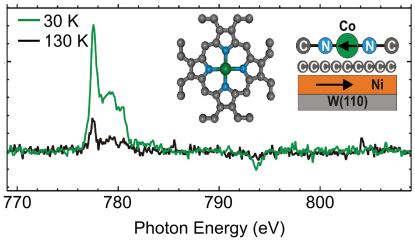

Hermanns C. F. et al., Adv. Mater. 25, 3473-3477 (2013)

- Intact molecule

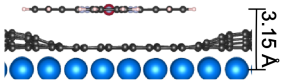

- (Almost) preserved molecular orbitals

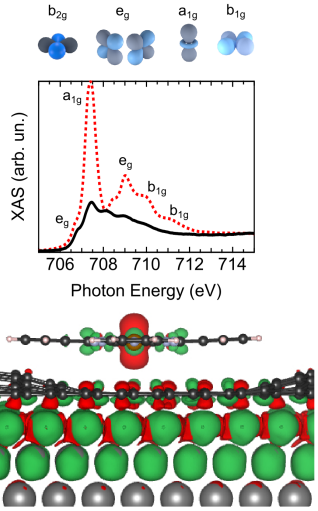

- Preserved magnetic moment

	Fe m (μ_B)
Thick Film FePc	2.20
at the interface with Gr/Co	2.10

- Thermally stable magnetic coupling

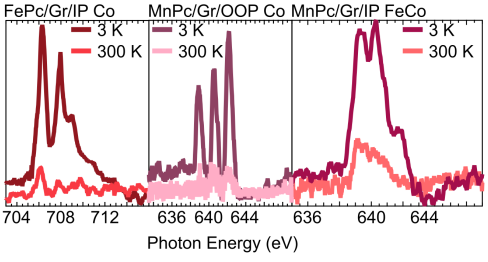

Avvisati G. et al., J. Phys. Chem. C 121, 1639-1647 (2017
Avvisati G. et al., Nano Lett. 18, 2268-2273 (2018)
Avvisati G. et al., Phys. Rev. B 98, 115412 (2018)
Avvisati G. et al., *to be published*

Appendix A

Experimental Techniques

The most suitable techniques to study surface-supported molecular adlayers are electron spectroscopies. Thanks to the small penetration depth of electrons, they are sensitive to the first few Å of the sample and, thanks to the development of brilliant synchrotron radiation sources, this sensitivity is extended to very dilute systems. All the experimental measurements presented in this thesis were performed in Ultra High Vacuum (UHV) conditions, with a base pressure in the 10^{-10} mbar regime or below. For surface physics (and electron spectroscopies) the UHV environment is crucial to efficiently collect electrons as well as maintain sample integrity, since at a pressure of 10^{-6} Torr it takes only 1 second to cover the surface with 1 ML of impurities.

In this chapter we will briefly described the practical aspects of the performed experiments, together with the fundamentals of XPS, NEXAFS and XMCD electron spectroscopies.

A.1 Sample preparation

In this section we will describe the delicate sample preparation procedure, perfected to ensure reproducible high quality standards.

The Ir(111) surface was cleaned with repeated cycles of variable energy sputtering, starting from 2 keV for the just inserted sample and progressively lowering to 1.5 keV for subsequent cycles, and annealing, always above 1300 K to ensure surface ordering. The order of the hexagonal surface was always checked with LEED measurements, revealing the presence of sharp bright diffraction spots without any domain deformation. The cleanliness of the surface was checked, where possible, by XPS measurements, to ensure

the absence of any surface contaminants, e.g. adsorbed oxygen and C segregated from the sample bulk. The quality of the freshly prepared surface was confirmed by the presence of an intense surface contribution to the Ir $4f$ core level.

The Gr sheet was prepared using two different methods, always leading to the same high quality result. The first procedure is a standard Chemical Vapour Deposition (CVD) approach, and the Gr sheet is grown by exposing the sample kept at 1500 K to around 700 L of ethylene (C_2H_4); the second method exploits Temperature Programmed Desorption (TPD), the surface is kept at RT and exposed for 2 minutes to 5×10^{-8}–2×10^{-7} mbar of C_2H_4 and the covered surface is then annealed up to 1300 K, to be repeated up to the completion of the single Gr layer.

Metallic Co was sublimated from a high-purity rod with an home-made e-beam evaporator and deposited on the freshly prepared Gr sheet. Co intercalation was achieved by annealing the Co-covered Gr/Ir(111) surface up to 400–600 K. Successful intercalation was checked with XPS, by monitoring the evolution of the C1s and Ir4f core levels, as well as confirmed by exposing the sample to gaseous oxygen and checking for oxidation features in the XPS/NEXAFS spectrum.

TMPc molecule powder was degassed by warming them just below evaporation temperature for several hours. The purified molecules were then deposited on the sampple by thermal sublimation ($\sim$ 650–800 K), at a constant and reproducible rate of 0.3 Å/ min as determined by a quartz crystal microbalance.

A.2 Interaction of radiation with matter

The experimental results presented in this thesis were obtained by means of electron spectroscopies, namely absorption and photoemission. The choice of electron spectroscopies resides in their marked surface sensitivities, given the small mean free path of electrons in matter. In this section the fundamentals of these techniques are presented, firstly with a general introduction on radiation-matter interaction and then by focusing on the details of the two spectroscopic approaches.

In Fig. A.1 a schematic of the processes is presented. In both cases the probe is an X-ray photon impinging on the sample, being absorbed and exciting a core electron. The difference between absorption and photoemission spectroscopies resides in the final state of the sample: in an absorption process the electron is excited towards an empty or continuum state of the sample, while the photoemitted electron crosses the vacuum level

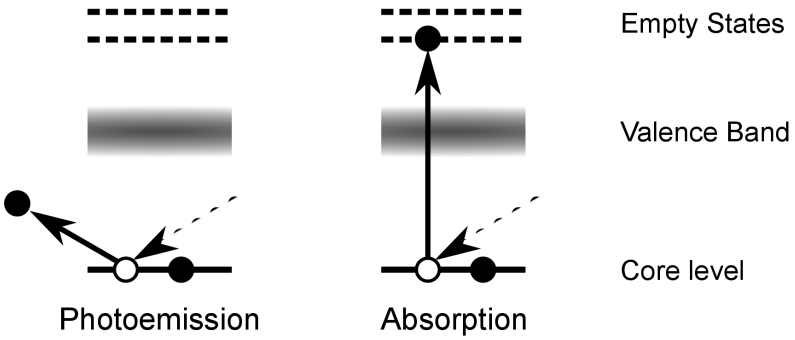

Figure A.1: Schematic of the X-ray absorption (right) and photoemission (left) processes.

and is freed from the surface.

In a semi-classical approach, i.e. the impinging radiation being treated classically while matter is quantized, the interaction Hamiltonian can be written as:

$$\mathcal{H}_{int} = \frac{e}{2mc}(\mathbf{A}\cdot\mathbf{p} - \mathbf{p}\cdot\mathbf{A}) + \frac{e^2}{2mc}\mathbf{A}^2 - e\phi \tag{A.2.1}$$

where $\mathbf{A}$ and ϕ are the vector and scalar potential of the electromagnetic wave, respectively. In the Coulomb gauge ($\phi = 0, \nabla\cdot\mathbf{A} = 0$) and neglecting second order perturbations Eq. A.2.1 becomes:

$$\mathcal{H}_{int} = \frac{e}{mc}\mathbf{A}\cdot\mathbf{p} \tag{A.2.2}$$

In our experiments photon energies in the 100-1000 eV range were used, with an associated wavelength >2 nm. This is larger than typical inter-atomic distances and, accordingly, the spatial variation of the vector potential $\mathbf{A}$ can be neglected. The matrix element of the transition can then be written as:

$$M_{fi} = |\langle\psi_f|\mathbf{A}\cdot\mathbf{p}|\psi_i\rangle| \propto |\langle\psi_f|\mathbf{A}\cdot\nabla V(\mathbf{r})|\psi_i\rangle| \propto |\langle\psi_f|\mathbf{A}\cdot\mathbf{r}|\psi_i\rangle| \tag{A.2.3}$$

where in the last two steps we used the commutation relations $\mathbf{p} \propto [\mathbf{r}, H]$ and $[V(\mathbf{r}), \mathbf{r}] = 0$, with $H = \frac{p^2}{2m} + V(\mathbf{r})$. We can now use the Fermi's Golden Rule to write the transition probability per unit time as

$$\omega \propto \frac{2\pi}{\hbar}|M_{fi}|^2\delta(E_f - E_i - h\nu) \tag{A.2.4}$$

This is a general approach valid for both X-ray absorption and photoemission spec-

troscopies [119], with the differences being hidden by the definition of the electron final state, as will be detailed in the following subsections.

A.2.1 Photoemission Spectroscopy

PhotoEmission Spectroscopy (PES) allows for the investigation of the electronic properties of surfaces. In a PES experiment a photon with given energy $h\nu$ is absorbed and an electron is ejected with kinetic energy

$$E_k = h\nu - E_B - \phi \tag{A.2.5}$$

where E_k is the kinetic energy of the photemitted electrons, E_B is the binding energy of the electrons in the material and ϕ is the work function of the sample. From Eq.A.2.5 we can estimate the binding energy of the hole left in the material.

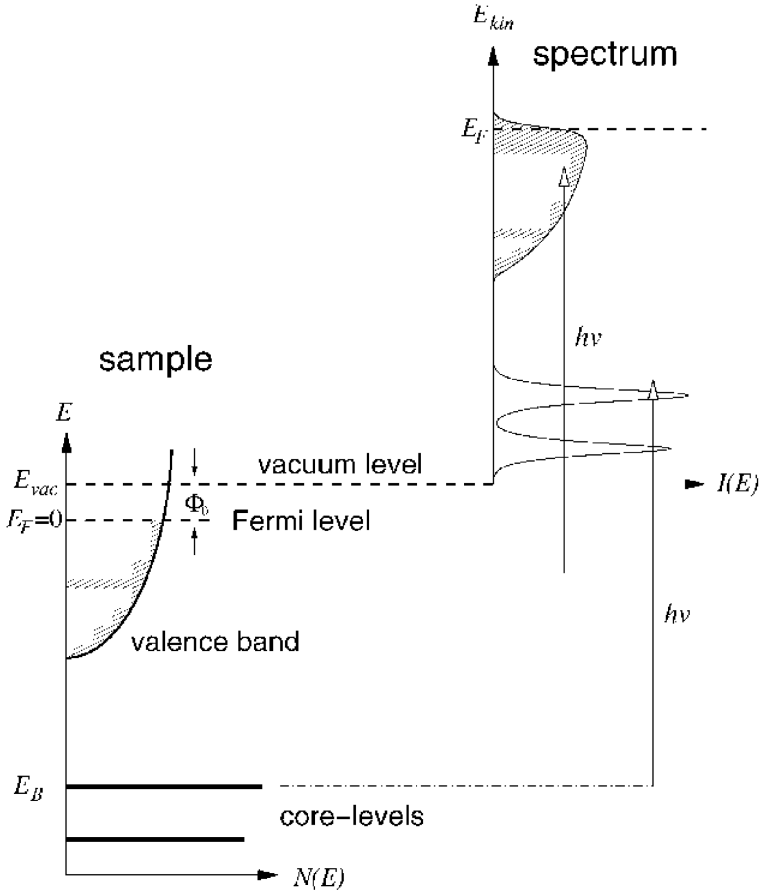

Figure A.2: Simplified sketch of a photoemission process, details in the text. Figure from Ref. [174].

The theory of photoemission spectroscopy is built on the so-called "sudden approximation", in which the system is believed to immediately relax after the formation of the

core/valence hole, and interaction between the system and the photoemitted electron is neglected [119]. In a simplified one-particle approach the photoemission experiments can be depicted as in Fig. A.2. A photon impinges the sample and, depending on its energy, it ejects one electron from the core levels (X-ray) or from the valence band (UV radiation). The photoemitted electrons travels through the materials, eventually crosses the surface and can be revealed, reflecting the electronic eigenstates of the probed sample [119, 174]. In a simplified picture it can be described as the product of three independent processes (*three step model*):

1. photoionization;
2. propagation of the photemitted electron inside the solid;
3. escape from the surface.

Step 1: Photoionization

In order to make the expression in Eq.A.2.4 clearer, we need to make assumptions on the initial and final state wavefunctions for a system with N electrons. In particular, the initial-state wavefunction can be written as the antysimmetrized (C operator) product of the state from which the electron will be photoemitted (Φ_k) and the other N-1 electrons ($\psi_i = C\Phi_{i,k}\psi_{i,k}(N-1)$); while the final-state wavefunction is given by multiplying the wavefunction of the photoemitted electron by the one of the remaining N-1 electrons ($\psi_f = C\Phi_{f,E_k}\psi_{f,k}(N-1)$). Therefore we can write the transition matrix element as

$$\langle\psi_f|\mathbf{r}|\psi_i\rangle = \langle\Phi_{f,E_k}|\mathbf{r}|\Phi_{i,k}\rangle \sum_s c_s \tag{A.2.6}$$

where s is an index running through all the excited states of the system and $c_s = \langle\psi_{f,k,s}(N-1)|\psi_{i,k}(N-1)\rangle$, with $|c_s|^2$ being the probability that the photoemission process leaves the sample in the excited state s. This matrix element contains all the features of a photoemission spectrum: if $s = k$ we have the main line, while other non-zero c_s give rise to the satellite features [119].

Step 2: Propagation inside the solid

Once excited, the photoelectron needs to travel inside the solid and reach the surface. During this path, the electron may collide with the other electrons or with phonons, loosing energy. The average distance that an electron can cover is given by the universal

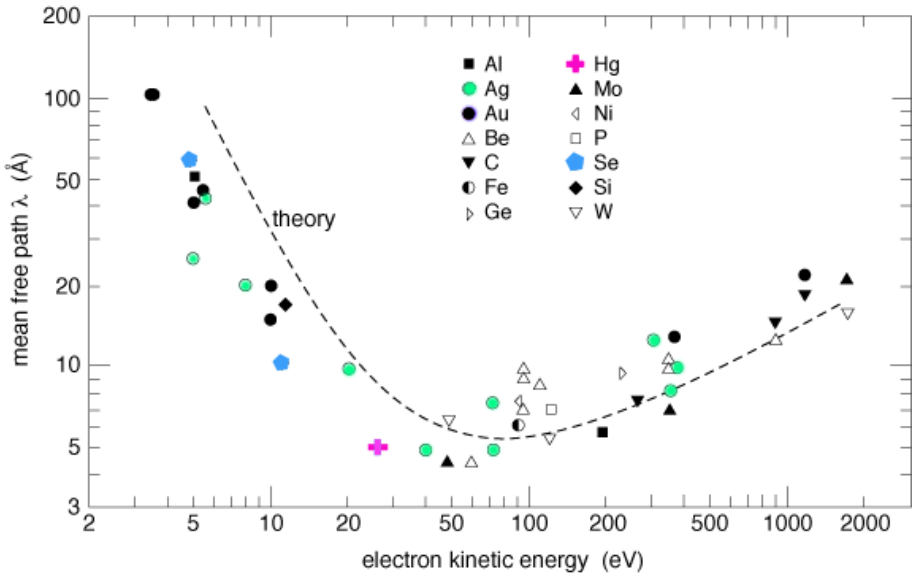

Figure A.3: Electron mean free path as a function of the electron kinetic energy. Image from "Practical Electron Microscopy and Database – An online book" by Yougui Liao.

curve of the inelastic electron mean free path reported in Fig. A.3 and, in the energy range of interest, is less than 1 nm. The inelastic electron mean free path indicates the distance that an electron can travel inside a material before its energy is reduced by a factor e because of inelastic scattering processes. This means that PES is a strictly surface-sensitive technique, with the photoemission intensity decresing at increasing z depth according to

$$I = I_0 e^{-z/(\lambda cos(\theta)} \tag{A.2.7}$$

where I and I_0 are the intensity at z and z=0, respectively, λ is the inelastic mean free path and θ is the angle at which electrons are detected with respect to the surface normal. Eq. A.2.7 can be used to evaluate the thickness of an adlayer, in a layer-by-layer growth approximation, by monitoring the attenuation of the photoemission intensity upon adsorbate deposition.

Step 3: Escape from the surface

Once the photoelectron has reached the surface, it will be able to cross it only if the component perpendicular to the surface of its kinetic energy overcomes the surface potential barrier, otherwise it will be reflected back inside the solid. Furthermore, the parallel component of the the wave vector needs to be conserved upon surface crossing, according to Snell's law. This leads to a maximum angle at which photoelectrons can cross the surface,

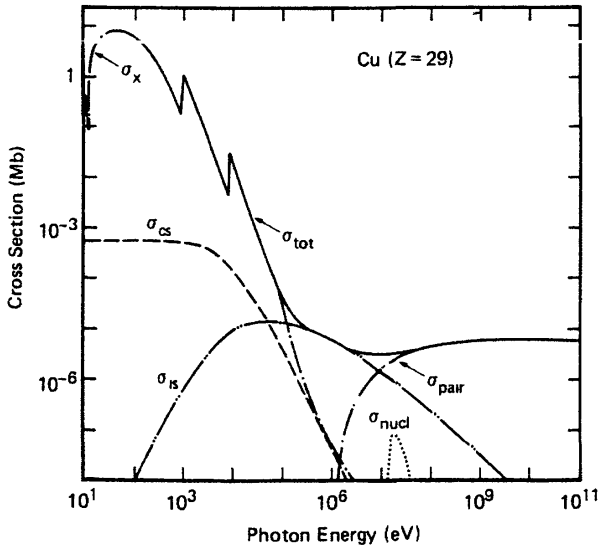

Figure A.4: Absorption cross section as a function of the photon energy for copper. Figure from Ref. [175].

the so-called escape cone.

Core level photoemission spectroscopy is a powerful technique to evaluate the composition of the surface, with sensitivity on the element chemical state. The XPS data presented in this thesis were analysed making use of the Igor pro software, fitting the curves with pseudo-Voigt peaks. The energy scale was calibrated by setting the Fermi(Au $4f_{7/2}$) binding energy at 0(84) eV.

A.2.2 NEXAFS

The final state in a NEXAFS experiment is a bound or continuum state of the system. Accordingly, in Eq.A.2.4 the energy density of final states needs to be taken into account:

$$\omega \propto \frac{2\pi}{\hbar}|M_{fi}|^2\delta(E_f - E_i - h\nu)\rho(E_f) \tag{A.2.8}$$

The absorption cross section varies as a function of the photon energy, as presented for Cu in Fig. A.4: it smoothly decreases for increasing photon energies and exhibits a sudden increase when the binding energy of a core level state is reached (absorption edge). A typical absorption spectrum is presented in Fig. A.5 and can be divided in two energy regions: near the absorption threshold (XANES or NEXAFS) the spectrum is dominated by the main transition lines while, at higher photon energies, the absorption features are associated to multiple scattering processes. The experimental data presented in this thesis

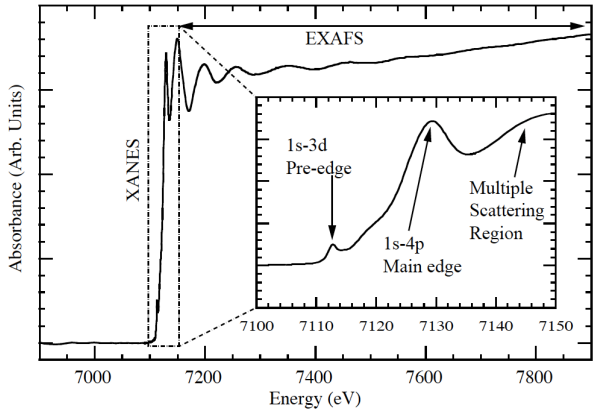

Figure A.5: XAS measurements at the Fe K edge, highlighting the different regions of a typical spectrum. Figure from Carpenter CC BY-SA 3.0 (http://creativecommons.org/licenses/by-sa/3.0).

focus on the first energy region and in the following we will concentrate on this regime.

In Eq.A.2.8 we can notice that the intensity of the signal strictly depends on the magnitude of the matrix element M_{fi}. We can use the explicit expression for the vector potential $\mathbf{A} \sim e^{i\mathbf{k}\cdot\mathbf{r}}\hat{\epsilon}$ and the dipole approximation $e^{i\mathbf{k}\cdot\mathbf{r}} \sim 1$ to write M_{fi} simply as

$$M_{fi} \propto \langle f|\hat{\epsilon}\cdot\mathbf{r}|i\rangle \tag{A.2.9}$$

We can now write the spherical components of $\hat{\epsilon}$

$$\begin{aligned}\epsilon_1 &= -\frac{1}{\sqrt{2}}(\hat{\epsilon}_x + i\hat{\epsilon}_y)\\ \epsilon_0 &= \hat{\epsilon}_z\\ \epsilon_{-1} &= \frac{1}{\sqrt{2}}(\hat{\epsilon}_x - i\hat{\epsilon}_y)\end{aligned} \tag{A.2.10}$$

and of $\mathbf{r}$

$$\begin{aligned}\mathbf{r}_1 &= r\sqrt{\frac{4\pi}{3}}Y_{1,1}(\theta,\phi)\\ \mathbf{r}_0 &= r\sqrt{\frac{4\pi}{3}}Y_{1,0}(\theta,\phi)\\ \mathbf{r}_{-1} &= r\sqrt{\frac{4\pi}{3}}Y_{1,-1}(\theta,\phi)\end{aligned} \tag{A.2.11}$$

so that the scalar product $\hat{\epsilon}\cdot\mathbf{r}$ becomes

$$\sqrt{\frac{4\pi}{3}}\left(\frac{\hat{\epsilon}_x + i\hat{\epsilon}_y}{\sqrt{2}}Y_{1,1}(\theta,\phi) + \hat{\epsilon}_z)Y_{1,0}(\theta,\phi) + \frac{\hat{\epsilon}_x - i\hat{\epsilon}_y}{\sqrt{2}}Y_{1,-1}(\theta,\phi)\right) \tag{A.2.12}$$

If we write the initial and final states in terms of the j and m quantum numbers we can derive the following selection rules, for which the matrix element in Eq.A.2.8 does not vanish [176]

$$\Delta j = 0, \pm 1 \quad \Delta l = \pm 1 \quad \Delta m = \begin{cases} 0, & \text{linear polarization} \\ \pm 1, & \text{circular polarization} \end{cases} \tag{A.2.13}$$

Given a $1s$ initial state, with spherical symmetry, the final state will be a p orbital (K absorption edge). In this case, the matrix element in Eq.A.2.8 will depend on the relative orientation between the incident light polarization vector and the direction of the p orbital as:

$$I \propto Pcos^2(\theta)(cos^2(\alpha) + \frac{1}{2P}tan^2(\theta)sin^2(\alpha)) \tag{A.2.14}$$

where P is the degree of light polarization, α is the tilt angle between the p orbital and the surface normal and θ is the angle between the light polarization vector and the surface normal [120]. Eq.A.2.14 states that the intensity of the signal is maximum when the orbital direction and the polarization vector are collinear. The organic macrocycle of π conjugated molecules is characterized by a well-oriented $\pi(\sigma)$ orbitals arising from the hybridization of the out-of-plane(in-plane) $2p_z(2p_x,2p_y)$ states. Hence, according to Eq.A.2.14, it is possible, by measuring the K edge NEXAFS spectrum at different θ, to determine the adsorbate orientation (α) on the sample surface.

A.2.3 XMCD

XMCD can be treated as a two-step process:

1. in the first step, sketched in Fig. A.6, the circularly polarized radiation impinges the sample and a photon is absorbed. Angular momentum conservation requires that some momentum is exchanged between the incident photon and the excited electron. If the excited electron is found in a spin-orbit-split state (e.g $2p_{3/2}$) the transferred angular momentum is converted into spin via spin-orbit coupling and the photoelectrons get spin-polarized. In particular, the spin polarization will be opposite for positive and negative helicities and at the $2p_{3/2}$ (L_3 edge) and $2p_{1/2}$ (L_2 edge), because of opposite spin-orbit coupling, respectively $l + s$ and $l - s$.

2. in the second step the spin-imbalanced final empty states of the system act as a

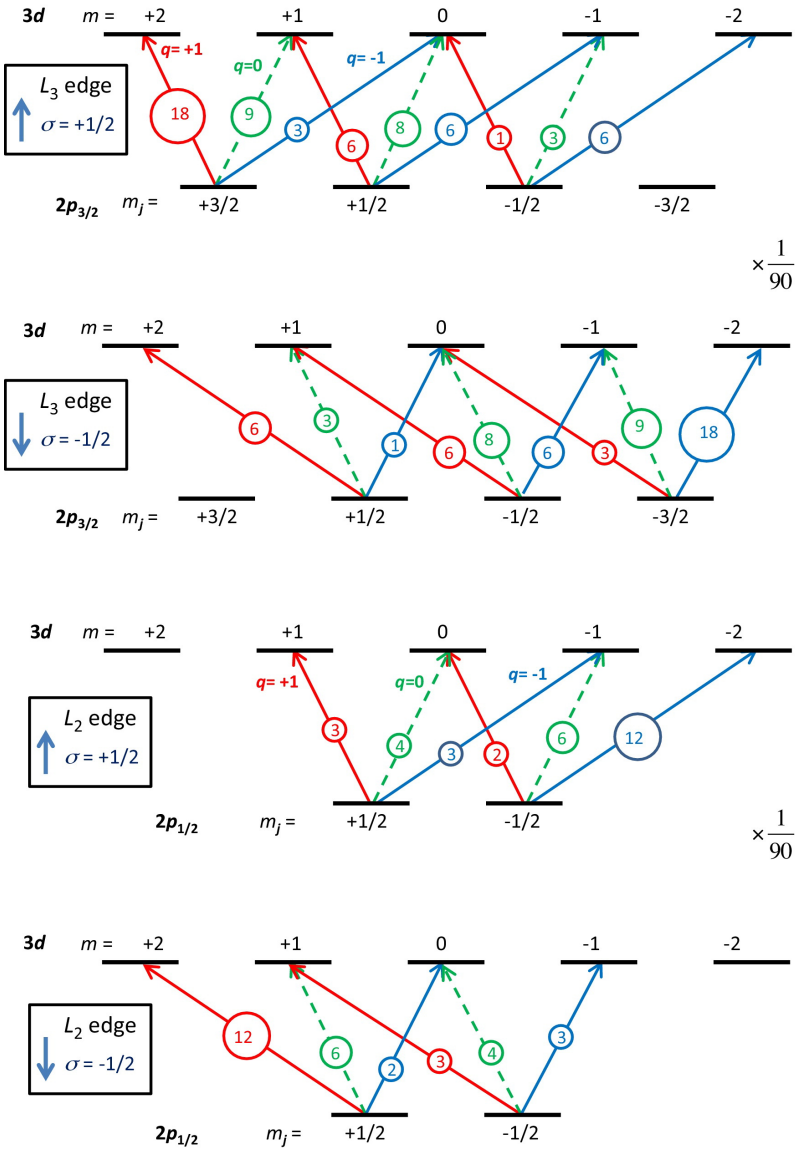

Figure A.6: Dipole-allowed $2p$-$3d$ transitions, excited with left-circular (blue arrows), right-circular (red arrows) and linear (dashed green) polarizations. Figure from Ref. [177].

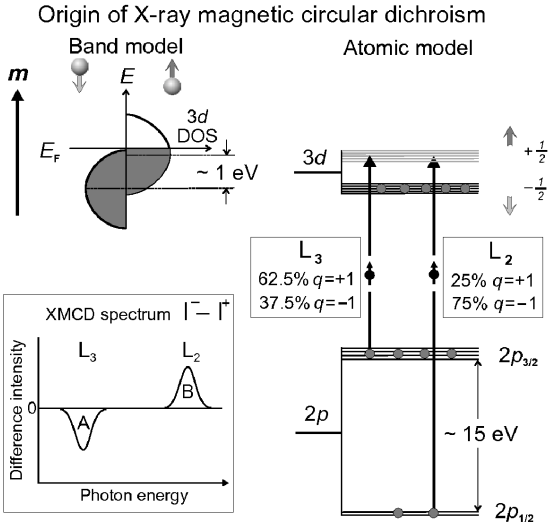

Figure A.7: Illustration of the XMCD absorption at the L edge of transition metals, assuming the X-ray beam impinging parallel to the sample magnetization. Figure from Ref. [178].

spin-sensitive detector, since the dipole operator does not act on spin and hence no spin-flip occurs during the excitation, as reported in Fig. A.7.

If we express the initial and final states in the $|n, l, m_l\rangle$ basis and we make use of the selection rules in Eq.A.2.13, the matrix element of the transitions becomes [178]

$$\begin{aligned}\langle f|\hat{\epsilon}\cdot\mathbf{r}|i\rangle &= \langle l+1, m_l \pm 1|Y_{1,\pm1}|l,m\rangle \\ &= -\sqrt{\frac{(l\pm m_l+2)(l\pm m+1)}{2(2l+3)(2l+1)}}\end{aligned} \tag{A.2.15}$$

and the XMCD spectrum is defined as the difference between parallel and antiparallel orientations of sample magnetization and the incident photon spin. Conventionally, the XMCD signal is defined as $I^{\uparrow\downarrow} - I^{\uparrow\uparrow} = \Delta I$ in such a way that the dichroism at the L_3 edge is negative for the $3d$ transition metals, e.g. Fe, Co, Ni.

One of the main advantages of exploiting XMCD to investigate the magnetic state of the sample is that it enables to quantitatively determine the spin and orbital contribution to the magnetic moment of the system, via the sum rules. The sum rules were derived in Refs. [101] and [102] and relate the integral of the XMCD spectrum to the orbital and

effective spin magnetic moments [177–179]:

$$\begin{aligned} m_L &= -\frac{4}{3} n_h \mu_B \frac{\int_{L_2+L_3} \Delta I(E) dE}{\int_{L_3+L_2} I^+_{L_{2,3}} + I^-_{L_{2,3}}} \\ m_S^{eff} = m_S + 7m_T &= -2 n_h \mu_B \frac{\int_{L_3} \Delta I_{L_3}(E) dE - 2\int_{L_2} \Delta I_{L_2}(E) dE}{\int_{L_3+L_2} I^+_{L_{2,3}} + I^-_{L_{2,3}}} \end{aligned} \tag{A.2.16}$$

The sum rules are a powerful tool, but they have to be used with caution as several approximation needs to be valid [179]. In particular: the beam polarization as well as the sample magnetization needs to be constant over time; the anisotropic magnetic dipole moment m_T needs to be known or extrapolated separately; the L_3 and L_2 edges need to be properly separated, to allow correct integral evaluation as well as background subtraction, and not mixed by multiplet effects. In the experimental data reported in this thesis sum rules application was hindered for the molecular adlayer, because of such effects as well as by not proper saturation of the adsorbate magnetization.

The NEXAFS and XMCD spectra presented in this thesis were acquired in total electron yield, *i.e.*, by measuring the sample drain current. The signal was normalized by the incident flux, as measured from a clean gold grid. Background correction was performed by subtracting the spectrum of the pristine substrate.

NEXAFS measurements were performed at an incident angle of 70° with respect to the surface normal, to enhance surface sensitivity, and changing the light polarization vector, as sketched in the inset of the figures. XMCD spectra were collected by changing the incident angle of the X-ray beam, collinear to the applied magnetic field. Element-sensitive hysteresis loops were acquired by monitoring the field-dependence of the XMCD signal, normalized at the pre-edge to avoid field-induced artifacts.

A.3 Low Energy Electron Diffraction

LEED experiments allow for the investigation of the structural arrangement of the sample surface. Indeed, since diffraction occurs when the incident wavelength is comparable to the spacing of the sample, electrons with energies as low as 20–200 eV range can diffract from the sample surface with typical lattice spacing of few Å. Furthermore, given the inelastic electron mean free path (Fig. A.3) it is clear that the structural information arise from the very surface (< 1 nm deep) of the sample.

In a LEED experiment electrons are produced by a heated filament, monochromatized

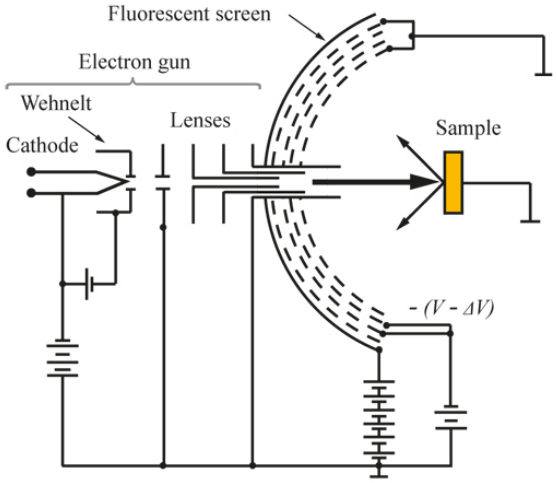

Figure A.8: Schematic of a LEED experiment.

and focused on the sample surface, then elastically diffused electrons are re-collected with a fluorescent screen. The electrons contributing to the actual diffraction pattern are the ones meeting the Von Laue condition:

$$\begin{aligned} \vec{a}_1 \cdot (\vec{k} - \vec{k}_0) &= 2\pi n \\ \vec{a}_2 \cdot (\vec{k} - \vec{k}_0) &= 2\pi m \end{aligned} \tag{A.3.17}$$

if we sum up term to term

$$(\vec{a}_1 + \vec{a}_2) \cdot (\vec{k} - \vec{k}_0) = 2\pi(n+m) \tag{A.3.18}$$

we find that electrons are diffracted if the difference between the outcoming ($\vec{k}$) and incoming ($\vec{k}_0$) waves is an integer (n,m) multiple of the reciprocal lattice vector. The scattered amplitude $A_{\vec{k},\vec{k}_0}$, without including multiple scattering events, will then be given by the coherent sum of single scatterings from each atom at position $\vec{r}_i$, weighted by the atomic scattering factors f_i and including the induced phase:

$$A_{\vec{k},\vec{k}_0} = \sum_{n,m} e^{i(\vec{k}-\vec{k}_0)\cdot(n\vec{a}_1+m\vec{a}_2)} \sum_i f_i e^{i(\vec{k}-\vec{k}_0)\cdot\vec{r}_i} \tag{A.3.19}$$

In particular, electrons undergoing inelastic scattering processes, due to non atomically perfect surfaces, contribute to the diffused background, while electrons meeting the Von Laue conditions that are diffracted by the surface contribute to the LEED pattern, picturing the structure of the reciprocal lattice [180].

Appendix B

Experimental Apparatus

B.1 The LoTUS laboratory

The LoTUS laboratory is located in the physics department of the University of Rome "La Sapienza". It is equipped with two experimental chambers, devoted to core-level and valence-band photoemission experiments. The XPS apparatus consists of a standard PSP TA10 X-ray source, equipped with two anodes, Al and Mg, to select the photon energy that can be either 1486.6 eV (Al K_α) or 1256.6 eV (Mg K_α). The photoemitted electrons are collected by a VG Microtech Cam-2 hemispherical analyzer, with an overall energy resolution of 1 eV. The UHV chamber is also equipped with all the ancillary facilities for sample preparation and control: e-beam heating manipulator, sputter gun, gas lines, CF ports for evaporator mounting and a quartz crystal microbalance for adsorbates coverage control. The setup is also equipped with a load lock chamber allowing for fast insertion of the samples, without breaking the vacuum.

B.2 The SuperESCA beamline

The SuperESCA beamline was the first operating beamline of the italian synchrotron radiation facility, Elettra (Trieste, Italy), and is dedicated to photoemission experiments. It shares, with the ESCA microscopy beamline, a recently installed Kyma linear planar undulator (LPU) insertion device, made by 98 46 mm-long periods and producing horizontally polarized light in the energy range 90 eV – 1500 eV (130 eV – 1800 eV) when the Elettra storage ring works at 2.0 (2.4) GeV.

The optical scheme of the SuperESCA beamline is of the prefocusing-monochromator-

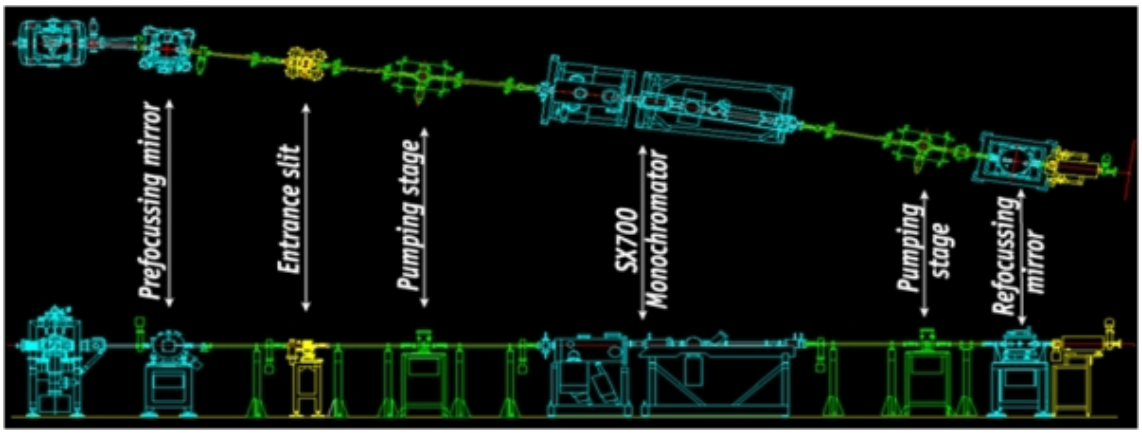

Figure B.1: Optical layout of the SuperESCA beamline.

refocusing type. In particular the beam emitted by the insertion device is pre-focused into the monochromator entrance slit by a vertically-oriented cylindrical mirror and the monochromatized radiation is then refocused on the sample by an ellipsoidal mirror. The SuperESCA monochromator is a modified plane grating SX700 monochromator, with a high resolving power $E/\Delta E$ >10000.

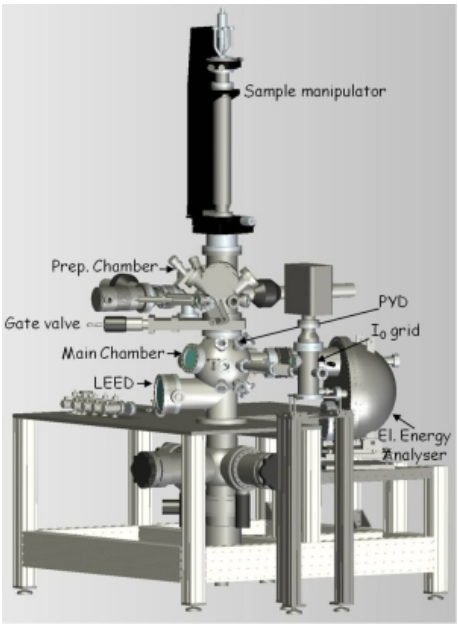

Figure B.2: Picture of the SuperESCA end-station.

The SuperESCA end-station is depicted in Fig. B.2 made up by two UHV chambers, separated by a gate valve. In the top part, sample preparation is performed. The chamber is equipped with a sputter gun, gas lines, and CF ports for user-provided evaporators, while the manipulators allow for high temperature annealing by electron bombardment. The main chamber, the bottom one, is entirely made of μ metal to ensure field shielding. It includes a LEED system and hosts the 150 mm hemispherical electron energy analyser, equipped with a delay line detector designed by the Elettra staff.

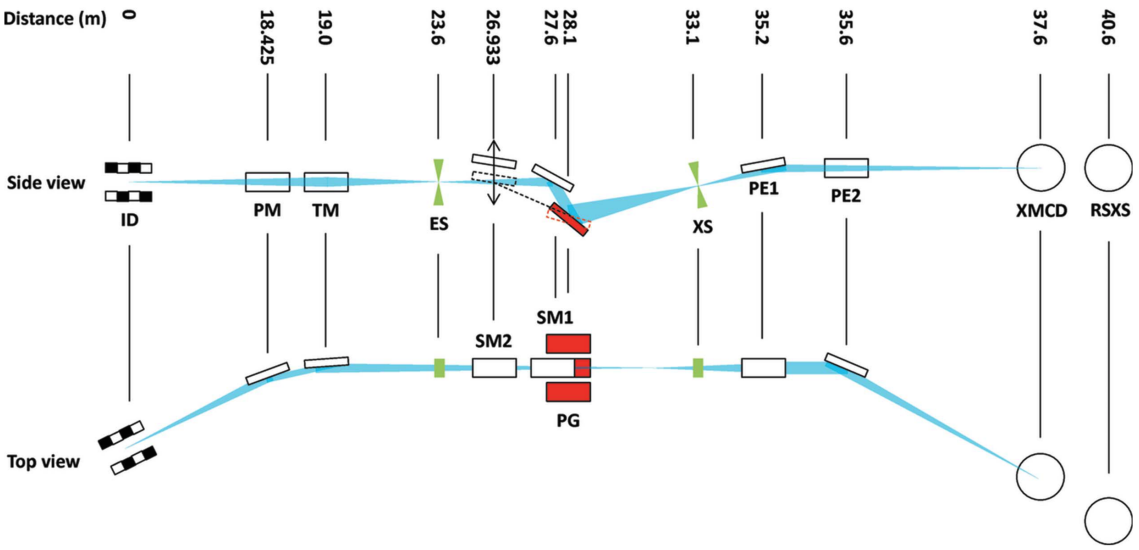

Figure B.3: Optical layout of the BOREAS beamline. Figure from Ref. [181].

B.3 The BOREAS beamline

The BOREAS (Beamline fOr REsonant Absorption and Scattering experiments) is one of the operating beamlines of the ALBA synchrotron radiation facility, located in Barcelona (Spain). It is equipped with two end-stations, the one used for the XMCD-NEXAFS measurements presented in this thesis is called HECTOR (High fiEld veCTOR magnet). The working conditions of the beamline are thoroughly described in Ref. [181].

The BOREAS insertion device is an APPLE-II helical undulator with 22 periods each one 71.36 mm long, able to deliver linearly, circularly and elliptically polarized radiation. The source was designed to reach energies down to 59 eV (78 eV, 98 eV) for horizontally (circularly, vertically) polarized radiation.

The optical layout of the beamline is shown in Fig. B.3. It can be divided in three sections, in particular from left to right:

- white-beam section, with a plane and a toroidal mirrors (PM and TM, respectively). This part is dedicated to absorb most of the beam power to protect the monochromator from thermal drifts (PM) as well as to refocus the beam towards the monochromator entrance (TM);

- monochromator section, with two spherical mirrors (SM), three gratins (PG), to cover the whole 80-4500 eV energy range, and two slits, entrance and exit (ES and XS). The monochromator is of the Hettrick-Underwood type and it was designed in such a way to reach an energy resolving power $E/\Delta E > 5000$;

- refocusing section, with two bendable elliptical mirrors (PE), to focus the beam at the centre of the two end.stations, placed 3 m apart.

Figure B.4: Picture of the HECTOR end-station.

The HECTOR end-station is equipped with a UHV-compatible cryomagnet (Scientific Magnetics Ltd), composed by a set of three orthogonal superconducting split-coils allowing for magnetic fields up to 6 T (2 T) along (perpendicular to) the beam direction. The sample in the main chamber are electrically isolated and in a UHV environment with a base pressure better than 10^{-10} mbar, and placed near to the cold finger of a variable temperature cryostat, covering the range 3 K – 350 K. The preparation chamber is located below the main one and is equipped with all the ancillary facilities for sample preparation: sputter gun, e-beam heating stage, gas lines, metal and organic evaporators.

Ringraziamenti

Questi tre anni carichi di soddisfazione non sarebbero stati possibili senza l'aiuto e la presenza di moltissime persone. Vorrei iniziare ringraziando la Prof.ssa Maria Grazia Betti, per avermi accolto nel suo gruppo di ricerca, avermi insegnato il mestiere della ricercatrice e avermi accompagnato in questo primo tratto di strada. Grazie al prof. Carlo Mariani per i pomeriggi "defaticanti" (secondo lui) in laboratorio.

Grazie a Piggio, grazie a te questa tesi ha molto più senso. Grazia a "L'Ingegnere", i beamtime con te erano un po' meno duri. Grazie ai miei "compagni di LoTUS", la veterana Iolanda *in primis* perché "a smooth sea never made a skilled sailor", e i nostri laureandi compagni di molte, moltissime serate Giulio, Marco e Filippo. Grazie ad Alessandra, per le infinite sedute di mutuo ascolto. Grazie a "la saletta e i suoi abitanti" per aver alleggerito le giornate più stressanti.

Grazie ad Andrea, Claudia e Daniele, il loro supporto (teorico e non) ha dato un altro peso alle nostre misure. Grazie a Manuel (BOREAS – Alba), Silvano, Paolo, Daniel, Luca, Alessandro e Francesco (SuperESCA – Elettra), il loro ottimo lavoro ha permesso di ottenere i risultati mostrati in questa tesi.

Grazie a Niccolò, ai miei amici e alla mia famiglia, grazie per esserci sempre stati.

List of Figures

List of Tables

Acronyms

AFM Antiferromagnetic.

CuPc Copper-Phthalocyanine.

CVD Chemical Vapour Deposition.

DFT Density Functional Theory.

FePc Iron-Phthalocyanine.

FM Ferromagnetic.

GI Grazing Incidence.

Gr Graphene.

IP In-Plane.

LDA Local Density Approximation.

LEED Low-Energy Electron Diffraction.

LUMO Lowest Unoccupied Molecular Orbital.

MAE Magnetic Anisotropy Energy.

MnPc Manganese-Phthalocyanine.

NEXAFS Near Edge X-ray Absorption Fine Structure.

NI Normal Incidence.

OOP Out-Of-Plane.

PMA Perpendicular Magnetic Anisotropy.

RT Room Temperature.

TMPc Transition Metal Phthalocyanine.

TPD Temperature Programmed Desorption.

UHV Ultra High Vacuum.

XAS X-ray Absorption Spectroscopy.

XMCD X-ray Magnetic Circular Dichroism.

XPS X-ray Photoemission Spectroscopy.

Bibliography

[1] A. Fert. 'Nobel Lecture: Origin, development, and future of spintronics'. *Reviews of Modern Physics*, **80**:1517–1530, 2008.

[2] S. A. Wolf, D. D. Awschalom, R. A. Buhrman, J. M. Daughton, S. von Molnár, M. L. Roukes, A. Y. Chtchelkanova, and D. M. Treger. 'Spintronics: a spin-based electronics vision for the future'. *Science*, **294**:1488–1495, 2001.

[3] H. Brune and P. Gambardella. *Atomic and molecular magnets on surfaces*, pages 447–470. CRC Press, 2013.

[4] C. Carbone, S. Gardonio, P. Moras, S. Lounis, M. Heide, G. Bihlmayer, N. Atodiresei, P. H. Dederichs, S. Blügel, S. Vlaic, A. Lehnert, S. Ouazi, S. Rusponi, H. Brune, J. Honolka, A. Enders, K. Kern, S. Stepanow, C. Krull, T. Balashov, A. Mugarza, and P. Gambardella. 'Self-assembled nanometer-scale magnetic networks on surfaces: fundamental interactions and functional properties'. *Advanced Functional Materials*, **21**:1212–1228, 2011.

[5] P. Gambardella, S. Rusponi, M. Veronese, S. S. Dhesi, C. Grazioli, A. Dallmeyer, I. Cabria, R. Zeller, P. H. Dederichs, K. Kern, C. Carbone, and H. Brune. 'Giant magnetic anisotropy of single cobalt atoms and nanoparticles'. *Science*, **300**:1130–1133, 2003.

[6] J. Li, W.-D. Schneider, R. Berndt, and B. Delley. 'Kondo scattering observed at a single magnetic impurity'. *Physical Review Letters*, **80**:2893–2896, 1998.

[7] D. M. Eigler and E. K. Schweizer. 'Positioning single atoms with a scanning tunnelling microscope'. *Nature*, **344**:524–526, 1990.

[8] Harald Brune. *Growth of metal clusters at surfaces*, pages 67–105. Springer Berlin Heidelberg, Berlin, Heidelberg, 2000.

[9] A. Singha, R. Baltic, F. Donati, C. Wäckerlin, J. Dreiser, L. Persichetti, S. Stepanow, P. Gambardella, S. Rusponi, and H. Brune. '$4f$ occupancy and magnetism of rare-earth atoms adsorbed on metal substrates'. *Physical Review B*, **96**:224418, 2017.

[10] F. Donati, A. Singha, S. Stepanow, C. Wäckerlin, J. Dreiser, P. Gambardella, S. Rusponi, and H. Brune. 'Magnetism of Ho and Er atoms on close-packed metal surfaces'. *Physical Review Letter*, **113**:237201, 2014.

[11] F. Donati, S. Rusponi, S. Stepanow, C. Wäckerlin, A. Singha, L. Persichetti, R. Baltic, K. Diller, F. Patthey, E. Fernandes, J. Dreiser, Ž. Šljivančanin, K. Kummer, C. Nistor, P. Gambardella, and H. Brune. 'Magnetic remanence in single atoms'. *Science*, **352**:318–321, 2016.

[12] F. D. Natterer, F. Donati, F. Patthey, and H. Brune. 'Thermal and magnetic-field stability of Holmium single-atom magnets'. *Physical Review Letter*, **121**:027201, 2018.

[13] Johannes V. Barth. 'Molecular architectonic on metal surfaces'. *Annual Review of Physical Chemistry*, **58**:375–407, 2007.

[14] E. Goiri, P. Borghetti, A. El-Sayed, J. E. Ortega, and D. G. de Oteyza. 'Multi-component organic layers on metal substrates'. *Advanced Materials*, **28**:1340–1368, 2016.

[15] T. W. White, N. Martsinovich, A. Troisi, and G. Costantini. 'Quantifying the "subtle interplay" between intermolecular and moleculesubstrate interactions in molecular assembly on surfaces'. *The Journal of Physical Chemistry C*, **122**:17954–17962, 2018.

[16] P. Gambardella, S. Stepanow, A. Dmitriev, J. Honolka, F. M. F. de Groot, M. Lingenfelder, S. S. Gupta, D. D. Sarma, P. Bencok, S. Stanescu, S. Clair, S. Pons, N. Lin, A. P. Seitsonen, H. Brune, J. V. Barth, and K. Kern. 'Supramolecular control of the magnetic anisotropy in two-dimensional high-spin Fe arrays at a metal interface'. *Nature Materials*, **8**:189–193, 2009.

[17] M. I. Dyakonov. *Spin physics in semiconductors*. Springer-Verlag Berlin Heidelberg, 2008.

[18] J. Bartolomé, C. Monton, and I. K. Schuller. *Magnetism of Metal Phthalocyanines*, pages 221–245. Springer Berlin Heidelberg, 2014.

[19] L. Bogani and W. Wernsdorfer. 'Molecular spintronics using single-molecule magnets'. *Nature Materials*, **7**:179–186, 2008.

[20] C. Wäckerlin, F. Donati, A. Singha, R. Baltic, S. Rusponi, K. Diller, F. Patthey, M. Pivetta, Y. Lan, S. Klyatskaya, M. Ruben, H. Brune, and J. Dreiser. 'Giant hysteresis of single-molecule magnets adsorbed on a nonmagnetic insulator'. *Advanced Materials*, **28**:5195–5199, 2016.

[21] D. Cahen, A. Kahn, and E. Umbach. 'Energetics of molecular interfaces'. *Materials Today*, **8**:32–41, 2005.

[22] M. Cinchetti, V. A. Dediu, and L. E. Hueso. 'Activating the molecular spinterface'. *Nature Materials*, **16**:507–515, 2017.

[23] A. Brambilla, A. Picone, D. Giannotti, A. Calloni, G. Berti, G. Bussetti, S. Achilli, G. Fratesi, M. I. Trioni, G. Vinai, P. Torelli, G. Panaccione, L. Duò, M. Finazzi, and F. Ciccacci. 'Enhanced magnetic hybridization of a spinterface through insertion of a two-dimensional magnetic oxide layer'. *Nano Letters*, **17**:7440–7446, 2017.

[24] Y.-H. Chu, C.-H. Hsu, C.-I. Lu, H.-H. Yang, T.-H. Yang, C.-H. Luo, K.-J. Yang, S.-H. Hsu, G. Hoffmann, C.-C. Kaun, and M.-T. Lin. 'Spin-dependent molecule symmetry at a pentaceneCo spinterface'. *ACS Nano*, **9**:7027–7032, 2015.

[25] C. Barraud, P. Seneor, R. Mattana, S. Fusil, K. Bouzehouane, C. Deranlot, P. Graziosi, L. Hueso, I. Bergenti, V. Dediu, F. Petroff, and A. Fert. 'Unravelling the role of the interface for spin injection into organic semiconductors'. *Nature Physics*, **6**:615–620, 2010.

[26] J. Brede, N. Atodiresei, S. Kuck, P. Lazić, V. Caciuc, Y.a Morikawa, G. Hoffmann, S. Blügel, and R. Wiesendanger. 'Spin- and energy-dependent tunneling through a single molecule with intramolecular spatial resolution'. *Physical Review Letters*, **105**:047204, 2010.

[27] E. Annese, F. Casolari, J. Fujii, and G. Rossi. 'Interface magnetic coupling of Fe-phthalocyanine layers on a ferromagnetic surface'. *Physical Review B*, **87**:054420, 2013.

[28] K.-J. Baeg, M. Binda, D. Natali, M. Caironi, and Y.-Y. Noh. 'Organic light detectors: photodiodes and phototransistors'. *Advanced Materials*, **25**:4267–4295, 2013.

[29] S. Fu, K. Zhang, M. Zhhang, and L. Tian. 'Encapsulated phthalocyanine blue pigment with polymerisable dispersant for inkjet printing inks'. *Pigment & Resin Technology*, **41**:3–8, 2012.

[30] S. Schmaus, A. Bagrets, Y. Nahas, A. Yamada, T. K. andBork, M. Bowen, E. Beaurepaire, F. Evers, and W. Wulfhekel. 'Giant magnetoresistance through a single molecule'. *Nature Nanotechnology*, **6**:185–189, 2011.

[31] P. Gargiani, M. Angelucci, C. Mariani, and M. G. Betti. 'Metal-phthalocyanine chains on the Au(110) surface: Interaction states versus *d*-metal states occupancy'. *Physical Review B*, **81**:085412, 2010.

[32] C. Barraud, K. Bouzehouane, C. Deranlot, D. J. Kim, R. Rakshit, S. Shi, J. Arabski, M. Bowen, E. Beaurepaire, S. Boukari, F. Petroff, P. Seneor, and R. Mattana. 'Phthalocyanine based molecular spintronic devices'. *Dalton Transactions*, **45**:16694–16699, 2016.

[33] A. Lodi Rizzini, C. Krull, A. Mugarza, T. Balashov, C. Nistor, R. Piquerel, S. Klyatskaya, M. Ruben, P. M. Sheverdyaeva, P. Moras, C. Carbone, C. Stamm, P. S. Miedema, P. K. Thakur, V. Sessi, M. Soares, F. Yakhou-Harris, J. C. Cezar, S. Stepanow, and P. Gambardella. 'Coupling of single, double, and triple-decker metal-phthalocyanine complexes to ferromagnetic and antiferromagnetic substrates'. *Surface Science*, **630**:361–374, 2014.

[34] C. Iacovita, M. V. Rastei, B. W. Heinrich, T. Brumme, J. Kortus, L. Limot, and J. P. Bucher. 'Visualizing the spin of individual cobalt-phthalocyanine molecules'. *Physical Review Letters*, **101**:116602, 2008.

[35] J. Fernández, P. Roura-Bas, A. Camjayi, and A. A. Aligia. 'Two-stage three-channel Kondo physics for an FePc molecule on the Au(111) surface'. *Journal of Physics: Condensed Matter*, **30**:374003, 2018.

[36] K. S. Novoselov, A. K. Geim, S. V. Morozov, D. Jiang, Y. Zhang, S. V. Dubonos, I. V. Grigorieva, and A. A. Firsov. 'Electric field effect in atomically thin carbon films'. *Science*, **306**:666–669, 2004.

[37] V. M. Karpan, G. Giovannetti, P. A. Khomyakov, M. Talanana, A. A. Starikov, M. Zwierzycki, J. van den Brink, G. Brocks, and P. J. Kelly. 'Graphite and graphene as perfect spin filters'. *Physical Review Letters*, **99**:176602, 2007.

[38] N. Tombros, C. Jozsa, M. Popinciuc, H. T. Jonkman, and B. J. van Wees. 'Electronic spin transport and spin precession in single graphene layers at room temperature'. *Nature*, **448**:571–574, 2007.

[39] M. Scardamaglia, S. Lisi, S. Lizzit, A. Baraldi, R. Larciprete, C. Mariani, and M. G. Betti. 'Graphene-induced substrate decoupling and ideal doping of a self-assembled iron-phthalocyanine single layer'. *Journal of Physical Chemistry C*, **117**:3019–3027, 2013.

[40] F. Mittendorfer, A. Garhofer, J. Redinger, J. Klimeš, J. Harl, and G. Kresse. 'Graphene on Ni(111): strong interaction and weak adsorption'. *Physical Review B*, **84**:201401, 2011.

[41] A. Barla, V. Bellini, S. Rusponi, P. Ferriani, M. Pivetta, F. Donati, F. Patthey, L. Persichetti, D. K. Mahatha, M. Papagno, C. Piamonteze, S. Fichtner, S. Heinze, P. Gambardella, H. Brune, and C. Carbone. 'Complex magnetic exchange coupling between Co nanostructures and Ni(111) across epitaxial graphene'. *ACS Nano*, **10**:1101–1107, 2016.

[42] S. Marocchi, P. Ferriani, N. M. Caffrey, F. Manghi, S. Heinze, and V. Bellini. 'Graphene-mediated exchange coupling between a molecular spin and magnetic substrates'. *Physical Review B*, **88**:144407, 2013.

[43] D. Klar, S. Bhandary, A. Candini, L. Joly, P. Ohresser, S. Klyatskaya, M. Schleberger, M. Ruben, M. Affronte, O. Eriksson, B. Sanyal, and H. Wende. 'Field-regulated switching of the magnetization of Co-porphyrin on graphene'. *Physical Review B*, **89**:144411, 2014.

[44] C. F. Hermanns, K. Tarafder, M. Bernien, A. Krüger, Y.-M. Chan, P. M. Oppeneer, and W. Kuch. 'Magnetic coupling of porphyrin molecules through graphene'. *Advanced Materials*, **25**:3473–3477, 2013.

[45] S. Bhandary, O. Eriksson, and B. Sanyal. 'Defect controlled magnetism in FeP/graphene/Ni(111)'. *Scientific Reports*, **3**:3405, 2013.

[46] A. Candini, V. Bellini, D. Klar, V. Corradini, R. Biagi, V. De Renzi, K. Kummer, N. B. Brookes, U. del Pennino, H. Wende, and M. Affronte. 'Ferromagnetic exchange coupling between Fe phthalocyanine and Ni(111) surface mediated by the extended states of graphene'. *Journal of Physical Chemistry C*, **118**:17670–17676, 2014.

[47] P. Gargiani, S. Lisi, G. Avvisati, P. Mondelli, S. Fatale, and M. G. Betti. 'Mixing of MnPc electronic states at the MnPc/Au(110) interface'. *The Journal of Chemical Physics*, **147**:134702, 2017.

[48] P. Gargiani, G. Rossi, R. Biagi, V. Corradini, M. Pedio, S. Fortuna, A. Calzolari, S. Fabris, J. C. Cezar, N. B. Brookes, and M. G. Betti. 'Spin and orbital configuration of metal phthalocyanine chains assembled on the Au(110) surface'. *Physical Review B*, **87**:165407, 2013.

[49] M. Scardamaglia, C. Struzzi, S. Lizzit, M. Dalmiglio, P. Lacovig, A. Baraldi, C. Mariani, and M. G. Betti. 'Energetics and hierarchical interactions of metalphthalocyanines adsorbed on graphene/Ir(111)'. *Langmuir*, **29**:10440–10447, 2013.

[50] J. Coraux, A. T. NDiaye, N. Rougemaille, C. Vo-Van, A. Kimouche, H.-X. Yang, M. Chshiev, N. Bendiab, O. Fruchart, and A. K. Schmid. 'Air-protected epitaxial graphene/ferromagnet hybrids prepared by chemical vapor deposition and intercalation'. *Journal of Physical Chemistry Letters*, **3**:2059–2063, 2012.

[51] I. Carlomagno, J. Drnec, A. M. Scaparro, S. Cicia, S. Mobilio, R. Felici, and C. Meneghini. 'Effectiveness of Co intercalation between Graphene and Ir(1 1 1)'. *Chemical Physics Letters*, **697**:7–11, 2018.

[52] R. S. Weatherup, L. D'Arsié, A. Cabrero-Vilatela, S. Caneva, R. Blume, J. Robertson, R. Schloegl, and S. Hofmann. 'Long-term passivation of strongly interacting metals with single-layer graphene'. *Journal of the American Chemical Society*, **137**:14358–14366, 2015.

[53] I. Palacio, G. Otero-Irurueta, C. Alonso, J. I. Martnez, E. Lpez-Elvira, I. Muoz-Ochando, H. J. Salavagione, M. F. Lpez, M. Garca-Hernndez, J. Mndez, G. J. Ellis, and J. A. Martn-Gago. 'Chemistry below graphene: decoupling epitaxial graphene from metals by potential-controlled electrochemical oxidation'. *Carbon*, **129**:837–846, 2018.

[54] C. Romero-Muiz, A. Martn-Recio, P. Pou, J.M. Gmez-Rodrguez, and R. Prez. 'Strong dependence of flattening and decoupling of graphene on metals on the local distribution of intercalated oxygen atoms'. *Carbon*, **101**:129–134, 2016.

[55] S. Schumacher, T. O. Wehling, P. Lazić, S. Runte, D. F. Förster, C. Busse, M. Petrović, M. Kralj, S. Blügel, N. Atodiresei, V. Caciuc, and T. Michely. 'The backside of graphene: manipulating adsorption by intercalation'. *Nano Letters*, **13**:5013–5019, 2013.

[56] M. Andersen, L. Hornekær, and B. Hammer. 'Understanding intercalation structures formed under graphene on Ir(111)'. *Physical Review B*, **90**:155428, 2014.

[57] F. Huttmann, A. J. Martínez-Galera, V. Caciuc, N. Atodiresei, S. Schumacher, S. Standop, I. Hamada, T. O. Wehling, S. Blügel, and T. Michely. 'Tuning the van der Waals interaction of graphene with molecules via doping'. *Physical Review Letters*, **115**:236101, 2015.

[58] S. Lisi, P. Gargiani, M. Scardamaglia, N. B. Brookes, V. Sessi, C. Mariani, and M. G. Betti. 'Graphene-induced magnetic anisotropy of a two-dimensional iron phthalocyanine network'. *Journal of Physical Chemistry Letters*, **6**:1690–1695, 2015.

[59] F. Donati, Q. Dubout, G. Autès, F. Patthey, F. Calleja, P. Gambardella, O. V. Yazyev, and H. Brune. 'Magnetic moment and anisotropy of individual Co atoms on graphene'. *Physical Review Letters*, **111**:236801, 2013.

[60] F. Donati, L. Gragnaniello, A. Cavallin, F. D. Natterer, Q. Dubout, M. Pivetta, F. Patthey, J. Dreiser, C. Piamonteze, S. Rusponi, and H. Brune. 'Tailoring the magnetism of Co atoms on graphene through substrate hybridization'. *Physical Review Letters*, **113**:177201, 2014.

[61] A. T. N'Diaye, J. Coraux, T. N. Plasa, C. Busse, and T. Michely. 'Structure of epitaxial graphene on Ir(111)'. *New Journal of Physics*, **10**:043033, 2008.

[62] N. Blanc, J. Coraux, C. Vo-Van, A. T. N'Diaye, O. Geaymond, and G. Renaud. 'Local deformations and incommensurability of high-quality epitaxial graphene on a weakly interacting transition metal'. *Physical Review B*, **86**:235439, 2012.

[63] C. Busse, P. Lazić, R. Djemour, J. Coraux, T. Gerber, N. Atodiresei, V. Caciuc, R. Brako, A. T. N'Diaye, S. Blügel, J. Zegenhagen, and T. Michely. 'Graphene

on Ir(111): physisorption with chemical modulation'. *Physical Review Letters*, **107**:036101, 2011.

[64] A. B. Preobrajenski, May Ling Ng, A. S. Vinogradov, and N. Mårtensson. 'Controlling graphene corrugation on lattice-mismatched substrates'. *Physical Review B*, **78**:073401, 2008.

[65] S. Vlaic, N. Rougemaille, A. Kimouche, B. S. Burgos, A. Locatelli, and J. Coraux. 'Intercalating cobalt between graphene and iridium (111): spatially dependent kinetics from the edges'. *Physical Review Materials*, **1**:053406, 2017.

[66] M. Sicot, P. Leicht, A. Zusan, S. Bouvron, O. Zander, M. Weser, Y. S. Dedkov, K. Horn, and M. Fonin. 'Size-selected epitaxial nanoislands underneath graphene moiré on Rh(111)'. *ACS Nano*, **6**:151–158, 2012.

[67] S. Vlaic, A. Kimouche, J. Coraux, B. Santos, A. Locatelli, and N. Rougemaille. 'Cobalt intercalation at the graphene/iridium(111) interface: Influence of rotational domains, wrinkles, and atomic steps'. *Applied Physics Letters*, **104**:101602, 2014.

[68] L. Huang, Y. Pan, L. Pan, M. Gao, W. Xu, Y. Que, H. Zhou, Y. Wang, S. Du, and H.-J. Gao. 'Intercalation of metal islands and films at the interface of epitaxially grown graphene and Ru(0001) surfaces'. *Applied Physics Letters*, **99**:163107, 2011.

[69] I. Carlomagno, J. Drnec, A. M. Scaparro, S. Cicia, S. Vlaic, R. Felici, and C. Meneghini. 'Co-Ir interface alloying induced by thermal annealing'. *Journal of Applied Physics*, **120**:195302, 2016.

[70] D. Pacilé, S. Lisi, I. Di Bernardo, M. Papagno, L. Ferrari, M. Pisarra, M. Caputo, S. K. Mahatha, P. M. Sheverdyaeva, P. Moras, P. Lacovig, S. Lizzit, A. Baraldi, M. G. Betti, and C. Carbone. 'Electronic structure of graphene/Co interfaces'. *Physical Review B*, **90**:195446, 2014.

[71] H. Vita, St. Böttcher, P. Leicht, K. Horn, A. B. Shick, and F. Máca. 'Electronic structure and magnetic properties of cobalt intercalated in graphene on Ir(111)'. *Physical Review B*, **90**:165432, 2014.

[72] R. Decker, J. Brede, N. Atodiresei, V. Caciuc, S. Blügel, and R. Wiesendanger. 'Atomic-scale magnetism of cobalt-intercalated graphene'. *Physical Review B (R)*, **87**:041403, 2013.

[73] I. Carlomagno, J. Drnec, S. Vlaic, N. Vinogadrov, F. Carlà, H. Isern, C. Meneghini, and R. Felici. 'Co film stretching induced by lattice mismatch and annealing: the role of graphene'. *Applied Surface Science*, **432**:22–26, 2018.

[74] G. Avvisati, S. Lisi, P. Gargiani, A. Della Pia, O. De Luca, D. Pacilé, C. Cardoso, D. Varsano, D. Prezzi, A. Ferretti, and M. G. Betti. 'FePc adsorption on the moiré superstructure of graphene intercalated with a cobalt layer'. *Journal of Physical Chemistry C*, **121**:1639–1647, 2017.

[75] D. Yu. Usachov, A. V. Fedorov, O. Yu. Vilkov, A. E. Petukhov, A. G. Rybkin, A. Ernst, M. M. Otrokov, E. V. Chulkov, I. I. Ogorodnikov, M. V. Kuznetsov, L. V. Yashina, E. Yu. Kataev, A. V. Erofeevskaya, V. Yu. Voroshnin, V. K. Adamchuk, C. Laubschat, and D. V. Vyalikh. 'Large-scale sublattice asymmetry in pure and boron-doped graphene'. *Nano Letters*, **16**:4535–4543, 2016.

[76] G. Avvisati, C. Cardoso, D. Varsano, A. Ferretti, P. Gargiani, and M. G. Betti. 'Ferromagnetic and antiferromagnetic coupling of spin molecular interfaces with high thermal stability'. *Nano Letters*, **18**:2268–2273, 2018.

[77] B. Wang, M. Caffio, C. Bromley, H. Früchtl, and R. Schaub. 'Coupling epitaxy, chemical bonding, and work function at the local scale in transition metal-supported graphene'. *ACS Nano*, **4**:5773–5782, 2010.

[78] Q. Dubout, F. Calleja, G. Sclauzero, M. Etzkorn, A. Lehnert, L. Claude, M. Papagno, F. D. Natterer, F. Patthey, S. Rusponi, A. Pasquarello, and H. Brune. 'Giant apparent lattice distortions in STM images of corrugated sp^2-hybridised monolayers'. *New Journal of Physics*, 18:103027, 2016.

[79] A. T. N'Diaye, S. Bleikamp, P. J. Feibelman, and T. Michely. 'Two-dimensional Ir cluster lattice on a graphene moiré on Ir(111)'. *Physical Review Letters*, **97**:215501, 2006.

[80] A. T. N'Diaye, T. Gerber, C. Busse, J. Mysliveček, J. Coraux, and T. Michely. 'A versatile fabrication method for cluster superlattices'. *Physical Review Letters*, **97**:215501, 2006.

[81] H. G. Zhang, J. T. Sun, T. Low, L. Z. Zhang, Y. Pan, Q. Liu, J. H. Mao, H. T. Zhou, H. M. Guo, S. X. Du, F. Guinea, and H.-J. Gao. 'Assembly of iron phthalocyanine

and pentacene molecules on a graphene monolayer grown on Ru(0001)'. *Physical Review B*, **84**:245436, 2011.

[82] J. Mao, H. Zhang, Y. Jiang, Y. Pan, M. Gao, W. Xiao, and H.-J. Gao. 'Tunability of supramolecular Kagome lattices of magnetic phthalocyanines using graphene-based moiré patterns as templates'. *Journal of the American Chemical Society*, **131**:14136–14137, 2009.

[83] H. Yang, A. D. Vu, A. Hallal, N. Rougemaille, J. Coraux, G. Chen, A. K. Schmid, and M. Chshiev. 'Anatomy and giant enhancement of the perpendicular magnetic anisotropy of cobaltgraphene heterostructures'. *Nano Letters*, **16**:145–151, 2016.

[84] M. Gyamfi, T. Eelbo, M. Waśniowska, and R. Wiesendanger. 'Impact of intercalated cobalt on the electronic properties of graphene on Pt(111)'. *Physical Review B*, **85**:205434, 2012.

[85] N. Rougemaille, A. T. N'Diaye, J. Coraux, C. Vo-Van, O. Fruchart, and A. K. Schmid. 'Perpendicular magnetic anisotropy of cobalt films intercalated under graphene'. *Applied Physics Letters*, **101**:142403, 2012.

[86] A. D. Vu, J. Coraux, G. Chen, A. T. N'Diaye, A. K. Schmid, and N. Rougemaille. 'Unconventional magnetisation texture in graphene/cobalt hybrids'. *Scientific Reports*, **6**:24783, 2016.

[87] H. Yang, G. Chen, A. A. C. Cotta, A. T. N'Diaye, S. A. Nikolaev, E. A. Soares, W. A. A. Macedo, K. Liu, A. K. Schmid, A. Fert, and M. Chshiev. 'Significant DzyaloshinskiiMoriya interaction at grapheneferromagnet interfaces due to the Rashba effect'. *Nature Materials*, **17**:605–609, 2018.

[88] Y. Cao, M. Ahmadzadeh, K. Xu, B. Dodrill, and J. S. McCloy. 'Multiphase magnetic systems: measurement and simulation'. *Journal of Applied Physics*, **123**:023902, 2018.

[89] L. Tauxe, T. A. T. Mullender, and T. Pick. 'Potbellies, waspwaists, and superparamagnetism in magnetic hysteresis'. *Journal of Geophysical Research: Solid Earth*, **101**:571–583, 1996.

[90] L. H. Bennett and E. Della Torre. 'Analysis of wasp-waist hysteresis loops'. *Journal of Applied Physics*, **97**:10E502, 2005.

[91] D. Eom, D. Prezzi, K. T. Rim, H. Zhou, M. Lefenfeld, S. Xiao, C. Nuckolls, M. S. Hybertsen, T. F. Heinz, and G. W. Flynn. 'Structure and electronic properties of graphene nanoislands on Co(0001)'. *Nano Letters*, **9**:2844–2848, 2009.

[92] D. Marchenko, A. Varykhalov, J. Sánchez-Barriga, O. Rader, C. Carbone, and G. Bihlmayer. 'Highly spin-polarized Dirac fermions at the graphene/Co interface'. *Physical Review B*, **91**:235431, 2015.

[93] D. Usachov, A. Fedorov, M. M. Otrokov, A. Chikina, O. Vilkov, A. Petukhov, A. G. Rybkin, Y. M. Koroteev, E. V. Chulkov, V. K. Adamchuk, A. Grüneis, C. Laubschat, and D. V. Vyalikh. 'Observation of single-spin Dirac fermions at the graphene/ferromagnet interface'. *Nano Letters*, **15**:2396–2401, 2015.

[94] A. Díaz-Ortiz, R. Drautz, M. Fähnle, H. Dosch, and J. M. Sanchez. 'Structure and magnetism in bcc-based iron-cobalt alloys'. *Physical Review B*, 73:224208, 2006.

[95] T. Burkert, L. Nordström, O. Eriksson, and O. Heinonen. 'Giant magnetic anisotropy in tetragonal FeCo alloys'. *Physical Review Letters*, **93**:027203, 2004.

[96] F. Yildiz, M. Przybylski, X.-D. Ma, and J. Kirschner. 'Strong perpendicular anisotropy in $Fe_{1-x}Co_x$ alloy films epitaxially grown on mismatching Pd(001), Ir(001), and Rh(001) substrates'. *Physical Review B*, **80**:064415, 2009.

[97] G. Moulas, A. Lehnert, S. Rusponi, J. Zabloudil, C. Etz, S. Ouazi, M. Etzkorn, P. Bencok, P. Gambardella, P. Weinberger, and H. Brune. 'High magnetic moments and anisotropies for Fe_xCo_{1-x} monolayers on Pt(111)'. *Physical Review B*, **78**:214424, 2008.

[98] M. Bazarnik, R. Decker, J. Brede, and R. Wiesendanger. 'Multi-layer and multi-component intercalation at the graphene/Ir(111) interface'. *Surface Science*, **639**:70–74, 2015.

[99] R. Decker, M. Bazarnik, N. Atodiresei, V. Caciuc, S. Blügel, and R. Wiesendanger. 'Local tunnel magnetoresistance of an iron intercalated graphene-based heterostructure'. *Journal of Physics: Condensed Matter*, **26**:394004, 2014.

[100] J. Brede, J. Sławińska, M. Abadia, C. Rogero, J. E. Ortega, I. Piquero-Zulaica, J. Lobo-Checa, A. Arnau, and J. Iribas Cerdá. 'Tuning the graphene on Ir(111) adsorption regime by Fe/Ir surface-alloying'. *2D Materials*, **4**:015016, 2017.

[101] B. T. Thole, P. Carra, F. Sette, and G. van der Laan. 'X-ray circular dichroism as a probe of orbital magnetization'. *Physical Review Letters*, **68**:1943–1946, 1992.

[102] P. Carra, B. T. Thole, M. Altarelli, and X. Wang. 'X-ray circular dichroism and local magnetic fields'. *Physical Review Letters*, **70**:694–697, 1993.

[103] M. Cattelan, I. Píš, S. Nappini, E. Magnano, F. Bondino, and S. Agnoli. 'The magnetization orientation of Fe ultrathin layers in contact with graphene'. *Physical Chemistry Chemical Physics*, **18**:33233–33239, 2016.

[104] R. Salikhov, L. Reichel, B. Zingsem, R. Abrudan, A. Edström, D. Thonig, J. Rusz, O. Eriksson, L. Schultz, S. Fähler, M. Farle, and U. Wiedwald. 'Enhanced spinorbit coupling in tetragonally strained FeCoB films'. *Journal of Physics: Condensed Matter*, **29**:275802, 2017.

[105] C. T. Chen, Y. U. Idzerda, H.-J. Lin, N. V. Smith, G. Meigs, E. Chaban, G. H. Ho, E. Pellegrin, and F. Sette. 'Experimental confirmation of the x-ray magnetic circular dichroism sum rules for iron and cobalt'. *Physical Review Letters*, **75**:152–155, 1995.

[106] I. P. Miranda, R. N. Igarashi, A. B. Klautau, and H. M. Petrilli. 'Dimensionality effects on magnetic properties of Fe_xCo_{1-x} nanoclusters on Pt(111)'. *Journal of Magnetism and Magnetic Materials*, **441**:222–229, 2017.

[107] S. Ouazi, S. Vlaic, S. Rusponi, G. Moulas, P. Buluschek, K. Halleux, S. Bornemann, S. Mankovsky, J. Minár, J.B. Staunton, H. Ebert, and H. Brune. 'Atomic-scale engineering of magnetic anisotropy of nanostructures through interfaces and interlines'. *Nature Communications*, **3**:1313, 2012.

[108] A. Lehnert, S. Dennler, P. Błński, S. Rusponi, M. Etzkorn, G. Moulas, P. Bencok, P. Gambardella, H. Brune, and J. Hafner. 'Magnetic anisotropy of Fe and Co ultrathin films deposited on Rh(111) and Pt(111) substrates: An experimental and first-principles investigation'. *Physical Review B*, **82**:094409, 2010.

[109] P. Gambardella, A. Dallmeyer, K. Maiti, M. C. Malagoli, W. Eberhardt, K. Kern, and C. Carbone. 'Ferromagnetism in one-dimensional monatomic metal chains'. *Nature*, **416**:301–304, 2002.

[110] S. K. Hämäläinen, M. Stepanova, R. Drost, P. Liljeroth, J. Lahtinen, and J. Sainio. 'Self-assembly of cobalt-phthalocyanine molecules on epitaxial graphene on Ir(111)'. *The Journal of Physical Chemistry C*, **116**:20433–20437, 2012.

[111] A. D. Oyedele, C. M. Rouleau, D. B. Geohegan, and K. Xiao. 'The growth and assembly of organic molecules and inorganic 2D materials on graphene for van der Waals heterostructures'. *Carbon*, **131**:246–257, 2018.

[112] D. Chylarecka, C. Wäckerlin, T. K. Kim, K. Müller, F. Nolting, A. Kleibert, N. Ballav, and T. A. Jung. 'Self-assembly and superexchange coupling of magnetic molecules on oxygen-reconstructed ferromagnetic thin film'. *Journal of Physical Chemistry Letters*, **1**:1408–1413, 2010.

[113] M. Bazarnik, J. Brede, R. Decker, and R. Wiesendanger. 'Tailoring molecular self-assembly of magnetic phthalocyanine molecules on Fe- and Co-intercalated graphene'. *ACS Nano*, **7**:11341–11349, 2013.

[114] F. Evangelista, V. Carravetta, G. Stefani, B. Jansik, M. Alagia, S. Stranges, and A. Ruocco. 'Electronic structure of copper phthalocyanine: An experimental and theoretical study of occupied and unoccupied levels'. *The Journal of Chemical Physics*, **126**:124709, 2007.

[115] J. Uihlein, H. Peisert, H. Adler, M. Glaser, M. Polek, R. Ovsyannikov, M. Bauer, and T. Chassé. 'Strong interaction of MnPc on Ni(111): influence of graphene buffer layer'. *The Journal of Physical Chemistry C*, **118**:28671–28678, 2014.

[116] L. Massimi, M. Angelucci, P. Gargiani, M. G. Betti, S. Montoro, and C. Mariani. 'Metal-phthalocyanine ordered layers on Au(110): metal-dependent adsorption energy'. *The Journal of Chemical Physics*, **140**:244704, 2014.

[117] N. Marom, O. Hod, G. E. Scuseria, and L. Kronik. 'Electronic structure of copper phthalocyanine: a comparative density functional theory study'. *The Journal of Chemical Physics*, **128**:164107, 2008.

[118] M. Grobosch, C. Schmidt, R. Kraus, and M. Knupfer. 'Electronic properties of transition metal phthalocyanines: the impact of the central metal atom (d^5d^{10})'. *Organic Electronics*, **11**:1483–1488, 2010.

[119] S. Hüfner. *Photoelectron spectroscopy: principles and applications*. Springer Berlin Heidelberg, 1995.

[120] T. Breuer, M. Klues, and G. Witte. 'Characterization of orientational order in π-conjugated molecular thin films by NEXAFS'. *Organic Electronics*, **204**:102–115, 2015.

[121] R. De Francesco, M. Stener, and G. Fronzoni. 'Theoretical study of Near-Edge X-ray Absorption Fine Structure spectra of metal phthalocyanines at C and N K-edges'. *The Journal of Physical Chemistry A*, **116**:2885–2894, 2012.

[122] T. M. Willey, M. Bagge-Hansen, J. R. I. Lee, R. Call, L. Landt, T. van Buuren, C. Colesniuc, C. Monton, I. Valmianski, and Ivan K. Schuller. 'Electronic structure differences between H_2-, Fe-, Co-, and Cu-phthalocyanine highly oriented thin films observed using NEXAFS spectroscopy'. *The Journal of Chemical Physics*, **139**:034701, 2013.

[123] S. Javaid, M. Bowen, S. Boukari, L. Joly, J.-B. Beaufrand, Xi Chen, Y. J. Dappe, F. Scheurer, J.-P. Kappler, J. Arabski, W. Wulfhekel, M. Alouani, and E. Beaurepaire. 'Impact on interface spin polarization of molecular bonding to metallic surfaces'. *Physical Review Letters*, **105**:077201, 2010.

[124] M. L. M. Rocco, K.H. Frank, P. Yannoulis, and E.E. Koch. 'Unoccupied electronic structure of phthalocyanine films'. *The Journal of Chemical Physics*, **93**:6859–6864, 1990.

[125] L. Floreano, A. Cossaro, R. Gotter, A. Verdini, G. Bavdek, F. Evangelista, A. Ruocco, A. Morgante, and D. Cvetko. 'Periodic arrays of Cu-phthalocyanine chains on Au(110)'. *The Journal of Physical Chemistry C*, **112**:10794–10802, 2008.

[126] F. Petraki, H. Peisert, F. Latteyer, U. Aygl, A. Vollmer, and T. Chassé. 'Impact of the 3d electronic states of cobalt and manganese phthalocyanines on the electronic structure at the interface to Ag(111)'. *The Journal of Physical Chemistry C*, **115**:21334–21340, 2011.

[127] D. Klar, B. Brena, H. C. Herper, S. Bhandary, C. Weis, B. Krumme, C. Schmitz-Antoniak, B. Sanyal, O. Eriksson, and H. Wende. 'Oxygen-tuned magnetic cou-

pling of Fe-phthalocyanine molecules to ferromagnetic Co films'. *Physical Review B*, **88**:224424, 2013.

[128] S.-H. Chang, S. Kuck, J. Brede, L. Lichtenstein, G. Hoffmann, and R. Wiesendanger. 'Symmetry reduction of metal phthalocyanines on metals'. *Physical Review B*, **78**:233409, 2008.

[129] X. Sun, B. Wang, and Y. Yamauchi. 'Electronic structure and spin polarization of metal (Mn, Fe, Cu) phthalocyanines on an Fe(100) surface by first-principles calculations'. *Journal of Physical Chemistry C*, **116**:18752–18758, 2012.

[130] Md. E. Ali, B. Sanyal, and P. M. Oppeneer. 'Tuning the magnetic interaction between manganese porphyrins and ferromagnetic Co substrate through dedicated control of the adsorption'. *The Journal of Physical Chemistry C*, **113**:14381–14383, 2009.

[131] L. Massimi, S. Lisi, D. Pacilé, C. Mariani, and M. G. Betti. 'Interaction of iron phthalocyanine with the graphene/Ni(111) system'. *Beilstein Journal of Nanotechnology*, **5**:308–312, 2014.

[132] F. Evangelista, A. Ruocco, R. Gotter, A. Cossaro, L. Floreano, A. Morgante, F. Crispoldi, M. G. Betti, and C. Mariani. 'Electronic states of CuPc chains on the Au(110) surface'. *The Journal of Chemical Physics*, **131**:174710, 2009.

[133] A. Ruocco, F. Evangelista, A. Attili, M. P. Donzello, M. G. Betti, L. Giovanelli, and R. Gotter. 'Copper-phthalocyanine ultra thin films grown onto Al(1 0 0) surface investigated by synchrotron radiation'. *Journal of Electron Spectroscopy and Related Phenomena*, **137-140**:165–169, 2004.

[134] S. Lach, A. Altenhof, K. Tarafder, F. Schmitt, Md. E. Ali, M. Vogel, J. Sauther, P. M. Oppeneer, and C. Ziegler. 'Metalorganic hybrid interface states of a ferromagnet/organic semiconductor hybrid junction as basis for engineering spin injection in organic spintronics'. *Advanced Functional Materials*, **22**:989–997, 2012.

[135] Q.-H. Wu, G. H., T. W. Ng, and S. T. Lee. 'Substrate effect on the electronic structures of CuPc/graphene interfaces'. *Applied Physics Letters*, **100**:161603, 2012.

[136] W. Dou, S. Huang, R. Q. Zhang, and C. S. Lee. 'Moleculesubstrate interaction channels of metal-phthalocyanines on graphene on Ni(111) surface'. *The Journal of Chemical Physics*, **134**:094705, 2011.

[137] T. Kroll, R. Kraus, R. Schönfelder, V. Yu. Aristov, O. V. Molodtsova, P. Hoffmann, and M. Knupfer. 'Transition metal phthalocyanines: Insight into the electronic structure from soft X-ray spectroscopy'. *The Journal of Chemical Physics*, **137**:054306, 2012.

[138] M. V. Nardi, F. Detto, L. Aversa, R. Verucchi, G. Salviati, S. Iannotta, and M. Casarin. 'Electronic properties of CuPc and H_2Pc: an experimental and theoretical study'. *Physical Chemistry Chemical Physics*, **15**:12864–12881, 2013.

[139] J. Uihlein, H. Peisert, H. Adler, M. Glaser, M. Polek, R. Ovsyannikov, and T. Chassé. 'Interface between FePc and Ni(111): influence of graphene buffer layers'. *The Journal of Physical Chemistry C*, **118**:10106–10112, 2014.

[140] J. Bartolomé, F. Bartolomé, L. M. García, G. Filoti, T. Gredig, C. N. Colesniuc, I. K. Schuller, and J. C. Cezar. 'Highly unquenched orbital moment in textured Fe-phthalocyanine thin films'. *Physical Review B*, **81**:195405, 2010.

[141] C. Isvoranu, B. Wang, E. Ataman, J. Knudsen, K. Schulte, J. N. Andersen, M.-L. Bocquet, and J. Schnadt. 'Comparison of the carbonyl and nitrosyl complexes formed by adsorption of CO and NO on monolayers of iron phthalocyanine on Au(111)'. *The Journal of Physical Chemistry C*, **115**:24718–24727, 2011.

[142] M. Schmid, J. Zirzlmeier, H.-P. Steinrück, and J. M. Gottfried. 'Interfacial interactions of iron(II) tetrapyrrole complexes on Au(111)'. *The Journal of Physical Chemistry C*, **115**:17028–17035, 2011.

[143] N. Marom and L. Kronik. 'Density functional theory of transition metal phthalocyanines, II: electronic structure of MnPc and FePc–symmetry and symmetry breaking'. *Applied Physics A*, **95**:165–172, 2009.

[144] I. E. Brumboiu, S. Haldar, J. Lüder, O. Eriksson, H. C. Herper, B. Brena, and B. Sanyal. 'Influence of electron correlation on the electronic structure and magnetism of transition-metal phthalocyanines'. *Journal of Chemical Theory and Computation*, **12**:1772–1785, 2016.

[145] J.-Q. Zhong, Z. Wang, J. L. Zhang, C. A. Wright, K. Yuan, C. Gu, A. Tadich, D. Qi, H. X. Li, M. Lai, K. Wu, G. Q. Xu, W. Hu, Z. Li, and W. Chen. 'Reversible tuning of interfacial and intramolecular charge transfer in individual MnPc molecules'. *Nano Letters*, **15**:8091–8098, 2015.

[146] T. Schwieger, H. Peisert, M. S. Golden, M. Knupfer, and J. Fink. 'Electronic structure of the organic semiconductor copper phthalocyanine and K-CuPc studied using photoemission spectroscopy'. *Physical Review B*, **66**:155207, 2002.

[147] C. Wäckerlin, J. Nowakowski, S.-X. Liu, M. Jaggi, D. Siewert, J. Girovsky, A. Shchyrba, T. Hählen, A. Kleibert, P. M. Oppeneer, F. Nolting, S. Decurtins, T. A. Jung, and N. Ballav. 'Twodimensional supramolecular electron spin arrays'. *Advanced Materials*, **25**:2404–2408, 2013.

[148] C. Isvoranu, B. Wang, K. Schulte, E. Ataman, J. Knudsen, J. N. Andersen, M. L. Bocquet, and J. Schnadt. 'Tuning the spin state of iron phthalocyanine by ligand adsorption'. *Journal of Physics: Condensed Matter*, **22**:472002, 2010.

[149] N. Tsukahara, K.-I. Noto, M. Ohara, S. Shiraki, N. Takagi, Y. Takata, J. Miyawaki, M. Taguchi, A. Chainani, S. Shin, and M. Kawai. 'Adsorption-induced switching of magnetic anisotropy in a single iron(II) phthalocyanine molecule on an oxidized Cu(110) surface'. *Physical Review Letters*, **102**:167203, 2009.

[150] S. Bhandary, B. Brena, P. M. Panchmatia, I. Brumboiu, M. Bernien, C. Weis, B. Krumme, C. Etz, W. Kuch, H. Wende, O. Eriksson, and B. Sanyal. 'Manipulation of spin state of iron porphyrin by chemisorption on magnetic substrates'. *Physical Review B*, **88**:024401, 2013.

[151] S. Stepanow, P. S. Miedema, A. Mugarza, G. Ceballos, P. Moras, J. C. Cezar, C. Carbone, F. M. F. de Groot, and P. Gambardella. 'Mixed-valence behavior and strong correlation effects of metal phthalocyanines adsorbed on metals'. *Physical Review B*, **83**:220401, 2011.

[152] H. Wende, M. Bernien, J. Luo, C. Sorg, N. Ponpandian, J. Kurde, J. Miguel, M. Piantek, X. Xu, Ph. Eckhold, W. Kuch, K. Baberschke, P. M. Panchmatia, B. Sanyal, P. M. Oppeneer, and O. Eriksson. 'Substrate-induced magnetic ordering and switching of iron porphyrin molecules'. *Nature Materials*, **6**:516–520, 2007.

[153] M. Bernien, J. Miguel, C. Weis, Md. E. Ali, J. Kurde, B. Krumme, P. M. Panchmatia, B. Sanyal, M. Piantek, P. Srivastava, K. Baberschke, P. M. Oppeneer, O. Eriksson, W. Kuch, and H. Wende. 'Tailoring the nature of magnetic coupling of Fe-porphyrin molecules to ferromagnetic substrates'. *Physical Review Letters*, **102**:047202, 2009.

[154] P. Gargiani, R. Cuadrado, H. B. Vasili, M. Pruneda, and M. Valvidares. 'Graphene-based synthetic antiferromagnets and ferrimagnets'. *Nature Communications*, **8**:699, 2017.

[155] W. Kuch and M. Bernien. 'Controlling the magnetism of adsorbed metalorganic molecules'. *Journal of Physics: Condensed Matter*, **29**:023001, 2016.

[156] C. Piamonteze, P. Miedema, and F. M. F. de Groot. 'Accuracy of the spin sum rule in XMCD for the transition-metal L edges from manganese to copper'. *Physical Review B*, **80**:184410, 2009.

[157] T. O. Wehling, A. I. Lichtenstein, and M. I. Katsnelson. 'Transition-metal adatoms on graphene: Influence of local Coulomb interactions on chemical bonding and magnetic moments'. *Physical Review B*, **84**:235110, 2011.

[158] A. Mugarza, R. Robles, C. Krull, R. Korytár, N. Lorente, and P. Gambardella. 'Electronic and magnetic properties of molecule-metal interfaces: transition-metal phthalocyanines adsorbed on Ag(100)'. *Physical Review B*, **85**:155437, 2012.

[159] I. Grimaldi, M. Papagno, L. Ferrari, P. M. Sheverdyaeva, S. K. Mahatha, D. Pacilè, and C. Carbone. 'Magnetic decoupling of ferromagnetic metals through a graphene spacer'. *Journal of Magnetism and Magnetic Materials*, **426**:440–443, 2017.

[160] E. Cobas, A. L. Friedman, O. M. J. van't Erve, J. T. Robinson, and B. T. Jonker. 'Graphene as a tunnel barrier: graphene-based magnetic tunnel junctions'. *Nano Letters*, **12**:3000–3004, 2012.

[161] O. V. Yazyev and A. Pasquarello. 'Magnetoresistive junctions based on epitaxial graphene and hexagonal boron nitride'. *Physical Review B*, **80**:035408, 2009.

[162] S. Stepanow, A. Mugarza, G. Ceballos, P. Moras, J. C. Cezar, C. Carbone, and P. Gambardella. 'Giant spin and orbital moment anisotropies of a Cu-phthalocyanine monolayer'. *Physical Review B*, **82**:014405, 2010.

[163] A. Rosa and E. J. Baerends. 'Metal-macrocycle interaction in phthalocyanines: density functional calculations of ground and excited states'. *Inorganic Chemistry*, **33**:584–595, 1994.

[164] J. Wang, Y. Shi, J. Cao, and R. Wu. 'Magnetization and magnetic anisotropy of metallophthalocyanine molecules from the first principles calculations'. *Applied Physics Letters*, **94**:122502, 2009.

[165] T. Kataoka, Y. Sakamoto, Y. Yamazaki, V. R. Singh, A. Fujimori, Y. Takeda, T. Ohkochi, S.-I. Fujimori, T. Okane, Y. Saitoh, H. Yamagami, and A. Tanaka. 'Electronic configuration of Mn ions in the π-d molecular ferromagnet β-Mn phthalocyanine studied by soft X-ray magnetic circular dichroism'. *Solid State Communications*, **152**:806–809, 2012.

[166] G. Avvisati, P. Gargiani, P. Mondelli, F. Presel, A. Baraldi, and M. G. Betti. 'Superexchange pathways stabilize the magnetic coupling of MnPc with Co in a spin interface mediated by graphene'. *Physical Review B*, **98**:115412, 2018.

[167] D. Fiorani, G. Asti, and F. Lucari. *Magnetic Properties Of Matter – Proceedings Of The Second National School*. World Scientific, 1991.

[168] M. Bernien, X. Xu, J. Miguel, M. Piantek, Ph. Eckhold, J. Luo, J. Kurde, W. Kuch, K. Baberschke, H. Wende, and P. Srivastava. 'Fe-porphyrin monolayers on ferromagnetic substrates: Electronic structure and magnetic coupling strength'. *Physical Review B*, **76**:214406, 2007.

[169] I. E. Brumboiu, R. Totani, M. de Simone, M. Coreno, C. Grazioli, L. Lozzi, H. C. Herper, B. Sanyal, O. Eriksson, C. Puglia, and B. Brena. 'Elucidating the 3d electronic configuration in manganese phthalocyanine'. *The Journal of Physical Chemistry A*, **118**:927–932, 2014.

[170] U. Mazur and K. W. Hipps. 'Orbital-mediated tunneling, inelastic electron tunneling, and electrochemical potentials for metal phthalocyanine thin films'. *The Journal of Physical Chemistry B*, **103**:9721–9727, 1999.

[171] Y. Taguchi, T. Miyake, S. Margadonna, K. Kato, K. Prassides, and Y. Iwasa. 'Synthesis, structure, and magnetic properties of Li-doped manganese-phthalocyanine,

Li_x[MnPc] ($0 \leq x \geq 4$)'. *Journal of the American Chemical Society*, **128**:3313–3323, 2006.

[172] B. Mahns, F. Roth, M. Grobosch, D. R. T. Zahn, and M. Knupfer. 'Electronic excitations of potassium intercalated manganese phthalocyanine investigated by electron energy-loss spectroscopy'. *The Journal of Chemical Physics*, **134**:194504, 2011.

[173] S. Stepanow, A. Lodi Rizzini, C. Krull, J. Kavich, J. C. Cezar, F. Yakhou-Harris, P. M. Sheverdyaeva, P. Moras, C. Carbone, G. Ceballos, A. Mugarza, and P. Gambardella. 'Spin tuning of electron-doped metalphthalocyanine layers'. *Journal of the American Chemical Society*, **136**:5451–5459, 2014.

[174] F. Reinert and S. Hüfner. 'Photoemission spectroscopy–from early days to recent applications'. *New Journal of Physics*, **7**:97, 2005.

[175] J. Stöhr. *NEXAFS spectroscopy*. Springer Berlin Heidelberg, 1992.

[176] B. H. Bransden and C. J. Joachain. *Physics of atoms and molecules*. Pearson, 2003.

[177] G. van der Laan and A. I. Figueroa. 'X-ray magnetic circular dichroism–A versatile tool to study magnetism'. *Coordination Chemistry Reviews*, **277–278**:95–129, 2014.

[178] J. Stöhr and H. C. Siegmann. *Magnetism: from fundamentals to nanoscale dynamics*. Springer Berlin Heidelberg, 2006.

[179] F. de Groot and A. Kotani. *Core level spectroscopy of solids*. CRC Press, 2008.

[180] D. Phil Woodruff. *Modern techniques of surface science*. Cambridge University Press, 2016.

[181] A. Barla, J. Nicolás, D. Cocco, S. M. Valvidares, J. Herrero-Martín, P. Gargiani, J. Moldes, C. Ruget, E. Pellegrin, and S. Ferrer. 'Design and performance of BOREAS, the beamline for resonant X-ray absorption and scattering experiments at the ALBA synchrotron light source'. *Journal of Synchrotron Radiation*, **23**:1507–1517, 2016.